



Università degli Studi di Pavia

Università della Svizzera italiana

Joint PhD program in Computational Mathematics and Decision Sciences

XXXV Cycle

Artificial Intelligence, Mathematical Modeling and Magnetic Resonance Imaging for Precision Medicine in Neurology and Neuroradiology

PhD Dissertation of:

Giulia Colelli

PhD Coordinator:

Prof. Luca Pavarino

Supervisor:

Prof. Silvia Figini

Prof. Anna Pichiecchio

Academic year 2021-2022

"Tieni duro, non mollare, non ti fare passare la voglia"

A Nonno Ciccio

Acknowledgements

First of all, I would like to thank my supervisors Prof. Silvia Figini and Prof. Anna Pichiecchio that gave me the opportunity to do this experience and who offer me all the support I needed.

I would like also to thank the IRCCS Mondino Foundation, its scientific directors Fabio Blandini and then Roberto Bergamaschi for allowing me to have the opportunity for fruitful collaborations with Neuroradiology Department.

I would like also to thank Prof. Mattia Zanella and Prof. Antonietta Mira for giving me the possibility to collaborate in interesting research activities.

I would like also to thank Prof. Alessandro Lascialfari who has been a scientific point of reference for me during the PhD years and who has been fundamental to my academic growth.

A big thank you goes to Prof. Alessandro Bacchetta and Dr. Francesco Giovanni Celiberto for their support, for believing in me and helping me to develop my improbable and weird ideas, turning them in a scientific research activity.

Another big thank goes to all the Neuroradiology department of Mondino, for the friendly and supportive environment, in particular to Prof. Anna Pichiecchio, Dott. Matteo Paoletti, Dott. Carlo Asteggiano for also supporting me in the clinical aspects of neuromuscular diseases but above all because they supported me even humanly and psychologically.

A big thank you goes to my colleagues and friends Laura, Leonardo, Giulia, Francesca L. for supporting and putting up with me not only on a working level but also on a human level. Without them I am not sure that I would reach this milestone.

I am very grateful to my parents for supporting me, loving me, giving me the serenity that I need and for standing by my side no matter what.

I thank my sister Sefora and my brother Vincenzo for always be there for me, supporting me and giving me all the love that I need.

I would like to thank all my relatives for always supporting me, my grandmothers and my cousins Frank and Angela.

I would like to thank my lifelong friend Michelle for giving me the opportunity to share experience, to grow up together and for being there for me.

A big thank to my Friend Francesca T. for supporting me and for cheering me up.

I would like to thank my friend from ResBio and in particular my "cucina" for sharing together happy moments, failures, good advices and for being my second family here in Pavia. In particular, I would like to thank Francesca M., Erica, Dante and Giovanni for, among everything, the interesting dinner conversions on neuronal physiology. I would also like to thank " gli Spec." Giovanni, Laura, Alessandro and Paolo for sharing good experiences together and for their medical advices.

I would like to thank my friend Antonio for supporting me and giving me good advises in the important choices of my life.

Last but not least, I would like to thank my grandfather Ciccio, even if he is no longer physically with me he still supports me with all the things that he thought me and I know he would be proud of me for reaching this achievement.

I would also like to thank all the people that I have known during these years in Pavia, some have contributed in a positive way others in a negative way but they all gave me the opportunity to grow.

Abstract

The thesis addresses the possibility of using mathematical methods, simulation techniques, repurposed physical theories and artificial intelligence algorithms to fulfill clinical needs in neuroradiology and neurology. The aim is to describe and to predict disease patterns and its evolution over time as well as to support clinical decision-making processes. The thesis is divided into three parts.

Part 1 is related to the development of a Radiomic workflow combined with Machine Learning algorithms in order to predict parameters that quantify muscular anatomical involvement in neuromuscular diseases, with special focus on Facioscapulohumeral dystrophy. The proposed workflow relies on conventional Magnetic Resonance Imaging sequences available in most neuromuscular centers and it can be used as a non-invasive tool to monitor even fine change in neuromuscular disorders and to evaluate longitudinal diseases' progression over time.

Part 2 is about the description of a kinetic model for tumor growth by means of classical tools of statistical mechanics for many-agent systems also taking into account the effects of clinical uncertainties related to patients' variability in tumor progression. The action of therapeutic protocols is modeled as feedback control at the microscopic level. The controlled scenario allows the dumping of uncertainties associated with the variability in tumors' dynamics. Suitable numerical methods, based on Stochastic Galerkin formulation of the derived kinetic model, are introduced.

Part 3 refers to a still-on going project that attempts to describe a brain portion through a quantum field theory and to simulate its behavior through the implementation of a neural network with an ad-hoc activation function mimicking the biological neuron model response function. Under considered

conditions, the brain portion activity can be expressed up to $O(6)$, *i.e.*, up to six fields interaction, as a Gaussian Process. The defined quantum field framework may also be extended to the case of a Non-Gaussian Process behavior, or rather to an interacting quantum field theory in a Wilsonian Effective Field theory approach.

List of papers published or in preparation that are reported in the thesis

Paper I

Felisaz, P.F., Colelli, G., Ballante, E., Solazzo, F., Paoletti, M., Germani, G., Santini, F., Deligianni, X., Bergsland, N., Monforte, M., et al. “Texture analysis and machine learning to predict water T2 and fat fraction from non-quantitative MRI of thigh muscles in Facioscapulohumeral muscular dystrophy”. In: *European Journal of Radiology* (2021) DOI: [10.1016/j.ejrad.2020.109460](https://doi.org/10.1016/j.ejrad.2020.109460)

Paper II

Colelli, G., Barzaghi, L., Paoletti, M., Santini, F., Deligianni, X., Figini, S., Mira, A., Pichiecchio, A. “Texture analysis and machine learning applied to STIR sequence for prediction of quantitative parameters in facioscapulohumeral disease”. *Submitted to Frontiers in Neurology, November 2022.*

Paper III

Agosti, A., Shaqiri, E., Paoletti, M., Solazzo, F., Bergsland, N., Colelli, G., Savini, G., Muzic, S. I., Santini, F., Deligianni, X., et al. “Deep learning for automatic segmentation of thigh and leg muscles”. In: *Magnetic Resonance Materials in Physics, Biology and Medicine* (2022) DOI: [10.1007/s10334-021-00967-4](https://doi.org/10.1007/s10334-021-00967-4)

Paper IV

Medaglia, A., Colelli, G., Farina, L., Bacila, A., Bini, P., Marchioni, E., Figini, S., Pichiecchio, A., Zanella, M. “Uncertainty quantification and control of kinetic models of tumour growth under clinical uncertainties”. In: *International Journal of Non-Linear Mechanics* (2022) DOI: [10.1016/j.ijnonlinmec.2022.103933](https://doi.org/10.1016/j.ijnonlinmec.2022.103933).

Paper V

Colelli, G., Celiberto, F.G., Pichiecchio, A., Figini, S., Bacchetta, A. “Quantum Field Theory and Neural Network for the description of a brain portion: a first attempt”. *Manuscript in preparation*.

Contents

Abstract	v
List of papers published or in preparation that are reported in the thesis	vii
Contents	ix
List of Figures	xiii
List of Tables	xxi
Introduction	1
References	6
I Magnetic Resonance Imaging, Artificial Intelligence and Radiomics for the Quantification of neuromuscular biomarkers: a special focus on Facioscapulo-humeral dystrophy	9
Introduction	11
References	18
I Texture analysis and machine learning to predict water T2 and fat fraction from non-quantitative MRI of thigh muscles in Facioscapulohumeral muscular dystrophy	21
I.1 Introduction	23
I.2 Methods	24

I.3	Machine Learning and statistical assessment	27
I.4	Results	28
I.5	Discussion	30
I.6	Appendix A. Supplementary data	33
	References	36
II Texture analysis and machine learning applied to STIR		
sequence for prediction of quantitative parameters in		
facioscapulohumeral disease		
II.1	Introduction	43
II.2	Materials and Methods	45
II.3	Results	51
II.4	Discussion	54
	References	56
III Deep learning for automatic segmentation of thigh and leg		
muscles		
III.1	Introduction	68
III.2	Materials and methods	71
III.3	Results	86
III.4	Discussion	93
III.5	Conclusion	96
	References	97
2 Kinetic Theory and Uncertainties Quantification for		
Tumor Growth		
		101
Introduction		
		103
	References	106
IV Uncertainty quantification and control of kinetic models		
of tumour growth under clinical uncertainties		
		109

IV.1	Introduction	111
IV.2	Kinetic modelling of tumour growth dynamics with clinical uncertainties	114
IV.3	Observable effect of therapeutic protocols	120
IV.4	Quantities of interest and data	128
IV.5	Numerical tests	134
	References	146
3	A first attempt to combine quantum field theory, neural network and brain description	153
	Introduction	155
	References	158
V	Quantum Field Theory and Neural Network for the description of a brain portion: a first attempt	161
V.1	Introduction	163
V.2	Theory	167
V.3	Correspondence between quantum-field theory and neural network	169
V.4	Reproducing the behavior of a brain portion using a neural network	173
V.5	From the signal space to physical space	188
V.6	Conclusion and future perspectives	190
	References	194
	Conclusion	199

List of Figures

0.1	$B_{ext}^{\vec{}} = 0$ (left) the spins are oriented in random way and \vec{M} is zero. $B_{ext}^{\vec{}} \neq 0$ (right) few spins are aligned along the external field direction: the \vec{M} in this case is different from zero and it is oriented along the axis of the external magnetic field.	12
0.2	Free Induction Decay (FID). The detected signal is reported on the y-axis and the time t on the x-axis. The signal oscillates with the Larmor frequency and it decays exponentially with a time constant $T2^*$	13
0.3	$T1$ -weighted image related to Facioscapulohumeral muscular dystrophy patient and acquired with a $T1$ -turbo Spin Echo at Neuroradiology Department of IRCCS Fondazione Mondino. . .	15
0.4	$T2$ -weighted image related to a Facioscapulohumeral muscular dystrophy patient and acquired with STIR sequence at Neuroradiology Department of IRCCS Fondazione Mondino.	16
I.1	Illustration of the ROI drawing process. A typical axial $T2$ weighted image (TE=88 ms) extracted from the MESE sequence is shown (a). One operator manually drew ROIs of each muscle of the thigh (b). 12 muscle ROIs per side per each of the 5 central slices acquired were drawn, for a total of 120 ROIs. For the analysis, ROIs of the same muscle from both sides and from of all slices were merged for a total of 12 observations (each shown with a different color) per examination (b,c).	27

I.2	Comparison of Fat Fraction MAE (top) and water T2 MAE (bottom) obtained with LOO cross validation and k-folds cross validation. On the x-axis are reported the implemented ML algorithms listed in Table I.3 and I.4.	35
I.3	Comparison of Fat Fraction MSE (top) and water T2 MSE (bottom) obtained with LOO cross validation and k-folds cross validation. On the x-axis are reported the implemented ML algorithms listed in Table I.3 and I.4.	36
II.1	Optimized information imbalance respect to the target biomarker FF(top) and to the wT2 (bottom) showed as a function of subsets of radiomic features space A.	49
II.2	Muscle-wise MAE boxplots (first quartile (Q1) to third quartile (Q3) and median value in orange line) for FF (top) expressed in percentage points (pp) and wT2 (bottom) expressed in ms. Three boxplots are given for each muscle related to WF 1 (blue), WF 2 (green), WF 3 (red). Highest accuracy is related to red dots (FF, wT2 boxplots) corresponding to KNN prediction performances. .	60
II.3	FF (top) and wT2 (bottom) prediction performances averaged on all muscles and showed as a function of the different implemented ML algorithms. According to the proposed workflows, a trio of mean prediction accuracy was define for each ML model, <i>i.e.</i> , green plot (WF1), blue plot (WF2), red plot (WF3).	61
II.4	Muscle-wise boxplots (first quartile (Q1) to third quartile (Q3) and median value in orange line) for FF (top) and wT2 (bottom) gold standard values, with CV listed in the legend.	62
II.5	Muscle-wise volume boxplots (first quartile (Q1) to third quartile (Q3) and median value in orange line). Muscle-wise mean volume size is reported in round brackets on x-axis, CV is listed in legend. .	63

III.1	Illustrative example of thigh and leg slices from MRI scans with the superposition of the corresponding muscles' manual segmentation and indications of the muscles' names. A Thigh case; B Leg case	75
III.2	Building blocks of the networks' architectures, with descriptions of the performed operations	77
III.3	Graphical representation of the network's architecture for the classification task. The number of channels, spatial dimensions and number of neurons are indicated next to each building block, together with the indications of the input and the output of the data flow	79
III.4	Graphical representation of the network's architecture for the segmentation tasks. The number of channels, spatial dimensions and number of neurons are indicated next to each building block, together with the indications of the input and the different outputs of the data flow	81
III.5	Graphical representation of the network's architecture as a tree-like structure	82
III.6	Illustrative example of thigh and leg plots of the weight maps (III.2). A Weights map associated to the background regions separating neighboring muscles for the thigh case; B Full weight map for the thigh case; C Weights map associated to the background regions separating neighboring muscles for the leg case; D Full weight map for the leg case	85
III.7	Plots of the model losses and model accuracies during the training of the classification network (A and B), the thigh segmentation network (C and D) and the leg segmentation network (E and F)	88

III.8	Illustrative comparisons between the manual segmentation and the network (DNN) generated segmentation for three elements in the training and three elements in the validation datasets, for both the thigh and leg case, with the corresponding <i>Dice coefficient score</i>	89
III.9	Comparisons between the manual segmentation and the network (DNN) generated segmentation of thigh muscles for 5 patients with mild and 5 patients with severe fat infiltrations in the test dataset. The bottom (leftmost column), inner and top (rightmost column) slices are reported	91
III.10	Comparisons between the manual segmentation and the network (DNN) generated segmentation of leg muscles for 5 patients with mild and 5 patients with severe fat infiltrations in the test dataset. The inner slice is reported	92
III.11	Comparisons between the manual segmentation and the network (DNN) generated segmentation of the thigh and leg muscles for subject A and subject B, shown along with two coronal and sagittal slices	92
IV.1	Growth curves and empirical data relative to untreated glioblastoma. The trajectory of each curve (solid line) and the empirical volume size (circle marker) data are shown for each patient and for different growth laws: Gompertz case (left plot), von Bertalanffy case (right plot). Values reported on y-axes are scaled by a quantity of 10^5	133
IV.2	Empirical distributions of the obtained parameters and fitted Beta distributions with parameters given in Table IV.1	134

IV.3	Convergence of the L^2 error with respect to a reference solutions obtained with $\bar{M} = 50$, at fixed time $T = 10$. The top row corresponds to the Gompertz case whereas the bottom row to the von Bertalanffy case. Top-Left: $z_1 = \alpha \sim \mathcal{U}([10^{-3}, 3 \cdot 10^{-2}])$ and fixed $z_2 = x_L \equiv 0.5$. Top-Right: $z_2 = x_L \sim B(c_1, c_2)$ and fixed $z_1 = \alpha \equiv 0.01$. Bottom-Left: $z_1 = a \sim B(c_1, c_2)$ and fixed $z_2 = q \equiv 0.01$, $z_3 = x_L \equiv 0.5$. Bottom-Right: $z_2 = q \sim B(c_1, c_2)$ and fixed $z_1 = a \equiv 0.8$, $z_3 = x_L \equiv 0.5$. The values (c_1, c_2) are reported in Table IV.1.	140
IV.4	Top: large time distribution (left) and evolution of the mean volume (right) for the Gompertz kinetic model with 2D uncertainties. The solid line is the numerical solution of (IV.11) at the final time $T = 500$, the markers refers to the expectation of the analytic solution (IV.13). Bottom: large time distribution (left) and evolution of the mean volume (right) for the von Bertalanffy kinetic model with 3D uncertainties. In all the cases, we choose $\Delta x = 10^{-2}$, $\Delta t = \Delta x/C$ with $C = 10^2$ and $M = 3$. (For interpretation of the references to colour in this figure legend, the reader is referred to the web version of this article).	141
IV.5	Evolution of $m(\mathbf{z}, t)$ in the uncontrolled scenario for $t \leq 60$ and in a controlled scenario for $t > 60$, with $p = 1, 2$, $S(x) = 1, \sqrt{x}$ and $\kappa = 0.1, 1$. The dashed lines represent the trend of the tumour if the control is not in action. In the case $p = 2$, we adopted a sG scheme with $\Delta x = 10^{-2}$, $\Delta t = \Delta x/C$ with $C = 10^2$, $M = 3$ for the numerical solution of (IV.32) with the introduced clinical uncertainties. In the case $p = 1$, we adopted a stochastic collocation DSMC with $N = 10^5$, $\Delta t = 0.05$, $\epsilon = 2\Delta t$ and $M = 3$. We considered the experimental target volume size $x_d = 0.18 \times 10^5 \text{mm}^3$. and the results are scaled by a factor 10^5 . .	142
IV.6	144
IV.7	145

V.1	Example of cortical layered microcircuit consisting of four layers of excitatory neurons' population (E) and four layers of inhibitory neurons' population (I). Image from Layer et al. 2022	177
V.2	n-pt deviation calculated as (V.10) normalized for $G_{GP}^{(n)}$ and generated by the activation function 1. Signal represents element of the tensor $m_n = \frac{\Delta G_n^n}{G_{GP}^n}$ and the background the average element-wise standard deviation. The experiment is done with 10^3 networks for a run and inputs defined in (V.21)	179
V.3	n-pt deviation calculated as (V.10) normalized for $G_{GP}^{(n)}$ and generated by the activation function 2. Signal represents element of the tensor $m_n = \frac{\Delta G_n^n}{G_{GP}^n}$ and the background the average element-wise standard deviation. The experiment is done with 10^3 networks for a run and inputs defined in (V.21) and $\beta = 1.8$. . .	181
V.4	n-pt deviation calculated as (V.10) normalized for $G_{GP}^{(n)}$ and generated by the activation function 1. Signal represents element of the tensor $m_n = \frac{\Delta G_n^n}{G_{GP}^n}$ and the background the average element-wise standard deviation. The experiment is done with 10^3 networks for a run and inputs defined in (V.22)	182
V.5	n-pt deviation calculated as (V.10) normalized for $G_{GP}^{(n)}$ and generated by the activation function 2. Signal represents element of the tensor $m_n = \frac{\Delta G_n^n}{G_{GP}^n}$ and the background the average element-wise standard deviation. The experiment is done with 10^3 networks for a run and inputs defined in (V.22) and $\beta = 1.8$. . .	183
V.6	n-pt deviation calculated as (V.10) normalized for $G_{GP}^{(n)}$ and generated by the activation function 1. Signal represents element of the tensor $m_n = \frac{\Delta G_n^n}{G_{GP}^n}$ and the background the average element-wise standard deviation. The experiment is done with 10^3 networks for 10 run and inputs defined in (V.21)	184

V.7	n-pt deviation calculated as (V.10) normalized for $G_{GP}^{(n)}$ and generated by the activation function 1. Signal represents element of the tensor $m_n = \frac{\Delta G_n^n}{G_{GP}^n}$ and the background the average element-wise standard deviation. The experiment is done with 10^3 networks for 10 run and inputs defined in (V.22).	185
V.8	n-pt deviation calculated as (V.10) normalized for $G_{GP}^{(n)}$ and generated by the activation function 2. Signal represents element of the tensor $m_n = \frac{\Delta G_n^n}{G_{GP}^n}$ and the background the average element-wise standard deviation. The experiment is done with 10^3 networks for 10 run and inputs defined in (V.21).	186
V.9	n-pt deviation calculated as (V.10) normalized for $G_{GP}^{(n)}$ and generated by the activation function 2. Signal represents element of the tensor $m_n = \frac{\Delta G_n^n}{G_{GP}^n}$ and the background the average element-wise standard deviation. The experiment is done with 10^3 networks for 10 run and inputs defined in (V.22).	187

List of Tables

I.1	Mean squared errors and absolute mean errors for the prediction of Fat Fraction (standard deviation (SD) in round brackets)	29
I.2	Mean squared errors and absolute mean errors for the prediction of Water T2 (standard deviation (SD) in round brackets). MAE in T2 scale column reports the MAE rescaled to physical units, milliseconds(ms).	30
I.3	Mean squared errors and absolute mean errors for the prediction of FF (standard deviation (SD) in round brackets).	34
I.4	Mean squared errors and absolute mean errors for the prediction of wT2 (standard deviation (SD) in round brackets). The column "MAE in T2 scale" reports the MAE rescaled to physical units, milliseconds(ms).	34
II.1	workflow 1 (II.2.1.1): Evaluation of ML models predicting performances: mean absolute discrepancy (MAE) between the muscle-wise Fat Fraction gold standard values from Fatty Riot algorithm and the predicted value through ML algorithms. S.D. is reported in round brackets.	51
II.2	workflow 2 (II.2.1.2): Evaluation of ML models predicting performances: mean absolute discrepancy (MAE) between the muscle-wise Fat Fraction gold standard values from Fatty Riot algorithm and the predicted value through ML algorithms. S.D. is reported in round brackets.	52

II.3	workflow 3 (II.2.1.3): Evaluation of ML models predicting performances: mean absolute discrepancy (MAE) between the muscle-wise Fat Fraction gold standard values from Fatty Riot algorithm and the predicted value through ML algorithms. S.D. is reported in round brackets.	52
II.4	workflow 1 (II.2.1.1): Evaluation of ML models predicting performances: mean absolute discrepancy (MAE expressed in ms) between the muscle-wise water T2 gold standard values from EPG signal simulation algorithm and the predicted value through ML algorithms. S.D. is reported in round brackets.	52
II.5	workflow 2 (II.2.1.2): Evaluation of ML models predicting performances: mean absolute discrepancy (MAE expressed in ms) between the muscle-wise water T2 gold standard values from EPG signal simulation algorithm and the predicted value through ML algorithms. S.D. is reported in round brackets.	52
II.6	workflow 3 (II.2.1.3): Evaluation of ML models predicting performances: mean absolute discrepancy (MAE expressed in ms) between the muscle-wise water T2 gold standard values from EPG signal simulation algorithm and the predicted value through ML algorithms. S.D. is reported in round brackets.	53
II.7	Pearson and Spearman correlation coefficients between volume CVs, ground truth CVs and KNN MAE prediction of neuromuscular parameters. P-values are reported in round brackets with a significant level set at $p \leq 0.05$. KNN FF prediction for Pe muscle was not included to evaluate Pearson and Spearman correlations because it resulted to be an outliers of KNN FF MAE distribution.	53
III.1	Receptive fields associated to each convolutional operation in the successive residual blocks RB_l	82
III.2	Model accuracy after 40 epochs	89

III.3	Average DSC for the 10 test subjects, with an indication of their	
	disease severity 93
III.4	DSC for the 4 additional slices for Subject A and Subject B	. . . 96
IV.1	We report for each parameter the best fitted Beta distribution	
	characterised by the constants (c_1, c_2) in the third column and	
	the range of definition in the second column (the x_L range is	
	scaled by a quantity of 10^5). The quantification of the goodness	
	of the theoretical representations is given by KS-pvalue in the last	
	column 133

Introduction

Medicine is an evolving field that takes advantage of the recent progress of a broad spectrum of sciences such as biology, chemistry, statistics, mathematics, engineering with the aim of preventing, diagnosing and treating a wide range of medical conditions (Tuena et al. [2020](#)).

Emerging, high-volume data, derived by the implementation of high-throughput biomedical assays, such as DNA sequences and imaging protocols, are showing a great inter-individual variability with respect to the effects and mechanisms that contribute to disease processes (Goetz and Schork [2018](#)). This paves the way for the development of personalized and precision medicine which refers to the idea of delivering the right treatment to the right patient at the right time (Colijn et al. [2017](#)).

The aim is to achieve patient stratifications, monitoring and treatment design using quantitative, patient-specific datasets, integrated via algorithmic analyses. This implies embedding diagnostics and treatments with features derived from the so-called “-omics” sciences (genomic, proteomic, metabolomic, radiomics) in order to create complete datasets describing multivariate aspects of individuals’ health across time. Thus, it is also essential to identify measurable and accurate indicators, the biomarkers, which potentially can predict disease initiation and progression. To exploit the potential of such datasets, it is necessary to develop transparent and replicable mathematical frameworks able to describe and/or extract information from high-dimensional, dynamic, noisy and sparsely-sampled processes to highlight time patterns in a disease. For this reason, we need mathematical modeling methods and statistical data analysis algorithms to be robust and able to adapt to errors and uncertainties.

Mathematical modeling can be mechanistic and non-mechanistic, such

as Artificial Intelligence (AI) techniques (Machine Learning (ML) and Deep Learning (DL)). The mechanistic models focus on the description of elements forming a system, their mutual interactions and the interaction with the environment with the possibility to also describe the resulting emerging behavior and average properties of the systems. Among these kinds of models there are the dynamic modeling by ordinary and partial differential equations (ODEs and PDEs) that can give very accurate predictions about process parameter changes in time, including transition process and steady state. These models can also take into account different types of non-linearities generating complex system behavior such as emerging oscillations and instabilities (Stalidzans et al. [2020](#)).

An alternative to ordinary or partial differential equations is stochastic modeling in which the system is considered as a stochastic process. In addition, we can have agent-based modeling that describes biological systems using the concepts of environment, agents (molecules of metabolites, enzymes cells, complex molecules, organisms) which interact mutually and with the surrounding environment. These interaction rules give rise to an emerging and average system behavior. These kind of models also give the opportunities to involve agents with different levels of detail and to obtain multiscale modeling. Simulations and optimization steps are crucial for mechanistic models.

AI models, instead, are based on machine learning algorithms and neural networks and simulate the logical decision-making process taking advantage of available data. These models can predict the behavior of a system searching for relationships between inputs and outputs or identifying specific or recurrent patterns. To train such models, a great amount of available data is fundamental. Anyway, to obtain new insights in a process of interest it is possible to combine different modeling approaches in order to shed light on different aspects of the process or disease under examination.

Several medical fields take advantage from precision medicine and mathematical modeling, to mention a few of them cancer research (Filipp [2017](#)), blood research (Li, Todor, and Luo [2016](#)) and drug discovery (Thiele et al. [2017](#)). In the context of predictive and precision medicine, imaging is a fundamental

technology used in clinical practice to aid decision-making step for screening, diagnostic, and follow-up purposes (Guiot et al. [2022](#)).

Using imaging techniques, in fact, it is possible to extract structural, functional and metabolic information. In particular, MRI is the safest and non-invasive imaging technique that uses strong magnetic fields to create anatomical images with a good spatial resolution. If it is combined with magnetic resonance spectroscopy, it can provide anatomical and biochemical information of a particular region of an organ and, in addition, it can trace differences in oxygenated and deoxygenated hemoglobin giving functional activation information (Tuena et al. [2020](#)).

The quantitative analysis of medical imaging includes the field of Radiomics. The latter allows, after the segmentation of regions of interest (ROIs), the extraction of features that take into account gray-scale intensity level of the image, spatial gray-level distribution information, geometry and shape of the ROIs. Radiomic features can be used as covariates for ML algorithms in order to identify patterns (Han et al. [2020](#)), to regress biomarkers values (Lee et al. [2017](#), Parmar et al. [2015](#)), to solve classification problems (Conti et al. [2021](#)), Rastegar et al. [2020](#)) and to define the best treatment (Arimura et al. [2019](#)). For further application see Parekh and Jacobs [2019](#) and Lambin et al. [2017](#).

Recently, due to the necessity of minimizing the pre-processing, speeding-up the segmentation steps and solving classification problems in addition to identification of specific patterns with high resolution, DL has become largely used in medicine (Santos et al. [2019](#)). Several DL applications in medicine can be found in the reviews Bakator and Radosav [2018](#) and Akay and Hess [2019](#).

In the described framework, it falls the present thesis. It addresses the possibility of using mathematical methods, simulation techniques, repurposed physical theories and artificial intelligence algorithms to fulfill clinical needs in neuroradiology and neurology with the aim to predict disease patterns and its evolution over time as well as to support clinical decision-making process. The thesis is divided in three parts.

Part 1 is about answering the clinical necessity of identifying and under-

standing patterns and time evolution of neuromuscular diseases, with special focus on Facioscapulohumeral dystrophy (FSHD), in order to guide and support clinical decision procedure. Taking advantage of MRI imaging, a combination of Radiomics and ML algorithms is developed with the aim to predict Fat Fraction (FF) and water T2 (wT2) biomarkers that are suitable to quantify muscle fat replacement and muscle inflammation (Güttsches et al. [2021](#)). The implemented workflow involves MRI images acquired at thigh and calf muscles level. The goal of the works reported in the Part 1 is to deliver a radiomic and ML workflow that can predict with good accuracy quantitative MRI parameters relying on conventional, time-saving MRI sequences routinely available in most neuromuscular centers. To achieve the goal we need to face the muscles' segmentation process. To speed-up this step we automatized it by introducing a convolutional neural network (CNN) with a contracting-expanding topology in order to achieve deep feature extraction (contracting part) from increasingly compressed levels of resolution and different spatial aggregation levels (receptive fields) and resolution decompression and consequently segmentation (expanding part). The output is designed to return the segmentation map of thigh and calf muscles.

Part 2 describes the development of a kinetic model of tumor growth, with a special focus on glioblastomas. In Paper [IV](#) we describe tumor cells' growth within a statistical approach based on the physical kinetic theory, or rather in terms of evolution of a distribution function. The proposed mathematical description is a kind of agent based model and it relies on Boltzmann-type model in which statistical behavior of the system, *i.e.* tumor, is mainly related to the interaction between agents, *i.e.* cells, and surrounding environments at microscopic level without taking into account agents internal complex structure. Elementary transitions occurring at the cellular level, incorporating environmental clues and random fluctuations, generate a temporal variation of such distribution coherently, in suitable limits, with the well-known ODE-based growth models (Benzekry et al. [2014](#)). In order to give a more realistic description of tumor growth, we also introduce uncertainties related to

a limited set of observations, tumor segmentation process and different subject body response, even if this increases the dimensionality of the resulting kinetic problem and it influences the equilibrium state, *i.e.*, the solution of the associated Fokker-Planck-type equation. Concerning a specific choice of parameters, the tail of the equilibrium distributions (generalized Gamma distribution, lognormal-type distribution or Amoroso-type distribution) is connected to the probability of having tumors of size bigger than a given alerting size. Suitable selective-type controls acting at the level of cellular dynamics are used to investigate the action of therapeutic protocols trying to reduce the volume size of tumors. The problem of finding the optimal control is solved at the microscopic level and studied at the mesoscopic scale through classical methods of kinetic theory and it gives as results an equilibrium distribution with modified tails. Proper numerical methods, based on stochastic Galerkin formulation of the derived kinetic equations, are introduced for uncertainty quantification of the resulting kinetic model. Our proposed approach is multiscale since it connects actions on individual cellular-based dynamics to observable patterns in a cohort of patients.

Part 3 is related to a still on-going project that attempts to combine quantum field theory and neural networks to describe and simulate the behavior of a brain portion. In this part, we try to describe a brain portion through a scalar bosonic self-interacting field theory. Because of the connection between quantum field theory and neural network underlyed by Halverson, Maiti, and Stoner [2021](#) we construct a finite neural network to simulate the brain portion by defining an *ad-hoc* activation function inspired to the biological neuron model response function in the case in which a brain neuron is modeled as a Resistance-Capacity (RC) circuit. We come out with conclusion that, under suitable conditions, a brain portion can be well approximated through a Gaussian process on the function space, or rather through an non-interagent field theory, $N(\mu, \Xi^{-1})$ where the covariance is the Feynman propagator for the theory. The introduced quantum field framework is also applicable to the case of Non-Gaussian Process behavior, or rather to an interacting quantum field theory in a Wilsonian Effective Field

theory approach.

Summary of papers published or in preparation that are reported in the thesis

Paper I proposes a Radiomic workflow combined with Machine Learning algorithms applied to MR images to predict Fat Fraction and water T2 biomarkers in patients affected by Facioscapulohumeral Dystrophy .

Paper II describes a pilot study to predict quantitative qMRI parameters, Fat Fraction and water T2, from conventional STIR imaging.

Paper III proposes a deep learning approach based on a Convolutional Neural Network to segment the thigh's and leg's muscles on MRI images.

Paper IV proposes a kinetic model of tumor growth taking into account the effects of clinical uncertainties characterising the tumour progression.

Paper V introduces a first attempt to combine quantum field theory and neural networks to describe a brain portion.

References

- Akay, A. and Hess, H. (2019). “Deep learning: current and emerging applications in medicine and technology”. In: *IEEE journal of biomedical and health informatics* vol. 23, no. 3, pp. 906–920.
- Arimura, H. et al. (2019). “Radiomics with artificial intelligence for precision medicine in radiation therapy”. In: *Journal of radiation research* vol. 60, no. 1, pp. 150–157.
- Bakator, M. and Radosav, D. (2018). “Deep learning and medical diagnosis: A review of literature”. In: *Multimodal Technologies and Interaction* vol. 2, no. 3, p. 47.

- Benzekry, S. et al. (2014). “Classical mathematical models for description and prediction of experimental tumor growth”. In: *PLoS computational biology* vol. 10, no. 8, e1003800.
- Colijn, C. et al. (2017). “Toward precision healthcare: context and mathematical challenges”. In: *Frontiers in physiology* vol. 8, p. 136.
- Conti, A. et al. (2021). “Radiomics in breast cancer classification and prediction”. In: *Seminars in cancer biology*. Vol. 72. Elsevier, pp. 238–250.
- Filipp, F. V. (2017). “Precision medicine driven by cancer systems biology”. In: *Cancer and Metastasis Reviews* vol. 36, no. 1, pp. 91–108.
- Goetz, L. H. and Schork, N. J. (2018). “Personalized medicine: motivation, challenges, and progress”. In: *Fertility and sterility* vol. 109, no. 6, pp. 952–963.
- Guiot, J. et al. (2022). “A review in radiomics: Making personalized medicine a reality via routine imaging”. In: *Medicinal Research Reviews* vol. 42, no. 1, pp. 426–440.
- Güttsches, A.-K. et al. (2021). “Quantitative muscle-MRI correlates with histopathology in skeletal muscle biopsies”. In: *Journal of Neuromuscular Diseases* vol. 8, no. 4, pp. 669–678.
- Halverson, J., Maiti, A., and Stoner, K. (2021). “Neural networks and quantum field theory”. In: *Machine Learning: Science and Technology* vol. 2, no. 3, p. 035002.
- Han, Y. et al. (2020). “Identification of predominant histopathological growth patterns of colorectal liver metastasis by multi-habitat and multi-sequence based radiomics analysis”. In: *Frontiers in oncology* vol. 10, p. 1363.
- Lambin, P. et al. (2017). “Radiomics: the bridge between medical imaging and personalized medicine”. In: *Nature reviews Clinical oncology* vol. 14, no. 12, pp. 749–762.
- Lee, G. et al. (2017). “Radiomics and its emerging role in lung cancer research, imaging biomarkers and clinical management: state of the art”. In: *European journal of radiology* vol. 86, pp. 297–307.

- Li, S., Todor, A., and Luo, R. (2016). “Blood transcriptomics and metabolomics for personalized medicine”. In: *Computational and structural biotechnology journal* vol. 14, pp. 1–7.
- Parekh, V. S. and Jacobs, M. A. (2019). “Deep learning and radiomics in precision medicine”. In: *Expert review of precision medicine and drug development* vol. 4, no. 2, pp. 59–72.
- Parmar, C. et al. (2015). “Machine learning methods for quantitative radiomic biomarkers”. In: *Scientific reports* vol. 5, no. 1, pp. 1–11.
- Rastegar, S. et al. (2020). “Radiomics for classification of bone mineral loss: A machine learning study”. In: *Diagnostic and interventional imaging* vol. 101, no. 9, pp. 599–610.
- Santos, M. K. et al. (2019). “Artificial intelligence, machine learning, computer-aided diagnosis, and radiomics: advances in imaging towards to precision medicine”. In: *Radiologia brasileira* vol. 52, pp. 387–396.
- Stalidzans, E. et al. (2020). “Mechanistic modeling and multiscale applications for precision medicine: theory and practice”. In: *Network and Systems Medicine* vol. 3, no. 1, pp. 36–56.
- Thiele, I. et al. (2017). “Quantitative systems pharmacology and the personalized drug–microbiota–diet axis”. In: *Current Opinion in Systems Biology* vol. 4, pp. 43–52.
- Tuena, C. et al. (2020). “Predictive Precision Medicine: Towards the Computational Challenge”. In: *P5 eHealth: An Agenda for the Health Technologies of the Future*. Ed. by Pravettoni, G. and Triberti, S. Cham: Springer International Publishing, pp. 71–86.

Part 1

Magnetic Resonance Imaging,
Artificial Intelligence and
Radiomics for the
Quantification of
neuromuscular biomarkers: a
special focus on
Facioscapulohumeral
dystrophy

Introduction

Neuromuscular diseases are a broadly defined group of disorders characterized by dysfunction and injury of peripheral nerves or muscle. In muscular dystrophies, skeletal muscle undergoes several pathophysiological processes encompassing necrosis, inflammation, fibrosis, and finally replacement by adipose tissue as reported in X. Deligianni et al. [2022]. Among genetic muscular disorders, facioscapulohumeral muscular dystrophy (FSHD) is the second most common disease in adults defined by a stepwise, asymmetric and generally slow wasting and weakness progression of the facioscapulohumeral, abdominal, paraspinial and lower leg muscles (Andersen et al. [2017]; Dahlqvist et al. [2015]; Tawil et al. [2015]).

Identifying an accurate diagnosis for patients with genetic and inflammatory muscular disorders is not easy due to the clinical and genetic heterogeneity of myopathies. Regarding neuromuscular dystrophies, a very powerful and non-invasive tool for the diagnosis and the assessment of disease progression is the muscle Magnetic Resonance Imaging (MRI), which allows the spatial localization of the Nuclear Magnetic Resonance signal and consequently the construction of an image. In most of the medical MRI applications, hydrogens (H^1) are the nuclei being probed because of their natural abundance in human body.

To understand the MR image formation and how it brings information, we need to briefly refer to the physics behind it. H^1 nuclei, as quantum mechanics entities, have a nuclear spin or rather the intrinsic total angular momentum of the nucleus, obtained by the geometric composition of the total magnetic moments of the nucleons inside it. When the external magnetic field is zero, the nuclear magnetic moment can be oriented along one of the possible allowed directions.

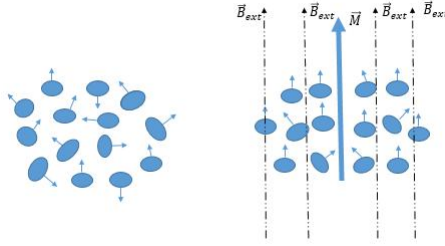


Figure 0.1: $B_{ext} = 0$ (left) the spins are oriented in random way and \vec{M} is zero. $B_{ext} \neq 0$ (right) few spins are aligned along the external field direction: the \vec{M} in this case is different from zero and it is oriented along the axis of the external magnetic field.

When an external magnetic field is applied, nuclear spins do a precession along the field direction, which corresponds to the minimum level of the system potential energy. Since it is impossible to follow each single spin behaviour of the sample under examination, the Magnetization vector \vec{M} is introduced in order to take into account for the mean of the magnetic moments per unit volume. In absence of the external magnetic field the total Magnetization is also zero, since each magnetic moment tends to precesses in a random way due to thermal agitation. When an external magnetic field is applied to the system, few spins tend to align themselves with the external magnetic field direction: \vec{M} is different from zero in this case and it has the same direction of the applied magnetic fields (see Figure [0.1](#)). To detect the magnetic static and dynamical properties of the sample under examination, we need to perturb the system that means to push \vec{M} direction away from the direction of the external magnetic field, *i.e.* from its longitudinal direction.

As \vec{M} precesses around the external magnetic field, it produces a change of magnetic field flux. According to Faraday law the time-varying magnetic flux induces in a receiving coil a voltage or an electromotive force (efm), *i.e.* an energy transferred per unit of electric charge to the coil. The derived electrical current is the signal exploited in MRI. The detected signal oscillate at the Larmor frequency (that is the frequency with which an H^1 precesses in a magnetic field and it depends linearly on the external static magnetic field

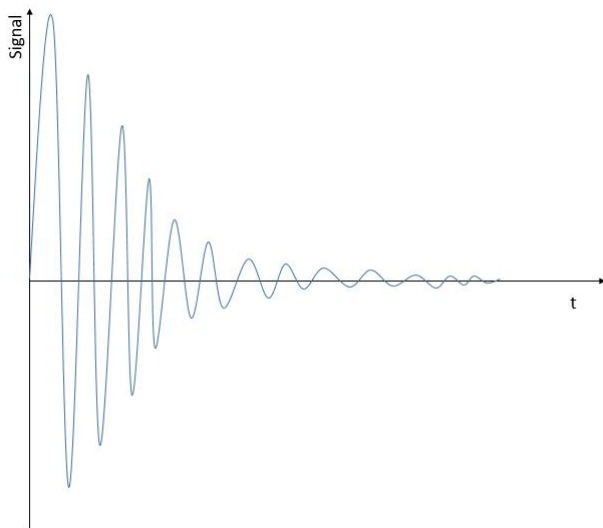


Figure 0.2: Free Induction Decay (FID). The detected signal is reported on the y-axis and the time t on the x-axis. The signal oscillates with the Larmor frequency and it decays exponentially with a time constant $T2^*$.

(Brown et al. 2014) and it decays exponentially with a time constant $T2^*$, producing the so-called free induction decay (FID) signal (see Figure 0.2).

To shift away the magnetization vector from the external magnetic field direction, it is necessary to apply a radiofrequency (rf) magnetic field for a short time, *i.e.* an rf pulse. The rf frequency is tuned to the Larmor frequency so that the resonance conditions are satisfied.

The resonance phenomenon allows the system to absorb energy and to undergo transition between the allowed nuclear states¹. The release of this absorbed energy causes the so called \vec{M} relaxation. The temporal evolution of \vec{M} is described by the solutions of the Bloch equations (see Brown et al. 2014), which incorporate both longitudinal and transversal relaxation effects characterized by T1 and T2 time constants respectively. The longitudinal relaxation is connected to the 'spin-lattice' interactions, or rather to the energy transfer to

¹For material with unpaired electrons, such as metal complexes and organic radicals, Electron paramagnetic resonance (EPR) can be used. EPR relies on the same basic concept of nuclear magnetic resonance, but the spins excited are those of the electrons instead of atomic nuclei

the surrounding macromolecules resulting from individual spin states flipping in the magnetic field, due to perturbations from the surrounding environment, and accompanied by the emission of a photon of energy proportional to the Larmor frequency (Ansoorge and Graves [2016](#)). Transversal relaxation is connected to 'spin-spin' interactions which causes a loss of coherence between different spins due to variations in the local spin precessional frequencies (Brown et al. [2014](#)). In general, the external magnetic field acting on the sample volume has some inhomogeneities that translate in additional spin dephasing in the transverse plane. This means that the signal decay rate is characterized by $T2^*$, with $T2^* < T2$.

To create an image, it is necessary to correlate a series of signal measurements with the spatial locations of the different sources. If the static external field is uniform, the total signal incorporates information about all spins regardless of their spatial location. To introduce a spatial information it is necessary to spatially change the magnetic field across the sample. In this way, the resulting signal has spatially varying frequency components along the direction of the field gradient. Therefore, the spectral components represent spatial information and so a mapping of the signal from the signal space to the image position space could be performed with a Fourier transform.

MR techniques allows the generation of images with different levels of contrast taking advantage of the large set of variables that can be adjusted. To mention a few, proton or spin density, relaxation time constants, proton motion, chemical shift, Larmor frequencies, contrast enhancing agents, diffusion (Brown et al. [2014](#)).

The MRI signal $s(t)$ from a material or a tissue is $s(t) \sim \rho_0(1 - e^{-T_R/T_1})e^{-T_E/T_2^*}$, where ρ_0 is proton or spin density, T_1 and T_2^* the relaxation times, T_E [2](#) the *echo time* and T_R the *repetition time* [3](#). Therefore, the most basic mechanisms that generate contrast are related to tissue differences in spin density and T_1

² T_E refers to the time between the application of the radiofrequency excitation pulse and the peak of the signal induced in the coil.

³ T_R is the time from the application of an excitation pulse to the application of the next pulse

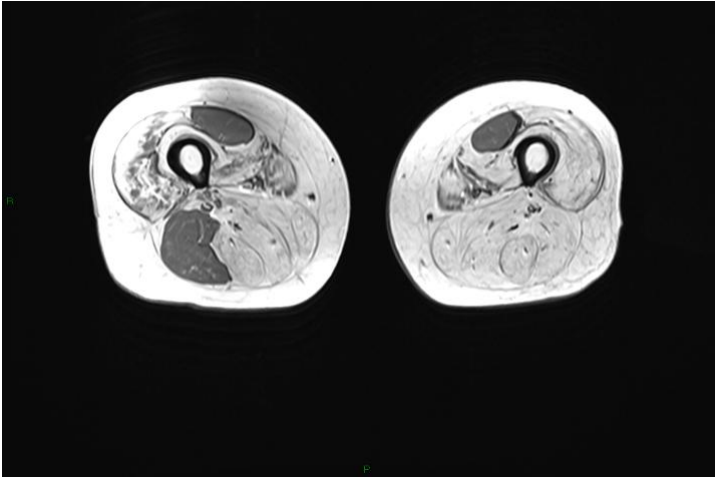


Figure 0.3: T_1 -weighted image related to Facioscapulohumeral muscular dystrophy patient and acquired with a T_1 -turbo Spin Echo at Neuroradiology Department of IRCCS Fondazione Mondino.

and T_2 time constants (Brown et al. [2014](#)), once the appropriated combination for T_E , T_R is considered. In particular, T_1 and T_2 constants are sensitive to local environments of proton spins so the T_1 -weighted and T_2 -weighted MRI can differentiate and characterize the human tissue types (Ansorge and Graves [2016](#)). T_1 -weighted contrast is a powerful method for delineation of different tissues, since T_1 values of normal soft tissues are different from one another. T_2 -weighted images, instead, play an important role when local magnetic field susceptibility differences between tissues are present. Besides, T_2 is found to be a sensitive indicator of disease (Brown et al. [2014](#)).

Weighted- T_1 and - T_2 images in neuromuscular disorders promote macroscopic evaluation of morphological changes of the muscles, including fat replacement and edema. Therefore, muscle MRI protocols routinely include T_1 -weighted images (see Figure [0.3](#)) and sequences sensitive to tissue water, as short-tau inversion recovery (STIR) (see Figure [0.4](#)) or T_2 -weighted images, with or without suppression of the signal of fat tissue (Paoletti et al. [2019](#))

More in detail, axial T_1 -Turbo Spin Echo (TSE) weighted sequence shows the severity and the distribution of the tissue damage highlighting the selective

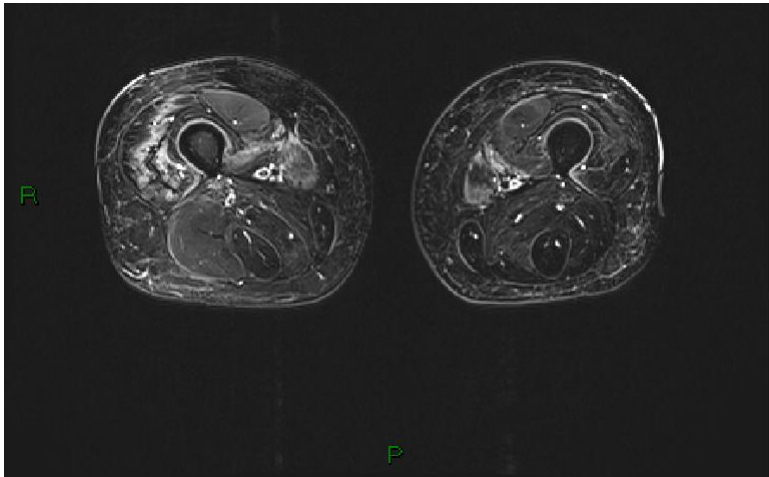


Figure 0.4: T_2 -weighted image related to a Facioscapulohumeral muscular dystrophy patient and acquired with STIR sequence at Neuroradiology Department of IRCCS Fondazione Mondino.

pattern of the muscle involvement in different hereditary and inflammatory muscle disorders, whereas STIR sequence is able to point out fat replacement and muscle edema (or edema -like) patterns.

Improvements in MRI techniques combined with post-processing software solutions pave the way for quantitative assessment of the pathological changes in neuromuscular disorders. The identification of quantitative features, *i.e.*, biomarkers, that bring information regarding muscle atrophy and the extent of active and chronic degenerative changes is the goal of quantitative MRI (qMRI). In neuromuscular disorders, expression of muscle degeneration and of *in vivo* indicator of ongoing disease activity is given through the quantitative parameters Fat Fraction (FF), *i.e.*, the percentage of fat replacement of the muscle, and the muscle water T_2 relaxation time (wT_2) respectively. FF is usually obtained from Dixon imaging whereas wT_2 by a multi-echo spin-echo relaxometry, after removing fat signal contribution (Carlier et al. [2016](#)). These neuromuscular quantitative biomarkers have the largest acceptance among researches because they show promising correlation with histopathological changes (Güttsches et al. [2021](#)). Reliable quantitative measurements from MRI

imply vendor-provided custom-tailored qMRI sequences and complex, high-cost technical implementations on the MRI scanner. For this reason qMRI methods are unavailable in many clinical centers and the combination of conventional MRI and semiquantitative scales is still used in routinely clinical practice.

A possible solution to that has arisen in the last years with Radiomics. The latter quantifies textural information by mathematical extraction of pixels intensity and spatial interrelationships distributions, highlighting the main patterns of a disease. The combination of Radiomics and Artificial Intelligence (AI) seems to be a promising tool to make diagnosis and to support clinical decision-making process in different medical fields, especially in the field of quantitative imaging as reported in M. Monforte et al. [2019]; Timmeren et al. [2020] and Felisaz et al. [2021]. To address the need of easily obtaining qMRI parameters, in the following studies a specific workflow combining radiomics and AI is introduced with the aim to take advantage of the conventional MR images available in most neuromuscular centers. In particular, in paper I we implement machine-learning regressors to predict the thigh mean value of wT2 and FF in patient affected by FSHD, starting from texture analysis of the 8-th echo of Multi-echo Spin-echo (MESE) sequence considered as conventional, non-quantitative images. In the paper II we take advantage of the time-saving STIR imaging method to find a workflow that can provide the best predictions for calf-muscles FF and wT2, comparing ML-based radiomics approach, also used in the previous work, with the implementation of two new easy-to-compute radiomics indexes that quantify fat infiltration grade and the muscle edema, respectively, then used as covariates in ML algorithms.

A crucial point in extracting quantitative information from MRI in the context of ML and radiomics based workflows is the segmentation process. It consists in drawing precision regions of interest (ROIs) on MR images. Up to now, manual drawing of ROIs has been considered the gold standard. However, it is a time-consuming process and it requires dedicated and trained human operators (Barnouin et al. [2014]; Breiman et al. [2017]). Particularly promising in facilitating and accelerating the segmentation process is the implementation

of automatic tools based on machine learning and more recently on deep learning (Ogier et al. 2021). As a further step towards the automatization of muscle ROI drawing we implemented a convolutional neural network with a contracting-expanding topology, as reported in paper [III] to obtain deep features extraction from increasingly compressed levels of resolution and different spatial aggregation levels on the initial MR images (contracting part) and resolution decompression and segmentation (expanding part). The purpose is to create an automatic tool for single-muscle segmentation maps at thigh and calf level.

The works presented in this chapter support the usefulness of combining radiomics, artificial intelligence and MRI to introduce new and powerful workflows that could help and drive clinical decision process, especially in the neuromuscular fields. Particularly, the introduced workflows allow disease diagnosis and progression evaluation using conventional sequences, with the advantage of getting quantitative MRI parameters in an enlarged cohort of clinical center in addition to the possibility of eventually reduce the MRI acquisition scan time.

References

- Andersen, G. et al. (2017). “MRI as outcome measure in facioscapulohumeral muscular dystrophy: 1-year follow-up of 45 patients”. In: *J. Neurol.*
- Ansorge, Richard and Graves, Martin (2016). *The physics and mathematics of MRI*. Morgan & Claypool Publishers.
- Barnouin, Y. et al. (2014). “ Manual segmentation of individual muscles of the quadriceps Femoris using MRI: a reappraisal”. In: *J Magn Reson Imaging* vol. 40, pp. 239–247.
- Breiman, L. et al. (2017). *Classification and regression trees*. Routledge.
- Brown, Robert W et al. (2014). *Magnetic resonance imaging: physical principles and sequence design*. John Wiley & Sons.

- Carrier, P. et al. (2016). “Skeletal muscle quantitative nuclear magnetic resonance imaging and spectroscopy as an outcome measure for clinical trials”. In: *J Neuromuscul Dis.* vol. 3, pp. 1–28.
- Dahlqvist, J. et al. (2015). “Severe paraspinal muscle involvement in facioscapulohumeral muscular dystrophy”. In: *Neurology.*
- Deligianni, X. et al. (2022). “Dynamic magnetic resonance imaging of muscle contraction in facioscapulohumeral muscular dystrophy”. In: *Sci Rep.* vol. 12(1).
- Felisaz, Paolo Florent et al. (2021). “Texture analysis and machine learning to predict water T2 and fat fraction from non-quantitative MRI of thigh muscles in Facioscapulohumeral muscular dystrophy”. In: *European Journal of Radiology* vol. 134, p. 109460.
- Güttsches, A.K. et al. (2021). “Quantitative Muscle-MRI Correlates with Histopathology in Skeletal Muscle Biopsies”. In: *J Neuromuscul Dis.* vol. 8(4), pp. 669–678.
- Monforte, M. et al. (2019). “Tracking muscle wasting and disease activity in facioscapulohumeral muscular dystrophy by qualitative longitudinal imaging.” In: *J. Cachexia. Sarcopenia Muscle.*
- Ogier, A.C. et al. (2021). “SOver- view of MR image segmentation strategies in neuromuscular disorders.” In: *Front Neurol.*
- Paoletti, M et al. (2019). “Advances in Quantitative Imaging of Genetic and Acquired Myopathies: Clinical Applications and Perspectives”. In: *Frontiers in Neurology* vol. 10.
- Tawil, R. et al. (2015). “Evidence-based guideline summary: Evaluation, diagnosis, and management of facioscapulohumeral muscular dystrophy: Report of the Guide-line Development, Dissemination, and Implementation Subcommittee of the American Academy of Neurology and the Practice Issues Review Panel of the American Association of Neuromuscular Electrodagnostic Medicine”. In: *Neurology.*
- Timmeren, J. van et al. (2020). “Radiomics in medical imaging-”how-to” guide and critical reflection.” In: *J Neuromuscul Dis.*

Paper I

Texture analysis and machine learning to predict water T2 and fat fraction from non-quantitative MRI of thigh muscles in Facioscapulohumeral muscular dystrophy

Paolo Florent Felisaz^{a,b,*},¹, Giulia Colelli^{a,c},¹, Elena Ballante^{c,d}, Francesca Solazzo^a, Matteo Paoletti^a, Giancarlo Germani^a, Francesco Santini^{e,f}, Xeni Deligianni^{e,f}, Niels Bersglund^{g,h}, Mauro Monforteⁱ, Giorgio Tascaⁱ, Enzo Ricciⁱ, Stefano Bastianello^{a,j}, Silvia Figini^k,², Anna Pichiecchio^{a,j},²

Published in *European Journal of Radiology*, January 2021, DOI: [10.1016/j.ejrad.2020.109460](https://doi.org/10.1016/j.ejrad.2020.109460)

Abstract

^a Department of Neuroradiology, IRCCS Mondino Foundation, Pavia, Italy
^b Department of Radiology, Desio Hospital, ASST Monza, Desio, Italy
^c Department of Mathematics, University of Pavia, Pavia, Italy
^d BioData Science Center, IRCCS Mondino Foundation, Pavia, Italy
^e Department of Radiology, Division of Radiological Physics, University Hospital Basel, Basel,

Purpose: Quantitative MRI (qMRI) plays a crucial role for assessing disease progression and treatment response in neuromuscular disorders, but the required MRI sequences are not routinely available in every center. The aim of this study was to predict qMRI values of water T2 (wT2) and fat fraction (FF) from conventional MRI, using texture analysis and machine learning.

Method: Fourteen patients affected by Facioscapulohumeral muscular dystrophy were imaged at both thighs using conventional and quantitative MR sequences. Muscle FF and wT2 were calculated for each muscle of the thighs. Forty-seven texture features were extracted for each muscle on the images obtained with conventional MRI. Multiple machine learning regressors were trained to predict qMRI values from the texture analysis dataset.

Results: Eight machine learning methods (linear, ridge and lasso regression, tree, random forest (RF), generalized additive model (GAM), k-nearest-neighbor (kNN) and support vector machine (SVM) provided mean absolute errors ranging from 0.110 to 0.133 for FF and 0.068 to 0.115 for wT2. The most accurate methods were RF, SVM and kNN to predict FF, and tree, RF and kNN to predict wT2.

Conclusion: This study demonstrates that it is possible to estimate with good accuracy qMRI parameters starting from texture analysis of conventional MRI.

Keywords: FSHD; MRI; Machine learning; Muscle; Quantitative; Texture

Switzerland

^f Department of Biomedical Engineering, University of Basel, Basel, Switzerland

^g Buffalo Neuroimaging Analysis Center, Department of Neurology, Jacobs School of Medicine and Biomedical Sciences, University at Buffalo, State University of New York, Buffalo, NY, USA

^h IRCCS, Fondazione Don Carlo Gnocchi, Milan, Italy

ⁱ Unita Operativa Complessa di Neurologia, Fondazione Policlinico Universitario A. Gemelli IRCCS, Rome, Italy

^j Department of Brain and Behavioral Sciences, University of Pavia, Pavia, PV, Italy

^k Department of Political and Social Sciences, University of Pavia, Pavia, PV, Italy

I.1 Introduction

Quantitative Magnetic Resonance Imaging (qMRI) is a useful non-invasive diagnostic tool in the field of neuromuscular diseases, providing clinically relevant parameters, such as Fat Fraction (FF) and muscle water T2 (wT2) (Paoletti et al. [2019](#); Strijkers et al. [2019](#)). These parameters provide sensitive measures of muscle damage and are aimed toward having a prognostic role. In fact, they could be used to track disease progression or response to treatments (Mul et al. [2017](#)). However, implementing qMRI protocols is challenging in terms of technical requirements and financial resources, thus they are not accessible in every neuromuscular center. Instead, conventional (non-quantitative) MRI is much more widespread. Conventional sequences in diagnostic protocols for muscle MRI usually include T1-weighted images and water sensitive sequences, such as STIR or T2-weighted with or without fat suppression (Chardon et al. [2019](#)). These conventional sequences are devoted to the macroscopic evaluation of fat replacement and muscle edema. Semi-quantitative rating scales are used clinically based on visual inspection, the most commonly used being the Fischer and Mercuri scales (Guggenberger et al. [2013](#); Mercuri et al. [2002](#)).

Fascioscapulohumeral muscular dystrophy (FSHD) is one of the most common muscular dystrophies and is characterized by a progressive asymmetric loss of strength and atrophy of skeletal muscles (Emery [1991](#); Wattjes, Kley, and Fischer [2010](#)). Weakness usually affects first the facial and shoulder girdle muscles and then abdominal, upper and lower limbs. Conventional MRI is used for distinguishing FSHD from other myopathies and measuring disease severity with the common grading scales (Tasca et al. [2016](#)), as well as for semi-quantitatively assessing disease activity (Monforte et al. [2019](#)). qMRI instead can potentially aid in the follow-up of patients with FSHD (Janssen et al. [2016](#)).

Texture analysis can extract quantitative features from qualitative images. These textural features are descriptors of the pixel intensity variation and distribution within an image and are related to human discriminable visual

patterns, such as contrast and granularity (Haralick, Dinstein, and Shanmugam 1973).

They are commonly processed with machine learning algorithms to predict clinically useful outcomes after training from a dataset. Basically, they can fall within two broad categories: classifiers, aimed to predict discrete outcomes, for instance benign versus malignant or a particular grade of pathology, and regressors, aimed to predict continuous variables such as survival time or a quantitative biomarker.

The aim of this paper was to use machine-learning regressors to predict wT2 and FF starting from texture analysis of non-quantitative MRI sequences. We used a dataset of MRI scans from patients affected by FSHD with different degrees of intramuscular fatty replacement and edema. A cross validation framework was set to test and compare multiple parametric and nonparametric machine learning models, including linear regression, ridge regression, lasso regression, regression tree, random forest (RF), generalized additive model (GAM), support vector machine (SVM) and k-nearest neighbor (kNN).

I.2 Methods

I.2.1 Study design and participants

The study was approved by the local ethics committee and all the participants provided written informed consent. Fourteen patients affected by FSHD (11 men, 3 women, mean age 45.6 years, range 32–60) were recruited in a longitudinal study and imaged at the thigh level every six months. Seven patients were imaged 3 times, four patients were imaged twice and three were imaged once, for a total of 32 examinations. Patients had different grades of muscular involvement as per the clinical severity scale (CSS median 3.5, 95 % CI for the median 2.95–4.00) and the 6 min walking test at the first time point (6MWT mean 410 min, range 65–57, SD 146).

I.2.2 MR protocols

All examinations were performed on a 3T scanner (Skyra, Siemens AG Erlangen, Germany) using integrated spine and body surface coils. Acquisition volumes were centered on the thigh muscles at a standardized position (the last slice of the box was located at 10 cm proximally from the upper base of the patella). The protocol included a 3D 6-point multi-echo gradient echo sequence with shifted echo times (MEGE, matrix size = 432×396 ; 52 slices, TR = 35 ms; TE = 1.7–9.2 ms; resolution = $1.0 \times 1.0 \times 5\text{mm}^3$, total scan time = 6 min) and a multiecho spin echo sequence (MESE TE = 10.9 ms, TR = 4100.0 ms, 17 echo times; resolution = $1.2 \times 1.2 \times 10.0\text{mm}^3$; gap 30 mm, 5 slices). The Fatty Riot algorithm was used offline for the calculation of fat/water fraction maps from the MEGE sequence (Welch et al. [2013](#)). For the MESE sequence, extended phase graph signal simulation including slice profile was implemented offline in Python (Python Software Foundation. Python Language Reference, version 3.8) (Marty et al. [2016](#); Weigel [2015](#)).

I.2.3 Image processing and texture analysis

One operator drew regions of interest (ROIs) for each muscle of the thigh using the images of the first echo obtained from the MESE sequence. 12 muscle ROIs per side were drawn on each slice, for a total of 12 ROIs per examination (See Figure [I.1](#)). The ROIs were co-registered to the MEGE images with creation of new corresponding MEGE ROIs, and then manually adjusted by the same operator. FF and wT2 mean values were extracted from each ROI from the MESE and MEGE sequences, using the above-described methods. For instance the observation “Sartorius” included respectively one averaged value of FF and wT2. The images obtained by the 8th echo of the MESE sequence (T2 weighted images with TE = 88 ms) were extracted and considered as the conventional (non-quantitative) images of the study. We used the software LifeX (Nioche et al. [2018](#)) to compute the texture analysis on the T2 weighted images, using

the same ROIs previously drawn on the MESE images. Voxel values were normalized and then quantized to 64 Gy levels. All possible features provided by the software were extracted, including first order features statistics based on histogram and shape, and second orders statistics including features derived from the Gray Level Zone Length Matrix (GLZLM), Gray Level Run Length Matrix (GLRLM), Neighborhood Gray-Level Different Matrix (NGLDM) and Gray Level Co-occurrence Matrix (GLCM), for a total of 47 features. Similarly to the process for FF and wT2, ROIs from all 5 slices and both side of the same muscle were merged in order to obtain 12 observations, each made of 47 texture features, per examination. Then texture features, wT2 and FF of each observation were integrated in a unique database. FF values were already normalized whereas wT2 values were scaled ranging from 0 to 1 in order to apply the algorithms described in the following section.

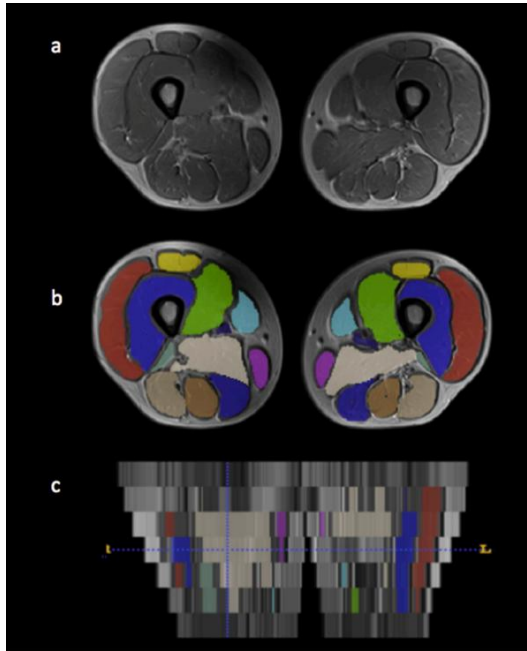


Figure I.1: Illustration of the ROI drawing process. A typical axial T2 weighted image (TE=88 ms) extracted from the MESE sequence is shown (a). One operator manually drew ROIs of each muscle of the thigh (b). 12 muscle ROIs per side per each of the 5 central slices acquired were drawn, for a total of 120 ROIs. For the analysis, ROIs of the same muscle from both sides and from of all slices were merged for a total of 12 observations (each shown with a different color) per examination (b,c).

I.3 Machine Learning and statistical assessment

We tested a set of parametric models including linear (T. Hastie, Tibshirani, and Friedman [2009]), ridge (Hoerl and Kennard [1970]), lasso regression (Tibshirani [1996]) and GAMs (T.J. Hastie [2017]) and nonparametric models including kNN (Cover and Hart [1967]), SVM (Drucker et al. [1997]), tree (Breiman et al. [2017]) and RF (Breiman [2001]) (Python). All observations were considered independent to maximize the number of samples for training the models. To assess the potential effect of correlation between observations from the same patients, we also implemented a mixed effect model where the different subjects were considered as random effects.

Performances of the models were estimated with the indicators mean square error (MSE) and mean absolute error (MAE). The MSE gives information on the mean quadratic discrepancy between the target values y_i and the predicted values \hat{y}_i :

$$MSE = \frac{\sum_i^N (y_i - \hat{y}_i)^2}{N} \quad (\text{I.1})$$

The MAE gives information on the mean of the absolute values of discrepancy between the target values y_i and the predicted values \hat{y}_i :

$$MAE = \frac{\sum_i^N |y_i - \hat{y}_i|}{N} \quad (\text{I.2})$$

To achieve a more realistic assessment of the performance we used cross-validation, a resampling approach in which each model is fitted multiple times on different subsets of the training data. In more detail, for a preliminary estimation of the model hyperparameters, a grid search was used and the entire data set was divided in training and test sets. The training set included the randomly selected 80 % of the data set and the test set the remaining 20 %. Then, for model assessment, the k-folds cross-validation with $k = 5$ was used. This approach involves randomly dividing the entire data set into 5 folds of approximately equal size, using one fold as test set and the remaining four as training sets. The performance indicators are calculated on the test set five times, each time changing the test set fold. We reported means and standard deviation of the performance indicators for each model.

I.4 Results

The final dataset consisted of 384 observations, each with 2 target variables and 47 texture features (covariates) related to 32 MR examinations from 14 patients. The target variables FF values ranged from 0.027 to 0.899 (2.7 to 89.9 %) and wT2 from 26.40 to 78.14 ms.

Three of the original 47 covariates (HISTOEntropylog10, SHAPEVolumevx, GLCMEntropylog10) that had strong correlation with the others, established

on the basis of p-value, were not included in the analysis to avoid collinearity issues.

Table I.1 reports means of MSE and MAE related to FF prediction for each model implemented.

As a result, the prediction performances were good for all models in terms of MSE and MAE and the values were stable (low values of standard deviation). RF was the model with minimum predictive errors (mean value MSE = 0.023, MAE = 0.105), closely followed by KNN (MSE = 0.024) and SVM (MSE = 0.026). We can thus conclude that in the best case (RF) the algorithm predicted the expected FF value with a mean error of approximately +/-11 percentage points (pp), and in the worst case (Trees) of +/-13pp.

Table I.2 reports means of MSE and MAE related to water T2 for each model implemented. The prediction performances were good for all models in terms of average MSE and MAE and in terms of stability, but in this case the kNN gave an outperformance result (MSE = 0.010, MAE 0.068,) followed by RF (MSE = 0.022) and Ridge and Trees (both with MSE = 0.023). Thus the algorithms could predict wT2 with an error ranging from +/- 7pp to +/- 12pp, equivalent to a minimum of 3.50 ms (kNN) to a maximum of 5.94 ms (Linear regression).

The performance of the mixed effect model was similar to the other models (for FF MSE = 0.025 and for wT2 MSE = 0.022).

Model	MSE	MAE
Linear regression	0.029 (0.008)	0.122 (0.015)
Ridge regression	0.028 (0.008)	0.127 (0.018)
Lasso regression	0.030 (0.010)	0.133 (0.021)
GAM	0.028 (0.007)	0.122 (0.013)
Regression Tree	0.033 (0.008)	0.125 (0.013)
Random Forest	0.023 (0.008)	0.105 (0.018)
kNN	0.024 (0.008)	0.110 (0.020)
SVM	0.026 (0.008)	0.114 (0.016)
Mixed effect model	0.025 (0.005)	0.118 (0.009)

Table I.1: Mean squared errors and absolute mean errors for the prediction of Fat Fraction (standard deviation (SD) in round brackets)

Model	MSE	MAE	MAE in T2 scale (ms)
Linear regression	0.025 (0.008)	0.115 (0.016)	5.943 (0.831)
Ridge regression	0.023 (0.009)	0.105 (0.017)	5.450 (0.882)
Lasso regression	0.024 (0.009)	0.108 (0.015)	5.580 (0.755)
GAM	0.025 (0.008)	0.113 (0.018)	5.865 (0.909)
Regression Tree	0.023 (0.007)	0.098 (0.015)	5.048 (0.0762)
Random Forest	0.022 (0.007)	0.098 (0.013)	5.089 (0.692)
kNN	0.010 (0.003)	0.068 (0.008)	3.501 (0.438)
SVM	0.026 (0.009)	0.099 (0.016)	5.134 (0.810)
Mixed effect model	0.026 (0.009)	0.109 (0.017)	5.664 (0.810)

Table I.2: Mean squared errors and absolute mean errors for the prediction of Water T2 (standard deviation (SD) in round brackets). MAE in T2 scale column reports the MAE rescaled to physical units, milliseconds(ms).

I.5 Discussion

In this study, a set of machine learning models are proposed to predict wT2 and FF of thigh muscles using texture analysis of conventional MRI, starting from a dataset of MR examinations from patients affected with FSHD. To the authors' knowledge, this is the first attempt to derive qMRI parameters from texture analysis and our promising results should be considered a proof of principle for further improvements in the future.

There is a growing need to have muscle qMRI parameters accessible and easily obtainable in most neuromuscular centers for assessing disease progression or response to new therapies in rare muscle disorders (Fatehi et al. 2016). Studies showed that qMRI parameters such as wT2 and FF are strongly correlated to the clinical outcome of patients affected with FSHD (Mul et al. 2017). There is evidence that wT2 and FF change over time as disease progresses (Andersen et al. 2017; Ferguson et al. 2018) and that FF can be responsive to the effects of treatments (Janssen et al. 2016). However, having accurate qMRI results is technically challenging and even though commercial and open source qMRI packages are available, further modifications or tuning are often needed to avoid drawbacks. For instance, post-processing correction of stimulated echo artifacts is mandatory for robust measures of wT2 maps obtained with MESE sequences

(Marty et al. [2016](#)). Likewise, 6-point MEGE sequences FF maps are superior to the commonly used 2- or 3-point Dixon techniques used for FF maps. However, 6-point MEGE sequences are not consistently available across different scanning platforms as of now.

Texture analysis and machine learning algorithms can predict clinically relevant outcomes starting from non-quantitative imaging. Most studies used texture analysis to classify discrete outcomes, for instance atrophic versus normal muscles ex vivo (Mahmoud-Ghoneim et al. [2006](#)) and in vivo (Herlidou et al. [1999](#)), or to distinguish different types of myopathies (Burlina et al. [2017](#)). In our study we used machine learning models, more specifically regression models, to predict continuous outcomes such as muscle qMRI parameters FF and wT2.

Our results are encouraging. We observed a minimum MAE of 11pp in FF, which is enough to automatically score muscles with a clinical 5-point scale (Guggenberger et al. [2013](#); Mercuri et al. [2002](#)) allowing also a more precise grading of intermediate levels of FF. In fact, 5-point scales have extreme values consisting in normal (0) or completely fatty substituted (4) muscles, and three intermediate scores consisting in mild, moderate and severe fat substitution. For wT2 the results were even better, with errors ranging from 3.50 ms to 5.94 ms. Since we have no previous examples of such similar analysis in the literature, we can speculate that the better performance for wT2 might reflect a more homogeneous increase of signal overall the muscle, possibly related to textural features sensitive to signal intensity. FF, instead, corresponds to a pattern more related to the morphology, with well-defined strands of fat substituting the muscles from the epimysium. The application of deep learning methods would likely further increase the performance of FF prediction and will be the target of future studies.

We kept almost all features in the analysis, removing only three that were highly correlated with one another. To reduce a potential cause of over-fitting we opted for implementing regularization instead of an initial features selection. In fact, L1 regularization included in the lasso regression, favoring a sparse solution, implicitly implements feature selections. Since there were no relevant differences

in performances between regularized (ridge and lasso) and unregularized (linear) models, we performed the other models (in particular non parametric) while keeping all 44 features as described in the results section. Nonparametric models worked better in both analyses, suggesting a complex and nonlinear relationship between predictors and target variables.

This study has some limitations. The first is related to the relative homogeneity of the training dataset. To expand the applicability of our results, algorithms should be trained with a mixed and larger database encompassing more patients with other muscular diseases, and including normal subjects. Also, they should include examinations from lower field MRI scanners and different vendors. Another limitation is the presence of multiple examinations from the same patients at different time points and different muscles associated to the same patient. However, the mixed effect model did not demonstrate clear differences in performance with respect to the analyses where observations were considered uncorrelated. We applied texture analysis to T2 weighted images without fat-suppression, extracted from the MESE sequence, but T1 weighted and STIR are usually preferred in diagnostic protocols. In this study, as a proof of concept, we chose the sequence where both signals from wT2 and fat were present in order to maximize the chances to prove the feasibility of our method. However, future studies should investigate other sequences with different parameters (TR, TE, slice thickness etc.) including STIR and T1w sequences. We deliberately considered “observations” from the average of both left and right. This was a technical limitation related to the necessity of having a minimum amount of voxels for the texture analysis. In facts, some ROIs were too small and not all muscles were represented in all slices. Higher resolution images would have led to twice the number of observations, at least one per muscle per side.

Future studies may be conducted using deep learning methods that would remove the necessity of texture analysis. These methods, commonly used for muscle segmentation, provide faster analysis of qMRI sequences (Weber et al. [2019](#)) and have been used for classifying different subtypes of muscular

dystrophies (Cai et al. 2019). However, such techniques typically need much larger datasets to be properly trained. One solution could be the use of data augmentation techniques, which artificially increase the training dataset.

In conclusion, we demonstrated the feasibility of predicting the qMRI parameters FF and wT2 using texture analysis and machine learning methods, starting from conventional T2 weighted images. Our encouraging results may extend the implementation of qMRI to all centers dealing with neuromuscular diseases that use standard sequences. Training data is critical and future studies with larger and mixed cohorts are warranted to improve the performance of these methods.

I.6 Appendix A. Supplementary data

Supplementary material related to this article can be found, in the online version, at doi: <https://doi.org/10.1016/j.ejrad.2020.1094>

Appendix B. Comparison of ML performance obtained with k-folds cross validation and with Leave-one-patient-out cross validation schemes

In Paper I, a k-fold cross validation has been implemented on all observations by assuming independence among the observations from the same patient. By implementing the leave-one-patient-out cross validation scheme, the biomarker prediction accuracy of ML algorithms are reported in Table I.3 and I.4

Model	MSE	MAE
Linear regression	0,028 (0,066)	0,120 (0,117)
Ridge regression	0,028 (0,042)	0,125 (0,107)
Lasso regression	0,029 (0,044)	0,132 (0,107)
GAM	0,027 (0,060)	0,119 (0,115)
Regression Tree	0,028 (0,066)	0,116 (0,123)
Random Forest	0,023 (0,047)	0,104 (0,108)
kNN	0,025 (0,047)	0,112 (0,110)
SVM	0,025 (0,048)	0,112 (0,114)
Mixed effect model	0,024 (0,059)	0,114 (0,107)

Table I.3: Mean squared errors and absolute mean errors for the prediction of FF (standard deviation (SD) in round brackets).

Model	MSE	MAE	MAE in T2 scale (ms)
Linear regression	0,025 (0,048)	0,113 (0,112)	5,864 (5,818)
Ridge regression	0,023 (0,046)	0,106 (0,110)	5,471 (5,701)
Lasso regression	0,024 (0,048)	0,108 (0,111)	5,588 (5,717)
GAM	0,026 (0,048)	0,113 (0,114)	5,843 (5,874)
Regression Tree	0,030 (0,067)	0,109 (0,134)	5,635 (6,908)
Random Forest	0,022 (0,045)	0,099 (0,110)	5,112 (5,669)
kNN	0,009 (0,021)	0,066 (0,071)	3,401 (3,694)
SVM	0,027 (0,063)	0,101 (0,129)	5,244 (6,665)
Mixed effect model	0,022 (0,041)	0,108 (0,102)	5,611 (5,301)

Table I.4: Mean squared errors and absolute mean errors for the prediction of wT2 (standard deviation (SD) in round brackets). The column "MAE in T2 scale" reports the MAE rescaled to physical units, milliseconds(ms).

The order of magnitude and the value of MAE and MSE associated with the ML algorithms and resulting from leave-one-patient-out (LOO) is similar to that obtained with the k-folds cross validation scheme with $k=5$ (k-folds). A comparison between MAE (MSE) associated with LOO and k-folds scheme is reported in Figure(I.2)(Figure(I.3)).

The standard deviation (SD) associated to ML algorithms and obtained with the LOO validation scheme, however, is larger than that obtained with the k-folds scheme implemented in Part 1 of Paper I. This may be traced back to the fact that LOO scheme, even if it gives approximately unbiased estimation of the test error, tends to have higher variance than k-folds cross validation as reported in James et al. [2013]. Therefore, in our case k-folds cross validation provides a

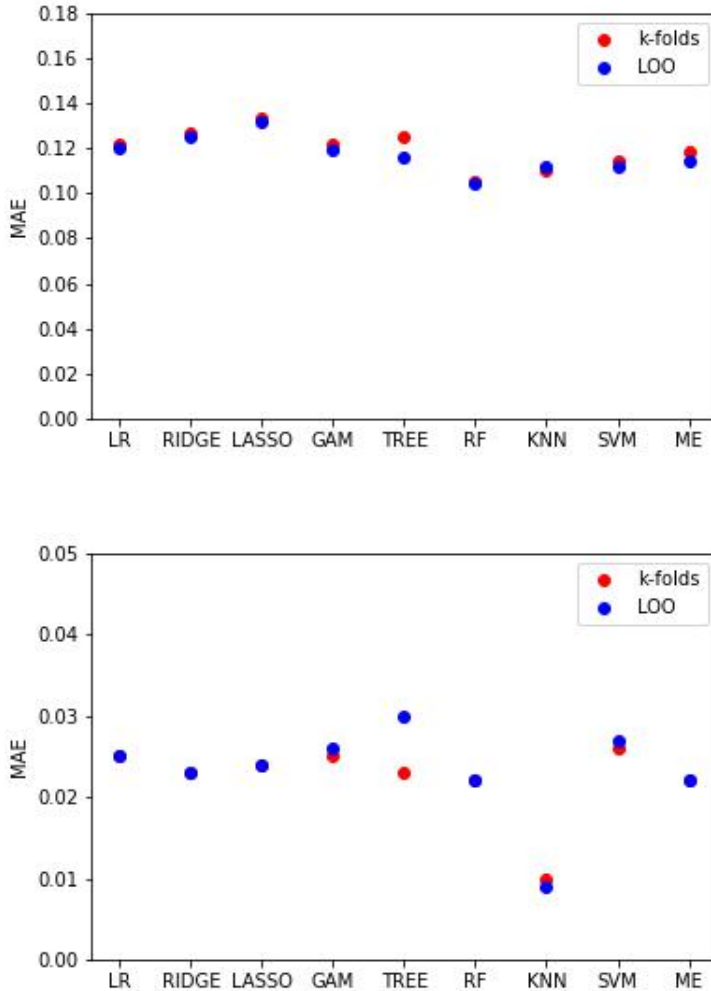


Figure I.2: Comparison of Fat Fraction MAE (top) and water T2 MAE (bottom) obtained with LOO cross validation and k-folds cross validation. On the x-axis are reported the implemented ML algorithms listed in Table I.3 and I.4

good bias-variance trade-off. In addition, LOO cross validation scheme is more computationally expensive with respect to k-folds cross validation, since LOO corresponds to $k=n$ (number of observations) cross validation scheme.

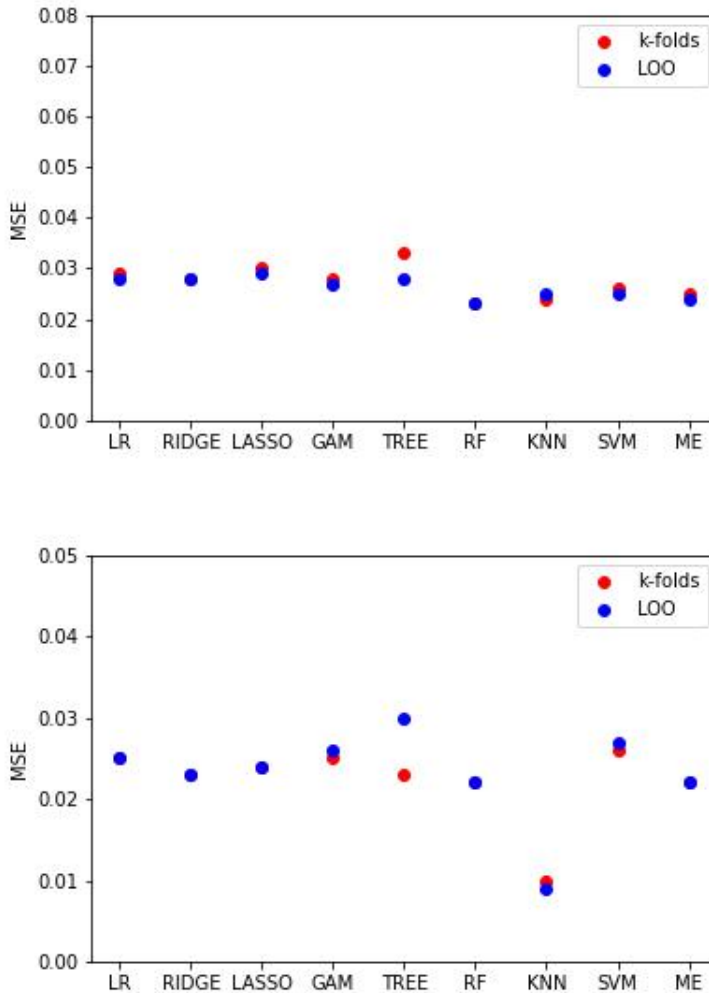


Figure I.3: Comparison of Fat Fraction MSE (top) and water T2 MSE (bottom) obtained with LOO cross validation and k-folds cross validation. On the x-axis are reported the implemented ML algorithms listed in Table I.3 and I.4

References

Andersen, G. et al. (2017). “MRI as outcome measure in facioscapulohumeral muscular dystrophy: 1-year follow-up of 45 patients”. In: *J. Neurol.*

Breiman, L. et al. (2017). *Classification and regression trees*. Routledge.

- Breiman, L. (2001). “Random Forest”. In: *Machine Learning* vol. 45, pp. 5–32.
- Burlina, P. et al. (2017). “Automated diagnosis of myositis from muscle ultrasound: exploring the use of machine learning and deep learning methods”. In: *PLoS One*.
- Cai, J. et al. (2019). “Texture analysis for muscular dystrophy classification in MRI with improved class activation mapping”. In: *Pattern Recognit.*
- Chardon, J.W. et al. (2019). “MYO-MRI diagnostic protocols in genetic myopathie”. In: *Neuromuscular Disord.*
- Cover, T. and Hart, P. (1967). “Nearest neighbor pattern classification”. In: *IEEE transactions on information theory* vol. 13 (1), pp. 21–27.
- Drucker, H. et al. (1997). “Support Vector regression machines”. In: *Adv. Neural Inf. Process. Syst.*
- Emery, A.E.H. (1991). “Population frequencies of inherited neuromuscular diseases-A world survey”. In: *Neuromuscular Disorders*.
- Fatehi, F. et al. (2016). “Muscle MRI of facioscapulohumeral dystrophy (FSHD): A growing demand and a promising approach”. In: *Revue Neurologique* vol. 172, no. 10, pp. 566–571.
- Ferguson, M.R. et al. (2018). “MRI change metrics of facioscapulohumeral muscular dystrophy: stir and T1”. In: *Muscle and Nerve*.
- Guggenberger, R. et al. (2013). “Diffusion tensor imaging of the median nerve at 3.0 T using different MR scanners: agreement of FA and ADC measurements”. In: *European Journal of Radiology* vol. 82.
- Haralick, R.M., Dinstein, I., and Shanmugam, K. (1973). “Textural features for image classification”. In: *IEEE Trans. Syst. Man Cybern.*
- Hastie, T., Tibshirani, R., and Friedman, J. (2009). *Elements of Statistical Learning*,
- Hastie, T.J. (2017). “Generalized additive models.” In: *Stat. Model. S*.
- Herlidou, S. et al. (1999). “Comparison of automated and visual texture analysis in MRI: characterization of normal and diseased skeletal muscle”. In: *Magn. Reson. Imaging*.

- Hoerl, A. E. and Kennard, R. W. (1970). “Ridge regression: Biased estimation for nonorthogonal problems”. In: *Technometrics* vol. 12(1), pp. 55–67.
- James, Gareth et al. (2013). *An introduction to statistical learning*. Vol. 112. Springer.
- Janssen, Barbara et al. (2016). “Quantitative MRI reveals decelerated fatty infiltration in muscles of active FSHD patients”. In: *Neurology* vol. 86, no. 18, pp. 1700–1707.
- Mahmoud-Ghoneim, D. et al. (2006). “Texture analysis of magnetic resonance images of rat muscles during atrophy and regeneration”. In: *Magn. Reson. Imaging*.
- Marty, B. et al. (2016). “Simultaneous muscle water T2 and fat fraction mapping using transverse relaxometry with stimulated echo compensation”. In: *NMR Biomed.*
- Mercuri, E. et al. (2002). “A short protocol for muscle MRI in children with muscular dystrophies”. In: *European Journal of Paediatric Neurology*.
- Monforte, M. et al. (2019). “Tracking muscle wasting and disease activity in facioscapulohumeral muscular dystrophy by qualitative longitudinal imaging.” In: *J. Cachexia. Sarcopenia Muscle*.
- Mul, K. et al. (2017). “Adding quantitative muscle MRI to the FSHD clinical trial toolbox”. In: *Neurology* vol. 89, no. 20, pp. 2057–2065.
- Nioche, C. et al. (2018). “Lifex: a freeware for radiomic feature calculation in multimodality imaging to accelerate advances in the characterization of tumor heterogeneity”. In: *Cancer Res.*
- Paoletti, M et al. (2019). “Advances in Quantitative Imaging of Genetic and Acquired Myopathies: Clinical Applications and Perspectives”. In: *Frontiers in Neurology* vol. 10.
- Strijkers, G.J. et al. (2019). “Exploration of new contrasts, targets, and MR imaging and spectroscopy techniques for neuromuscular disease-A workshop report of working group 3 of the biomedicine and molecular biosciences COST action BM1304 MYO.” In: *Journal of neuromuscular diseases*.

- Tasca, G. et al. (2016). “Magnetic resonance imaging in a large cohort of facioscapulohumeral muscular dystrophy patients: pattern refinement and implications for clinical trials.” In: *Annals of Neurology*.
- Tibshirani, R. (1996). “Regression shrinkage and selection via the lasso”. In: *Journal of the Royal Statistical Society: Series B (Methodological)* vol. 58(1), pp. 267–288.
- Wattjes, M.P., Kley, R.A., and Fischer, D. (2010). “Neuromuscular imaging in inherited muscle diseases”. In: *European Radiology*.
- Weber, K.A. et al. (2019). “Deep learning convolutional neural networks for the automatic quantification of muscle fat infiltration following whiplash injury”. In: *Sci. Rep.*
- Weigel, M. (2015). “Extended phase graphs: dephasing, RF pulses, and echoes - pure and simple.” In: *Magn Reson Imaging*.
- Welch, E.B. et al. (2013). “Optimization of Fat-Water Separation Algorithm Selection and Options Using Image-Based Metrics with Validation by ISMRM Fat-Water Challenge Datasets”. In: *Proceedings of the 21st Annual Meeting of the International Society for Magnetic Resonance in Medicine, Salt Lake City, Utah* vol. 2413.

Paper II

Texture analysis and machine learning applied to STIR sequence for prediction of quantitative parameters in facioscapulohumeral disease

Giulia Colelli^{1,2,3,*}, Leonardo Barzagli^{1,2}, Matteo Paoletti², Xeni Deligianni^{4,5}, Francesco Santini^{4,5}, Mauro Monforte⁶, Giorgio Tasca⁶, Enzo Ricci⁶, Antonietta Mira^{7,8}, Silvia Figini^{9,3,11}, Anna Pichiecchio^{10,2}

Submitted to Frontiers in Neurology, November 2022

Abstract

-
- ¹ Department of Mathematics, University of Pavia, Pavia, Italy
² Advanced imaging and radiomics center, Neuroradiology Department, IRCCS Mondino Foundation, Pavia, Italy
³ INFN - National Institute of Nuclear Physics, Pavia, Italy
⁴ Radiology, Division of Radiological Physics, University Hospital of Basel, Basel, Switzerland
⁵ Basel Muscle MRI, Department of Biomedical Engineering, University of Basel, Basel, Switzerland
⁶ UOC di Neurologia, Fondazione Policlinico Universitario A. Gemelli IRCCS, Roma, Italy
⁷ University of Svizzera Italiana, Lugano, Switzerland
⁸ University of Insubria Varese, Italy
⁹ University of Pavia, Department of Social and Political Science, Pavia, Italy
¹⁰ Department of Brain and Behavioral Sciences, University of Pavia, Pavia, Italy
¹¹ BioData Center, IRCCS Mondino Foundation, Pavia, Italy

Purpose: Quantitative Muscle MRI (qMRI) is a valuable and non-invasive tool to assess disease involvement and progression in neuromuscular disorders being able to detect even subtle changes in muscle pathology. qMRI sequences are, however, not commonly available in most of the clinical centers. The aim of this study is to evaluate the feasibility of using a conventional short-tau inversion recovery (STIR) sequence combined with different radiomics and machine learning workflows to predict fat fraction (FF) and water T2 (wT2) in skeletal muscle.

Methods: Twenty-five patients with facioscapulohumeral muscular dystrophy (FSHD) were scanned at calf level using conventional STIR sequence and qMRI techniques. We applied and compared three different radiomics workflows (WF1, WF2, WF3), combined with seven Machine Learning regression algorithms (linear, ridge and lasso regression, tree, random forest, k-nearest neighbor and support vector machine), on conventional STIR images to predict FF and wT2 for six calf muscles.

Results: The combination of WF3 and K-nearest neighbor resulted to be the best predictor model of qMRI parameters with a mean absolute error about $\pm 5pp$ for FF and $\pm 1.8ms$ for wT2.

Conclusion: This pilot study demonstrated the possibility to predict qMRI parameters in a cohort of FSHD subjects starting from conventional STIR sequence.

Keywords: Radiomics, Machine Learning, Muscle MRI, STIR, FSHD

II.1 Introduction

Muscle Magnetic Resonance Imaging (mMRI) has been increasingly used over the last years as a powerful diagnostic tool to evaluate disease involvement and progression in several neuromuscular disorders (Carlier et al. [2016](#); Díaz-Manera et al. [2015](#); Paoletti et al. [2019](#)). mMRI is able to demonstrate selective patterns of damage distribution both in terms of fat replacement and muscular edema (Costa, Di Primio, and Schweitzer [2012](#); Hollingsworth [2014](#)). Facioscapulohumeral muscular dystrophy (FSHD) is a genetic muscle disorders that causes a slowly progressive and asymmetric weakness of the facioscapulohumeral, abdominal, paraspinal, and lower leg muscles (Andersen et al. [2017](#); J. Dahlqvist et al. [2014](#); Tawil, Kissel, et al. [2015](#); Tawil, Maarel, and Tapscott [2014](#)) both in pediatric and adult patients.

mMRI of FSHD has relied on acquisition of conventional sequences such as T1-weighted (T1w) and short-tau inversion recovery (STIR) sequences that are able to foster the qualitative detection of anatomical changes in muscles size or shape, particularly related to fat replacement and muscle edema (or edema-like) (E. Mercuri et al. [2002](#); Reimers et al. [1994](#)), revealing a widespread involvement both in upper girdle and lower limbs (Fatehi et al. [2016](#); Gerevini et al. [2016](#)).

The use of mMRI enabled to propose a peculiar model for FSHD disease evolution, highlighting how patients undergo a muscle-selective involvement with an early hyperintense signal on STIR sequence related to edema/inflammation, followed by fatty replacement of single muscles, particularly evident on T1w images (M. Monforte et al. [2019](#)). As per other neuromuscular diseases, semi-quantitative visual scales have been applied to support and improve the evaluation of morphological changes in muscles, *e.g.*, Mercuri and Fischer scales (Fischer et al. [2008](#); Eugenio Mercuri et al. [2007](#)). The recent development and implementation of quantitative MRI (qMRI) in the field of neuromuscular diseases allowed to go beyond the conventional and semi-quantitative approaches, being able to assess quantitative parameters (*e.g.* the percentage of fat replace-

ment in the muscle, the so called fat fraction, FF), improving the non-invasive applicability of muscle imaging in the diagnostic process and follow-up of muscle disorders (Janssen et al. [2016](#)). Neither the clinical outcomes nor the conventional muscle MRI techniques, in fact, are deemed to be sensitive enough to track muscle changes in slowly progressing diseases (Carlier et al. [2016](#)).

MRI is considered a valuable tool to monitor even fine changes in neuromuscular disease evaluation and longitudinal progression over time because it delivers quantitative information such as muscles FF and the muscle water T2 relaxation time related to intramuscular edema (wT2) (J. R. Dahlqvist et al. [2020](#)). Dixon imaging and Multi-Echo T2 spin-echo sequences are the most commonly used qMRI methods to compute FF and wT2 (Carlier et al. [2016](#)). Up-to-date qMRI methods require custom-tailored sequences provided by vendors on the MRI scanner resulting in high-cost implementations, so qMRI is still unavailable in many clinical centers. Recently, radiomics proved to be a powerful tool to extract quantitative information from MRI images, becoming a new asset in the diagnostic field (Timmeren et al. [2020](#)). It can identify the main patterns of a disease through the mathematical extraction of pixel intensity and spatial interrelationship distributions. Radiomics quantifies textural information that, once dimensionally reduced (Abdi and Williams [2010](#); Glielmo et al. [2022](#)), can be combined with machine learning (ML) algorithms to predict neuromuscular quantitative biomarkers FF and wT2 with a good predictive power (Felisaz et al. [2021](#)).

However, it is still unclear whether and how radiomics could be applied on conventional STIR images and combined with ML algorithms to predict FF and wT2. Moreover, it remains unexplored whether the predictive power of ML algorithms on conventional STIR images could be improved through the definition of new radiomic features as an alternative to the ones provided by commercial radiomic feature extraction software (Nioche, Orhac, and Buvat [2020](#)).

STIR sequence is most likely available in all MRI centers and it has a very competitive acquisition time compared to qMRI sequences. In this study we aim

to investigate whether different radiomic and machine learning algorithms may be applied to conventional STIR sequence to predict quantitative parameters in skeletal muscle.

II.2 Materials and Methods

Twenty-five FSHD patients (10 females, age range: 19-60y) and six healthy volunteers (HCs) (5 females, age range: 47-63y) were scanned on a 3T MRI scanner (Magnetom Skyra, Siemens Healthcare, Erlangen, Germany) using integrated spine and body surface coils. Acquisition volume was centered on the calf with the last acquired slice located at 6cm proximally from the upper limit of the patella. The MRI protocol included 3D 6-point multi-echo gradient-echo (MEGE) [52 slices, slice thickness =5.0mm, distance factor =20 %, resolution = $1 \times 1 \times 5 \text{mm}^3$, TR/ TE =35ms/1.7-9.2 ms, scan time = 15 min], multi-echo spin echo (MESE) [7 slices, TH=10mm, DF=300 %, resolution = $1.2 \times 1.2 \times 10 \text{mm}^3$, TR/TE = 4100ms/10.9-185.3ms, 17 echoes, scan time = 5.13min] and 2D STIR sequences [50 slices, TH=5.0mm, DF=20 %, resolution = $1 \times 1 \times 5 \text{mm}^3$, TR/TE =4200/82ms ,TI=230 ms, scan time = 3.40min]. Pre-processing steps have been performed on STIR images in order to ensure feature extraction on an inter-patients harmonized grayscale values. In particular, all images were pre-processed by 3DSlicer (Fedorov et al. [2012](#)) N4 Bias Field Correction to correct low frequency intensity non-uniformity in MRI images, and 3DSlicer Histogram Matching to normalize grayscale MRI images.

From the first echo images of MEGE, one mid-calf slice of each FSHD patient was chosen to be automatically segmented (Agosti et al. [2021](#)) into six regions of interest (ROIs) for each calf muscle, *i.e.*, Soleus (S), Medial and Lateral Gastrocnemius (MG, LG), Anterior Tibialis (TA), Extensor Digitorum Longus (ELD), Peroneus Longus (Pe). The ROIs were co-registered to the mid-calf MESE and STIR slice using FSL software (Woolrich et al. [2009](#)) and then manually corrected by a single trained operator with 3 years of experience.

For each subject, radiomic feature extraction and ML predictions were

performed on the mid-calf slice of STIR image because it gives a representation of all calf muscles with a cross sectional area (CSA) wide enough to ensure the extraction of a robust pixel intensity distribution (Arpan et al. [2013](#)). In particular, feature extraction was performed averaging the left and right side of each muscle. Finally, ground truth FF and wT2 values, which the ML predictions have been compared to, were calculated by Fatty Riot algorithm (Smith et al. [2013](#)) and by EPG signal simulation (F. Santini et al. [2021](#); Weigel [2015](#)) from mid-calf MEGE and MESE slice, respectively.

II.2.1 dataset, dimensionality reduction and machine learning algorithms

We compare the performance in predicting calf muscle-wise FF and wT2 values introducing three different workflows. In particular, inspired by Felisaz et al. [2021](#) work, the first workflow predicts FF and wT2 combining radiomics with LIFEx software (Nioche, Orhac, and Buvat [2020](#)), principal component analysis (PCA) (Jolliffe [2002](#)) and ML regression models. The second method uses the same feature extraction and ML models of the previous method but explores the use of a new dimensionality reduction technique (Glielmo et al. [2022](#)) as an alternative to PCA to verify a possible improvement in the prediction of neuromuscular quantitative parameters. The third method relies neither on Lifex features nor on any dimensionality reduction technique. In particular, two STIR-based features are defined as markers of muscle fat percentage and muscle inflammation. These two features are used as the only predictors in ML models to test whether there is an improvement in the predictive performance of FF and wT2.

II.2.1.1 workflow 1

Feature extraction was performed using the IBSI standard-compliant LIFEx software v.7.1.0 with the aim to extract shape related features, taking into account for size and geometric properties, to first-order statistic features,

concerning voxel intensity distributions and to second-order statistic features highlighting voxel spatial relationship. In particular, a 2D extraction was performed on each ROI corresponding to the six calf muscles (left and right side were averaged). Therefore, we obtained six datasets associated to each calf muscle. On each dataset principal component analysis (PCA) (Jolliffe [2002](#)) dimensional reduction was performed in order to obtain lower-dimensional data while preserving as much of the data variation as possible. Six principal components, which in our case retain about 90% of the explained variance, were identified and consequently each data point was projected onto them. For each muscle dataset we implemented the parametric linear (Friedman et al. [2001](#)), ridge (Hoerl and Kennard [1970](#)) and Lasso (Tibshirani [1996](#)) regression and the non-parametric KNN (Cover and Hart [1967](#)), SVM (Drucker et al. [1996](#)), tree (Breiman et al. [2017](#)), and RF (Breiman [2001](#)) algorithms. A k-fold cross validation resampling approach with k=5 was used on the associated PCA dimensionally reduced dataset. This procedure guarantees a more realistic performance evaluation of each machine learning model by fitting the same statistical model several times on randomly obtained subsets of approximately equal size.

II.2.1.2 workflow 2

The starting point was the 2D extraction of texture features from the pre-processed STIR image as described in Sec. [II.2.1.1](#). To reduce the dimensionality of the dataset we have used the concept of information imbalance described in Glielmo et al. [2022](#). More precisely, performing feature selection or dimensionality reduction in our case is the same task of finding the most suitable measure between data points, since explicit features are available. This is because a particular choice of features naturally gives rise to a different distance function computed through the Euclidean norm (Glielmo et al. [2022](#)). Therefore, we designed a feature selection algorithm by selecting the subset of features, which minimizes the information imbalance with respect to the two targets, the

values of the neuromuscular biomarkers FF and wT2, separately. The definition of information imbalance Δ used was its estimation on a dataset with N points (Glielmo et al. 2022):

$$\Delta(A \rightarrow B) \approx 2(r^B | r^A = 1) / N \quad (\text{II.1})$$

where A is the space consisting in the radiomic feature space and B is the space associated to FF or wT2 biomarkers, r^B and r^A represent the rank of each pair of points in the space B and A respectively, calculated according to the distance d_B and d_A , an euclidean norm defined in the relative space. Thus, information imbalance quantify the relative information content of a distance measure with respect to another using the concept of local neighborhoods.

A low value of $\Delta(A \rightarrow B)$ means that the combination of a certain features can predict a specific neuromuscular biomarker. Figure II.1 shows for Soleum the minimum information imbalance $\Delta(A \rightarrow B)$ achievable with a specific subset of radiomic features for the two biomarkers wT2 and FF. For each muscle we optimized the information imbalance respect to target FF and wT2 separately and we selected the subspace of radiomic features corresponding to the associated minimum Δ . The obtained datasets for each muscle and each biomarkers were used as input for machine learning algorithms. As in Sec. II.2.1.1 parametric and non-parametric algorithms were implemented using the resampling k-folds cross validation.

II.2.1.3 workflow 3

We defined two STIR-based radiomic features to be used as an alternative to the conventional textural features of WF1 and WF2. We use these new features as the only covariates in the implementation of ML algorithms to test whether the prediction performance of ML models could be improved over those obtained by the previously described workflows.

Firstly, we applied the same segmentation method of FSHD patients on the pre-processed STIR images of each healthy control (HC). In particular, six contiguous HCs slices of mid-calf region were segmented in order to ensure

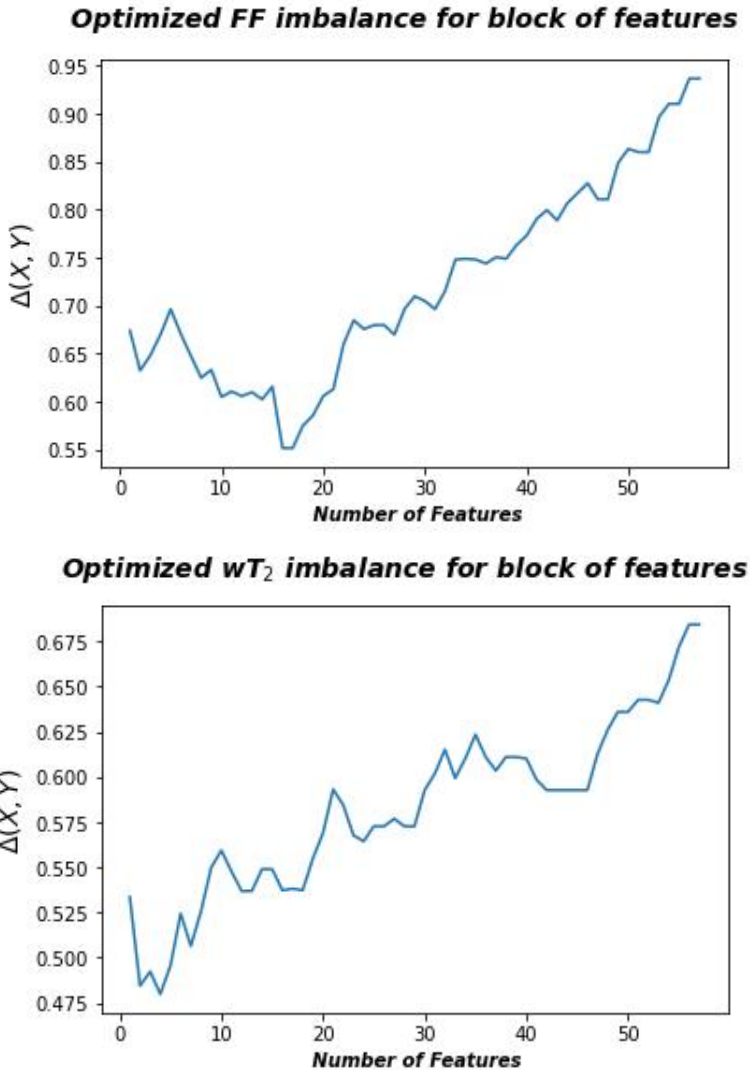


Figure II.1: Optimized information imbalance respect to the target biomarker FF(top) and to the wT₂ (bottom) showed as a function of subsets of radiomic features space A.

a robust pixel statistics of the grayscale intensity distributions. Then, two reference limits, Upper Limit (UL) and Lower Limit (LL), were defined as follow. Inspired by J. R. Dahlqvist et al. [2020](#), UL was defined for each calf muscle through the extraction of pixel-wise histogram of signal intensity distribution

from all slices. The six muscle-wise UL were set at the mean μ of the associated pixels-intensity distribution added to 2 standard deviation (S.D.) σ :

$$UL_i = \mu_i + 2\sigma_i \quad (\text{II.2})$$

with i indexing the six calf muscle.

Due to non-uniform fat suppression of STIR sequence, LL was calculated as a representative value of fat signal intensity. Therefore, subcutaneous fat was manually drawn in HC slices to ensure the extraction of this LL feature. In particular, from subcutaneous fat ROI of all slices the pixel-wise histogram of signal intensity distribution was extracted. Subsequently, the LL was set as the mode of the distribution. In this way, we could calculate a more realistic fat intensity representative value, limiting the contribution of blood vessels present in the subcutaneous fat, which tend to shift the mean value of the associated distribution towards greater value due to the hyperintensity STIR signal of the blood.

Moreover, the obtained LL and muscle-wise UL coefficients were set as the reference limits to quantify, for every FSHD patient, fat infiltration grade (FFG) and muscle edema grade (MEG) by expressing the number of pixels below LL and above UL as a percentage of the total pixels in each calf muscle.

FFG and MEG were then used as covariates in ML models to predict FF and wT2, respectively. Particularly, muscle-wise FFG and MEG values were separately collected into datasets according to calf muscles and neuromuscular biomarker and used as input for machine learning algorithms. As described in Sec. [II.2.1.1](#) we implemented both parametric and non parametric models using the k-folds cross validation as resampling approach. The workflow 3 brought the advantage of testing the prediction accuracy of neuromuscular biomarkers with two features that were easy to compute by means of a stand-alone Python routine, without go through commercial texture softwares and any dimensionality reduction techniques.

II.2.2 ML models performance evaluation

According to the aforementioned workflows, the performance estimation of the models was performed calculating for each muscle and for each machine learning algorithm the mean absolute error (MAE):

$$MAE_j = \frac{\sum_{i=1}^N |y_i - \bar{y}_i|}{N} \quad (\text{II.3})$$

where N is the number of observations, y_i is the target value, \bar{y}_i the predicted value, index j is related to the different calf muscle and index i runs over the observations associated to each muscle. Furthermore, Mean MAE ($M\bar{A}E$) was defined as:

$$M\bar{A}E_j = \frac{\sum_{k=1}^5 MAE_j}{N} \quad (\text{II.4})$$

where the index k runs over the $k=5$ folds.

II.3 Results

In Tables [II.1](#), [II.2](#), [II.3](#) the FF $M\bar{A}E$ was reported for the three used workflows (WF1, WF2 and WF3) calculated for each muscle and from each ML algorithm. Similarly, in Tables [II.4](#), [II.5](#), [II.6](#) the $M\bar{A}E$ was reported for wT2. Boxplots in Fig. [II.2](#) show the FF and wT2 $M\bar{A}E$ distribution per each muscle and workflow (WF 1, 2 and 3). The discrepancy between the ground truth values and ML predicted values is expressed in percentage points (pp) for FF and in milliseconds (ms) for wT2, respectively.

Muscle	Mean absolute discrepancy (MAE)							
	LR	ridge	Lasso	TREE	RF	KNN	SVM	
S	0.155 (0.052)	0.139 (0.047)	0.130 (0.042)	0.147 (0.037)	0.137 (0.035)	0.116 (0.064)	0.102 (0.058)	
MG	0.284 (0.064)	0.283 (0.059)	0.295 (0.054)	0.276 (0.068)	0.278 (0.073)	0.279 (0.066)	0.276 (0.066)	
LG	0.066 (0.074)	0.133 (0.032)	0.139 (0.036)	0.129 (0.027)	0.147 (0.030)	0.137 (0.032)	0.109 (0.034)	
TA	0.225 (0.039)	0.220 (0.039)	0.247 (0.051)	0.239 (0.035)	0.205 (0.013)	0.204 (0.030)	0.210 (0.030)	
ELD	0.225 (0.028)	0.191 (0.021)	0.235 (0.0334)	0.205 (0.018)	0.189 (0.028)	0.082 (0.010)	0.167 (0.028)	
Pe	0.039 (0.02)	0.046 (0.01)	0.043 (0.011)	0.044 (0.017)	0.046 (0.0117)	0.028 (0.011)	0.039 (0.017)	

Table II.1: workflow 1 ([II.2.1.1](#)): Evaluation of ML models predicting performances: mean absolute discrepancy (MAE) between the muscle-wise Fat Fraction gold standard values from Fatty Riot algorithm and the predicted value through ML algorithms. S.D. is reported in round brackets.

Mean absolute discrepancy (MAE)							
Muscle	LR	ridge	Lasso	TREE	RF	KNN	SVM
S	0.171 (0.090)	0.135 (0.050)	0.130 (0.042)	0.128 (0.053)	0.113 (0.063)	0.072 (0.035)	0.096 (0.054)
MG	0.414 (0.180)	0.271 (0.052)	0.296 (0.053)	0.348 (0.042)	0.295 (0.051)	0.098 (0.033)	0.277 (0.050)
LG	1.133 (1.967)	0.255 (0.253)	0.136 (0.038)	0.121 (0.031)	0.134 (0.058)	0.134 (0.032)	0.115 (0.043)
TA	0.225 (0.039)	0.220 (0.039)	0.247 (0.051)	0.239 (0.035)	0.204 (0.013)	0.204 (0.030)	0.210 (0.030)
ELD	0.225 (0.028)	0.191 (0.021)	0.237 (0.033)	0.205 (0.0178)	0.189 (0.028)	0.082 (0.010)	0.167 (0.028)
Pe	0.039 (0.020)	0.046 (0.009)	0.043 (0.011)	0.044 (0.017)	0.046 (0.012)	0.028 (0.011)	0.039 (0.017)

Table II.2: workflow 2 (II.2.1.2): Evaluation of ML models predicting performances: mean absolute discrepancy (MAE) between the muscle-wise Fat Fraction gold standard values from Fatty Riot algorithm and the predicted value through ML algorithms. S.D. is reported in round brackets.

Mean absolute discrepancy (MAE)							
Muscle	LR	ridge	Lasso	TREE	RF	KNN	SVM
S	0.130 (0.028)	0.130 (0.031)	0.130 (0.036)	0.137(0.032)	0.148 (0.043)	0.066 (0.031)	0.105 (0.054)
MG	0.312 (0.041)	0.309 (0.034)	0.297 (0.021)	0.286 (0.064)	0.275 (0.047)	0.052 (0.012)	0.316 (0.054)
LG	0.135 (0.030)	0.135 (0.030)	0.134 (0.030)	0.149 (0.018)	0.171 (0.026)	0.061 (0.012)	0.110 (0.023)
TA	0.277 (0.043)	0.273 (0.037)	0.262 (0.035)	0.242 (0.068)	0.235 (0.078)	0.057 (0.012)	0.194 (0.062)
ELD	0.242 (0.040)	0.242 (0.039)	0.240 (0.035)	0.270 (0.051)	0.211 (0.059)	0.048 (0.019)	0.180 (0.051)
Pe	0.045 (0.019)	0.044 (0.019)	0.044 (0.020)	0.048 (0.021)	0.052 (0.020)	0.034 (0.019)	0.040 (0.024)

Table II.3: workflow 3 (II.2.1.3): Evaluation of ML models predicting performances: mean absolute discrepancy (MAE) between the muscle-wise Fat Fraction gold standard values from Fatty Riot algorithm and the predicted value through ML algorithms. S.D. is reported in round brackets.

Mean absolute discrepancy (MAE)							
Muscle	LR	ridge	Lasso	TREE	RF	KNN	SVM
S	4.21 (0.518)	4.21 (0.550)	3.98 (0.647)	3.33 (1.23)	2.78 (0.680)	3.40 (0.874)	0.324 (0.809)
MG	9.22 (1.90)	9.05 (1.81)	8.80 (1.77)	9.73 (1.68)	9.35 (2.61)	8.72 (2.11)	8.25 (2.61)
LG	6.44 (2.49)	5.71 (1.29)	5.07 (0.387)	5.84 (1.46)	5.71 (1.59)	5.28 (0.730)	4.38 (1.68)
TA	9.28 (2.42)	9.22 (2.38)	9.09 (2.50)	9.34 (3.11)	10.1 (3.48)	9.42 (3.44)	9.22 (2.83)
ELD	9.03 (4.13)	8.83 (3.97)	8.41 (3.59)	7.33 (2.08)	7.83 (3.09)	7.64 (3.05)	6.64 (2.93)
Pe	1.96 (0.472)	1.92 (0.413)	1.83 (0.325)	1.83 (0.384)	1.68 (0.246)	1.81 (0.334)	1.76 (0.197)

Table II.4: workflow 1 (II.2.1.1): Evaluation of ML models predicting performances: mean absolute discrepancy (MAE expressed in ms) between the muscle-wise water T2 gold standard values from EPG signal simulation algorithm and the predicted value through ML algorithms. S.D. is reported in round brackets.

Mean absolute discrepancy (MAE)							
Muscle	LR	ridge	Lasso	TREE	RF	KNN	SVM
S	4.31 (1.12)	3.92 (1.26)	3.85 (1.33)	4.66 (1.07)	3.63 (1.33)	2.36 (0.615)	3.59 (0.874)
MG	10.4 (1.26)	10.4 (1.22)	10.4 (1.18)	8.17 (1.64)	9.05 (2.36)	2.15 (0.337)	8.25 (2.02)
LG	13.2 (4.17)	9.49 (2.28)	4.73 (2.32)	8.08 (2.84)	9.02 (2.45)	6.14 (1.98)	7.90 (2.36)
TA	8.36 (1.07)	7.99 (0.901)	7.70 (0.737)	7.62 (1.19)	7.04 (1.15)	3.28 (1.07)	6.84 (1.23)
ELD	26.2 (47.8)	4.21 (1.43)	5.21 (2.20)	4.21 (1.70)	4.90 (2.01)	2.39 (1.51)	3.67 (2.16)
Pe	2.71 (1.03)	2.24 (0.748)	2.24 (0.817)	2.07 (0.561)	1.97 (0.698)	0.797 (0.384)	1.73 (0.708)

Table II.5: workflow 2 (II.2.1.2): Evaluation of ML models predicting performances: mean absolute discrepancy (MAE expressed in ms) between the muscle-wise water T2 gold standard values from EPG signal simulation algorithm and the predicted value through ML algorithms. S.D. is reported in round brackets.

Muscle	Mean absolute discrepancy (MAE)						
	LR	ridge	Lasso	TREE	RF	KNN	SVM
S	1.55 (0.453)	1.36 (0.453)	1.07 (0.453)	1.26 (1.33)	0.809 (1.17)	1.90 (0.583)	0.647 (0.971)
MG	8.46 (2.19)	8.46 (2.15)	8.46 (2.15)	9.26 (2.06)	10.4 (2.19)	2.06 (0.758)	8.00 (2.40)
LG	4.98 (0.687)	4.98 (0.730)	5.03 (0.687)	5.93 (0.902)	5.80 (1.16)	2.58 (0.988)	4.55 (1.57)
TA	9.91(2.58)	9.91 (2.54)	9.91 (2.50)	9.09 (2.91)	9.38 (2.62)	2.79 (1.07)	8.60 (2.66)
ELD	9.65 (3.47)	9.65 (3.47)	9.68 (3.20)	7.68 (2.01)	7.68 (2.05)	1.43 (0.502)	6.71 (2.35)
Pe	1.76 (0.246)	1.75 (0.236)	1.75 (0.236)	1.81 (0.266)	1.89 (0.295)	0.443 (0.148)	1.70 (0.266)

Table II.6: workflow 3 (II.2.1.3): Evaluation of ML models predicting performances: mean absolute discrepancy (MAE expressed in ms) between the muscle-wise water T2 gold standard values from EPG signal simulation algorithm and the predicted value through ML algorithms. S.D. is reported in round brackets.

<i>CV - parameter</i>	Pearson	Spearman
Vol - FF	-0.19 (0.75)	-0.10 (0.80)
Vol - wT2	0.75 (0.080)	0.71 (0.080)
FF - FF	0.43 (0.46)	0.58 (0.30)
wT2 - wT2	0.65 (0.16)	0.55 (0.25)

Table II.7: Pearson and Spearman correlation coefficients between volume CVs, ground truth CVs and KNN MAE prediction of neuromuscular parameters. P-values are reported in round brackets with a significant level set at $p \leq 0.05$. KNN FF prediction for Pe muscle was not included to evaluate Pearson and Spearman correlations because it resulted to be an outliers of KNN FF MAE distribution.

As inferred from boxplots in Fig. II.2, each workflow resulted in a mean FF and wT2 prediction performance of $\approx \pm 20pp$ and $\approx \pm 6ms$ (averaged values) for the anterior compartment muscles and of $\approx \pm 15pp$ and $\approx \pm 6ms$ for the posterior compartment, respectively. Figure II.3 shows the mean prediction performance, averaged on all calf muscles, for each ML algorithm and workflow. KNN algorithm proved to be the best predictor model when combined with WF3 for FF ($M\bar{A}E \pm 5pp(S.D.1.8pp)$) and for wT2 ($M\bar{A}E \pm 1.8ms(S.D.0.7ms)$). By contrast linear regression (LR) combined with WF2 showed the worst accuracy in estimating FF ($\pm 36pp(S.D.38.2pp)$) and wT2 ($\pm 10.9ms(S.D.9.4)$). To measure the variability of volume and ground truth distributions we also calculated the coefficients of variation (CVs) defined as:

$$CV_i = \frac{\sigma_i}{\mu_i} \quad (II.5)$$

where the index i runs over the muscles, σ_i and μ_i are the associated S.D.

and mean of the distributions, respectively. Thus, CVs for muscle-wise FF and wT2 ground truths quantify the variability range of ground truth values on which the ML models were tested. Figure II.4 reports the CV_i for FF and wT2 for each calf muscle. Similarly, muscle volume CVs account for inter-subject muscle shape variability. Volume CVs are reported in Fig. II.5. The ground truth CVs range from 0.45 to 0.99 for FF and from 0.04 to 0.22 for wT2 whereas volume CVs range from 0.30 to 0.42 (Fig. II.4II.5).

We explored whether KNN MAE prediction shows linear or monotonic dependency on CV values of muscle volume and ground truth parameters using Pearson (ρ_P) and Spearman (ρ_S) correlation coefficients. Table II.7 shows no significant correlation between KNN $M\bar{A}E$ and both CVs of ground truths and volume values. Thus, KNN prediction seemed to be independent from inter-subject muscle shape, *i.e.*, CVs volume, and ground truth variability ranges, *i.e.*, CVs of FF and WT2. Furthermore, the presence of linear and monotonic correlations was tested even between KNN $M\bar{A}E$ and muscle mean volume to examine KNN prediction dependency on different calf size of muscles. For our cohort, the following mean volume values for calf muscles were: S \approx 1743.1mm³, MG \approx 987.5mm³, LG \approx 585.9mm³, TA \approx 458.4mm³, ELD \approx 295.8mm³, Pe \approx 534.6mm³. Pearson and Spearman coefficients did not show any significant correlation neither for $M\bar{A}E$ FF ($\rho_P=0.66$ (0.22)) and $\rho_S=0.52$ (0.36)) nor for $M\bar{A}E$ wT2 ($\rho_P=0.12$ (0.83) and $\rho_S=0.08$ (0.87)). Therefore, KNN prediction seemed to be independent even from calf dimension of muscles.

II.4 Discussion

In this study we explored the possibility to predict fat fraction and water T2 of calf muscles in FSHD subjects starting from a conventional STIR sequence and applying three different workflows, which combine radiomics, dimensionality reduction methods and ML models. To the authors' knowledge, this is the first attempt to predict qMRI parameters from STIR imaging. The three applied workflows resulted in a comparable mean prediction performance about $\pm 20pp$

for FF and about $\pm 6ms$ for wT2 with the exception of LR and KNN models (Fig. II.3). KNN, according to the obtained results, turned out to be the best model predictor both for FF and wT2. More specifically, the algorithm-wise performance highlights the best prediction for the combination of KNN and WF3 for both FF ($\pm 5pp$) and wT2 ($\pm 1.8ms$) (Fig. II.3). The muscle-wise analysis of the prediction performance also demonstrate a KNN mean prediction performance with almost no dependency either on the dimension of muscles and on the inter-subject muscle shape (Figure II.2). We investigate these hypothesis by calculating for each muscle the muscle mean volume and the volume Cvs. Despite the difference both in mean muscle-wise volume values and in volume CVs (Figure II.5), no significant Pearson and Spearman correlation were found with KNN $M\bar{A}E$ that was able to predict wT2 and FF with a mean error of approximately $\pm 1.8ms$ and $\pm 5pp$ respectively.

Furthermore, the combination of a small sample size and high CV of ground truth distributions may have negatively affected the ML training step and consequently compromised prediction performance . However, KNN parameters prediction seemed to have no dependency on CV of ground truth values used for training ML algorithms (Fig. II.2). In contrast to the good predictive power of KNN, we found the least performative model being LR combined with WF2 (Fig. II.3). We surmise that LR + WF 2 might be unable to detect the complex relationship between predictors and target variable as suggested by the wider error bars. The main limit of the current study is related to the suboptimal suppression of fat signal in STIR sequences. Nevertheless, we used this non-uniform fat signal component to identify image fat pixels, which were used to extract conventional radiomic features (WF 1, 2), and to define FFG feature (WF3). Conversely STIR imaging is particularly suitable for muscle edema pattern detection (J. R. Dahlqvist et al. 2020) which may be easily detected by radiomic features.

Moreover, to expand the applicability of the current results, we aim to conduct further studies enrolling larger cohorts of subjects with different neuromuscular dystrophies and also exploring other skeletal muscle districts (*e.g.* paravertebral

muscles).

In conclusion, our study showed that conventional STIR imaging can potentially be used to predict quantitative muscle MRI parameters with good accuracy by applying radiomics combined with ML models. In particular, the KNN algorithm combined with WF3 was the best predictor for both FF and wT2. The proposed radiomic workflows could contribute to a wider application of a relatively common imaging technique as STIR to rapidly estimate quantitative parameters of skeletal muscle, without the need to acquire long and complex advanced qMRI sequences.

References

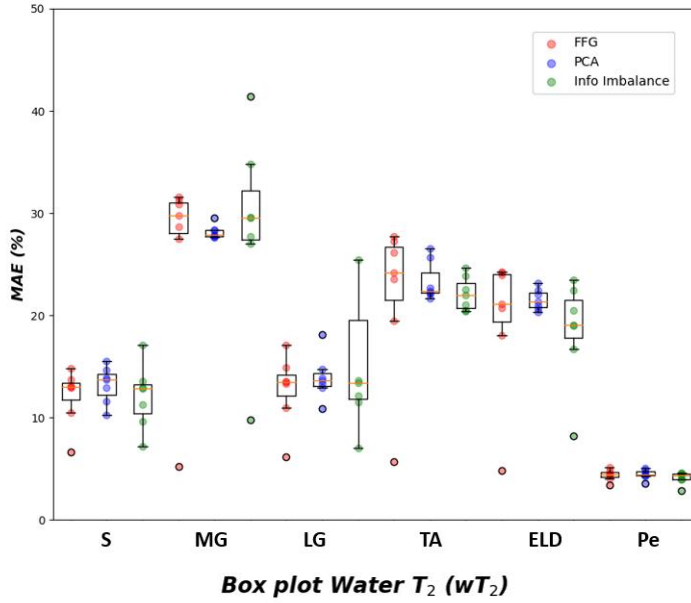
- Abdi, H. and Williams, L. J. (2010). “Principal component analysis”. In: *WIREs Computational Statistics* vol. 2, no. 4, pp. 433–459.
- Agosti, A. et al. (2021). “Deep learning for automatic segmentation of thigh and leg muscles.” In: *Magma (New York, N.Y.)*
- Andersen, G et al. (2017). “MRI as outcome measure in facioscapulohumeral muscular dystrophy: 1-year follow-up of 45 patients.” In: *J Neurol.*
- Arpan, I. et al. (2013). “T2 mapping provides multiple approaches for the characterization of muscle involvement in neuromuscular diseases: a cross-sectional study of lower leg muscles in 5–15-year-old boys with Duchenne muscular dystrophy”. In: *NMR in Biomedicine* vol. 26, no. 3, pp. 320–328.
- Breiman, L. (2001). “Random forests”. In: *Machine learning* vol. 45(1), pp. 5–32.
- Breiman, L. et al. (2017). *Classification and regression trees*. Routledge.
- Carrier, P.G. et al. (2016). “Skeletal Muscle Quantitative Nuclear Magnetic Resonance Imaging and Spectroscopy as an Outcome Measure for Clinical Trials”. In: *J Neuromuscul.*
- Costa, A. F., Di Primio, G. A., and Schweitzer, M. E. (2012). “Magnetic resonance imaging of muscle disease: A pattern-based approach”. In: *Muscle & Nerve* vol. 46, no. 4, pp. 465–481.

- Cover, T. and Hart, P. (1967). “Nearest neighbor pattern classification”. In: *IEEE transactions on information theory* vol. 13 (1), pp. 21–27.
- Dahlqvist, J.R. et al. (2014). “Severe paraspinal muscle involvement in facioscapulohumeral muscular dystrophy”. In: *Neurology*.
- Dahlqvist, Julia R. et al. (2020). “MRI in Neuromuscular Diseases: An Emerging Diagnostic Tool and Biomarker for Prognosis and Efficacy”. In: *Annals of Neurology* vol. 88, no. 4, pp. 669–681.
- Díaz-Manera, J. et al. (2015). “Muscle MRI in muscular dystrophies.” In: *Acta Myologica*, 34(2-3).
- Drucker, H. et al. (1996). “Support vector regression machines”. In: *Advances in neural information processing systems* vol. 9.
- Fatehi, F. et al. (2016). “Muscle MRI of facioscapulohumeral dystrophy (FSHD): A growing demand and a promising approach”. In: *Revue Neurologique* vol. 172, no. 10, pp. 566–571.
- Fedorov, A. et al. (2012). “3D Slicer as an Image Computing Platform for the Quantitative Imaging Network.” In: *Magn Reson Imaging* vol. 30(9), pp. 1323–41.
- Felisaz, Paolo Florent et al. (2021). “Texture analysis and machine learning to predict water T2 and fat fraction from non-quantitative MRI of thigh muscles in Facioscapulohumeral muscular dystrophy”. In: *European Journal of Radiology* vol. 134, p. 109460.
- Fischer, D. et al. (2008). “Distinct muscle imaging patterns in myofibrillar myopathies”. In: *Neurology* vol. 71, no. 10, pp. 758–765.
- Friedman, J. et al. (2001). *The elements of statistical learning*. Vol. 1. Springer series in statistics New York.
- Gerevini, S. et al. (2016). “Muscle MRI findings in facioscapulohumeral muscular dystrophy”. In: *European Radiology*.
- Glielmo, Aldo et al. (2022). “Ranking the information content of distance measures”. In: *PNAS Nexus*.
- Hoerl, A. E. and Kennard, R. W. (1970). “Ridge regression: Biased estimation for nonorthogonal problems”. In: *Technometrics* vol. 12(1), pp. 55–67.

- Hollingsworth, Kieren G. (2014). “Quantitative MRI in muscular dystrophy”. In: *Neurology* vol. 83, no. 11, pp. 956–957.
- Janssen, Barbara et al. (2016). “Quantitative MRI reveals decelerated fatty infiltration in muscles of active FSHD patients”. In: *Neurology* vol. 86, no. 18, pp. 1700–1707.
- Jolliffe, I. T. (2002). *Principal Component Analysis*. Vol. 1. Springer New York.
- Mercuri, E. et al. (2002). “A short protocol for muscle MRI in children with muscular dystrophies”. In: *European Journal of Paediatric Neurology*.
- Mercuri, Eugenio et al. (2007). “Muscle MRI in inherited neuromuscular disorders: Past, present, and future”. In: *Journal of Magnetic Resonance Imaging* vol. 25, no. 2, pp. 433–440.
- Monforte, M. et al. (2019). “Tracking muscle wasting and disease activity in facioscapulohumeral muscular dystrophy by qualitative longitudinal imaging”. In: *J Cachexia Sarcopenia Muscle*.
- Nioche, Christophe, Orhac, Fanny, and Buvat, Irène (2020). *LIFEx User Guide*. <https://www.lifexsoft.org/images/phocagallery/documentation/LIFEx/UserGuide/LIFExUserGuide.pdf>.
- Paoletti, M et al. (2019). “Advances in Quantitative Imaging of Genetic and Acquired Myopathies: Clinical Applications and Perspectives”. In: *Frontiers in Neurology* vol. 10.
- Reimers, C. D. et al. (1994). “Magnetic resonance imaging of skeletal muscles in idiopathic inflammatory myopathies of adults”. In: *Journal of Neurology*.
- Santini, F. et al. (2021). “Fast Open-Source Toolkit for Water T2 Mapping in the Presence of Fat From Multi-Echo Spin-Echo Acquisitions for Muscle MRI”. In: *Frontiers in Neurology* vol. 12.
- Smith, DS et al. (2013). “Optimization of fat-water separation algorithm selection and options using image-based metrics with validation by ISMRM fat-water challenge datasets”. In: *Proceedings of the International Society for Magnetic Resonance in Medicine*. Vol. 21.
- Tawil, R., Kissel, J.T., et al. (2015). “Evidence-based guideline summary: Evaluation, diagnosis, and management of facioscapulohumeral muscular dys-

- trophy: Report of the Guideline Development, Dissemination, and Implementation Subcommittee of the American Academy of Neurology and the Practice Issues Review Panel of the American Association of Neuromuscular Electrodiagnostic Medicine”. In: *Neurology*.
- Tawil, R., Maarel, SM. van der, and Tapscott, S.J. (2014). “Faciocapulohumeral dystrophy: the path to consensus on pathophysiology”. In: *Skelet Muscle*.
- Tibshirani, R. (1996). “Regression shrinkage and selection via the lasso”. In: *Journal of the Royal Statistical Society: Series B (Methodological)* vol. 58(1), pp. 267–288.
- Timmeren, J. van et al. (2020). “Radiomics in medical imaging-”how-to” guide and critical reflection.” In: *J Neuromuscul Dis*.
- Weigel, M. (2015). “Extended phase graphs: dephasing, RF pulses, and echoes - pure and simple.” In: *Magn Reson Imaging*.
- Woolrich, M.W. et al. (2009). “Bayesian analysis of neuroimaging data in FSL.” In: *Neuroimage* vol. 45, pp. 173–86.

Box plot Fat Fraction (FF)



Box plot Water T_2 (wT_2)

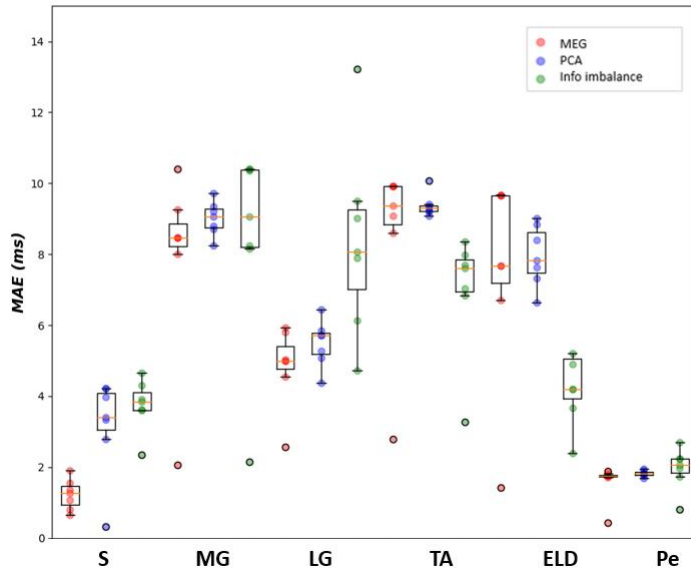
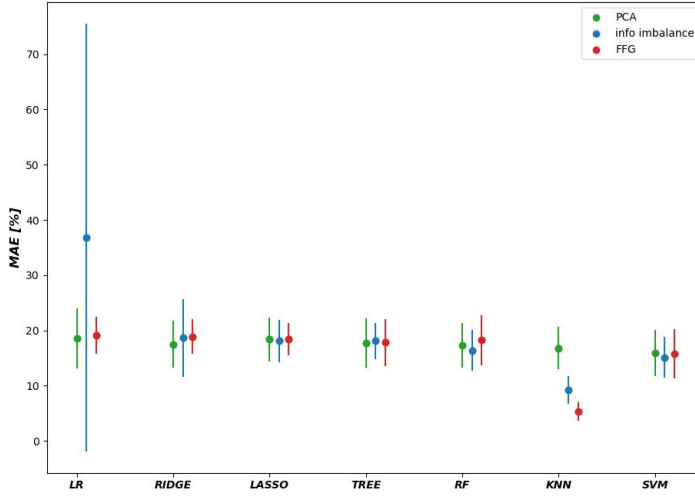


Figure II.2: Muscle-wise MAE boxplots (first quartile (Q1) to third quartile (Q3) and median value in orange line) for FF (top) expressed in percentage points (pp) and wT_2 (bottom) expressed in ms. Three boxplots are given for each muscle related to WF 1 (blue), WF 2 (green), WF 3 (red). Highest accuracy is related to red dots (FF, wT_2 boxplots) corresponding to KNN prediction performances.

Fat Fraction (FF) MAE Algorithm-wise



Water $T_2(wT_2)$ MAE Algorithm-wise

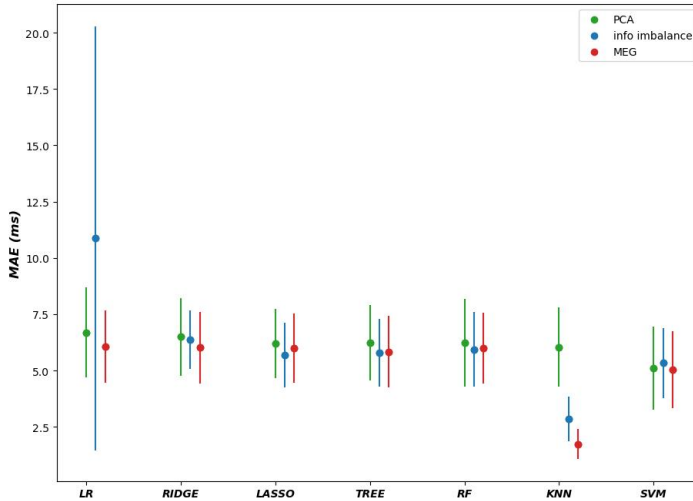
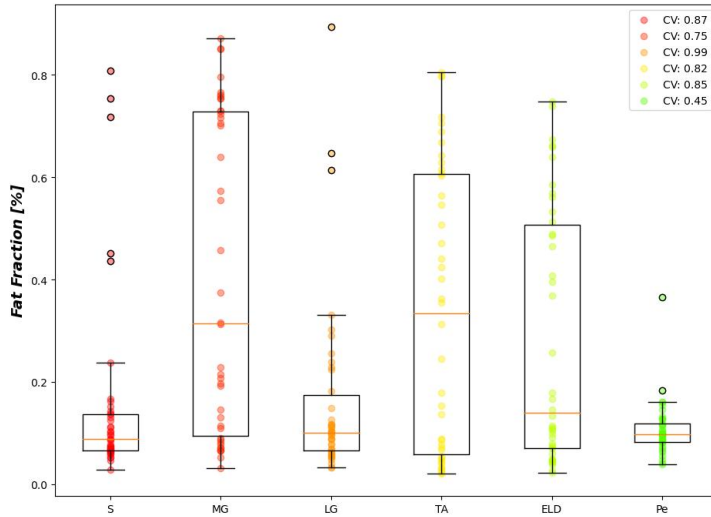


Figure II.3: FF (top) and wT_2 (bottom) prediction performances averaged on all muscles and showed as a function of the different implemented ML algorithms. According to the proposed workflows, a trio of mean prediction accuracy was define for each ML model, *i.e.*, green plot (WF1), blue plot (WF2), red plot (WF3).

Box plot gold standard FF



Box plot gold standard wT2

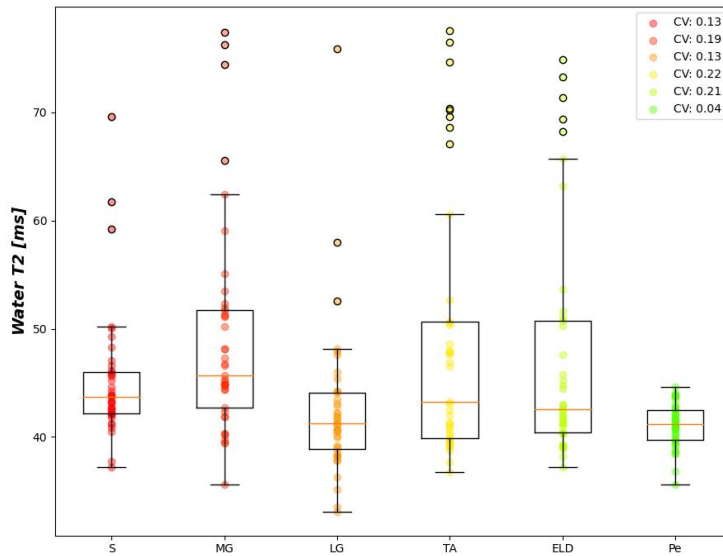


Figure II.4: Muscle-wise boxplots (first quartile (Q1) to third quartile (Q3) and median value in orange line) for FF (top) and wT2 (bottom) gold standard values, with CV listed in the legend.

Box plot Volume size

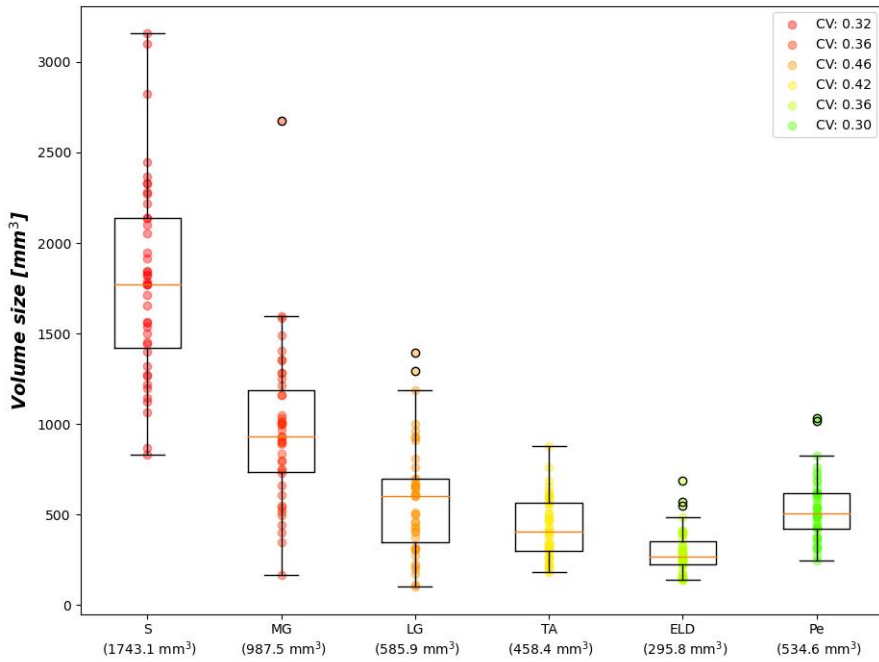


Figure II.5: Muscle-wise volume boxplots (first quartile (Q1) to third quartile (Q3) and median value in orange line). Muscle-wise mean volume size is reported in round brackets on x-axis, CV is listed in legend.

Paper III

Deep learning for automatic segmentation of thigh and leg muscles

Abramo Agosti^{1,2,*}, Enea Shaquiri¹, Matteo Paoletti¹,
Francesca Solazzo^{1,3}, Niels Bergsland⁴, Giulia Colelli^{1,2,5},
Giovanni Savini^{1,6}, Shaun I. Muzic⁷, Francesco Santini^{8,9},
Xeni Deligianni^{8,9}, Luca Diamanti¹⁰, Mauro Monforte¹¹,
Giorgio Tasca¹¹, Enzo Ricci¹¹, Stefano Bastianello^{1,12}, Anna
Pichiecchio^{1,12}

Published in *Magnetic Resonance Materials in Physics, Biology and Medicine*,
October 2021, DOI: [10.1007/s10334-021-00967-4](https://doi.org/10.1007/s10334-021-00967-4)

Abstract

Objective: In this study we address the automatic segmentation of selected muscles of the thigh and leg through a supervised deep learning approach.

Material and methods: The application of quantitative imaging in neuromuscular diseases requires the availability of regions of interest (ROI) drawn on muscles to extract quantitative parameters. Up to now, manual drawing of ROIs has been considered the gold standard in clinical studies, with no clear and universally accepted standardized procedure for segmentation. Several automatic methods, based mainly on machine learning and deep learning algorithms, have recently been proposed to discriminate between skeletal muscle, bone, subcutaneous and intermuscular adipose tissue. We develop a supervised deep learning approach based on a unified framework for ROI segmentation.

Results: The proposed network generates segmentation maps with high accuracy, consisting in Dice Scores ranging from 0.89 to 0.95, with respect to “ground truth” manually segmented labelled images, also showing high average performance in both mild and severe cases of disease involvement (*i.e.* entity of fatty replacement).

Discussion: The presented results are promising and potentially translat-

¹ Advanced Imaging and Radiomics Center, Neuroradiology Department, IRCCS Mondino Foundation, Pavia, Italy

² Dipartimento di Matematica, Università degli Studi di Pavia, Pavia, Italy

³ School of Specialization in Clinical Pharmacology and Toxicology Center of research in Medical Pharmacology, School of medicine University of Insubria, Varese, Italy

⁴Buffalo Neuroimaging Analysis Center, Department of Neurology, Jacobs School of Medicine and Biomedical Sciences and University of Buffalo, The State University of New York, Buffalo, NY, USA

⁵ INFN, Pavia Group, Pavia, Italy

⁶ Department of Neuroradiology, IRCCS Humanitas Research Hospital, Milano, Italy

⁷ University of Pavia, Pavia, Italy

⁸ Division of Radiological Physics, Department of Radiology, University Hospital Basel, Basel, Switzerland

⁹ Department of Biomedical Engineering, University of Basel, Allschwil, Basel, Switzerland

¹⁰ Neuro-oncology Unit, IRCCS Mondino Foundation, Pavia, Italy

¹¹Unità Operativa Complessa di Neurologia, Fondazione Policlinico Universitario A. Gemelli IRCCS, Roma, Italy

¹² Department of Brain and Behavioural Sciences, University of Pavia, Pavia, Italy

able to different skeletal muscle groups and other MRI sequences with different contrast and resolution.

Keywords: Deep learning, Muscle segmentation, Magnetic resonance imaging

III.1 Introduction

Recent technical advances of muscle MRI imaging have led to an evolution from traditional qualitative evaluation into what is currently known as quantitative imaging (qMRI), in which a large amount of diagnostically relevant information (such as fat substitution and edema) can be quantified and extracted from muscles of subjects affected by neuromuscular diseases (Carlier et al. [2016](#); Paoletti et al. [2019](#); Schroeder et al. [2019](#)). By using quantitative indicators, it is possible to make objective comparisons across subjects or time points to evaluate the natural history of disease progression or to use those parameters as potential outcome measures of therapeutic approaches. Muscle imaging protocols in the setting of qMRI often include several quantitative sequences, with the aim of evaluating different parameters, mainly intramuscular fat component (fat fraction, FF) and intramuscular free water relaxation (water T2, w-T2), but also diffusivity properties, size (muscle volume, cross-sectional area, CSA) etc. To extract quantitative data, drawing precise regions of interest (ROI) on selected muscles is crucial. The acquisition of multiple sequences on the same region also potentially requires registering ROIs to different datasets; such a process adds the further task to manually correct the registered ROIs in the final space where data are eventually extracted for statistical analysis.

Up to now, manual drawing of ROIs has been considered the gold standard for the extraction of quantitative data from muscles in clinical studies (Barnouin et al. [2014](#); Pons et al. [2018](#)). It requires dedicated and experienced human operators, long processing times and training curves, but also the necessity to select certain volumes of the entire muscle to limit the operator workload. Although muscle segmentation algorithms are not a novel concept (*e.g.* Barra and Boire [2002](#)), recent advances in hardware (offering faster processing) and in software/algorithms (new neural networks) made the potential much more promising. Therefore, the application of automatic tools to this field, mainly based on machine learning techniques and deep neural networks, already appears as particularly promising with the aim to accelerate data extraction and analysis

and eventually go beyond the manual process of ROI drawing and correction. A complete overview of the evolution of the MR image segmentation strategies is reported in Ogier et al. [2021]. Indeed, up to now automated segmentation tools have been successfully used to discriminate thigh tissues into skeletal muscle, bone, subcutaneous adipose tissue and intermuscular adipose tissue. In particular, recent studies applied diverse approaches including variational segmentation methods combined with statistical clustering-based techniques on T1-weighted scans (Gadermayr et al. [2018]; Orgiu et al. [2016]), machine-learning classification techniques on intensity-based features extracted from multi-contrast Dixon scans (Yang et al. [2016]), Deep Neural Networks (DNN) methods based on convolutional architectures combined with variational contour detector on T1-w scans (Yao et al. [2017]) and DNN methods based on an encoder-decoder U-net architecture (Ronneberger, Fischer, and Brox [2015]) combined with a clustering algorithm on T2 and proton density (PD) maps from multi spin echo scans (Amer et al. [2019]). Finally, Anwar et al. applied a semi-supervised deep learning approach based on an encoder-decoder architecture on multi-contrast Dixon scans (Anwar et al. [2020]). This latter work provided a unified framework to automatically segment both the multiple tissues regions and the edges of the fascia lata, which separates the adipose tissue domain into subcutaneous and inter-muscular.

All these aforementioned methods provided a high level of accuracy of the generated segmentation maps with respect to ground truth labelled images, ranging from 0.8 to 0.97 values of Dice Similarity Coefficient (DSC, a representative metrics of similarity between the segmented and ground truth maps) for the different tissues, with the deep learning based methods performing better in the cases of severe fat substitution (Amer et al. [2019]; Gadermayr et al. [2018]). Indeed, Gadermayr et al. showed that classical variational and machine learning segmentation methods worked well mainly in mildly involved subjects (*i.e.* with a low degree of fat replacement of muscular tissue), but actually had lower accuracy when examining subjects with advanced disease where fat replacement was predominant (Gadermayr et al. [2018]). In particular, they obtained average

levels of DSC accuracies of 0.90–0.95 for tissue segmentation in mild and moderate cases, whereas they obtained average DSC values of 0.67–0.85 in severely involved cases. The application of DNN methods in discriminating muscle tissues yielded to higher performances for severe cases. Other authors, in fact, found average DSC values of 0.93–0.96, depending on the input data type of the networks (Amer et al. [2019](#); Yao et al. [2017](#)).

As for the automatic segmentation of individual muscle regions, atlas-based approaches have been proposed in Le Troter et al. [2016](#) for the automatic segmentation of four muscles of the quadriceps femoris from T1-weighted scans of healthy subjects. In the latter work different registration methods, guided by an initial discrimination of thigh tissues obtained by means of a clustering algorithm, were evaluated, obtaining average DSCs ranging from 0.72 to 0.94 for the different muscles. Recently, Ding et al. reported a deep learning approach based on the U-net architecture which was applied to automatically segment 4 functional muscle groups of the thigh from multi-contrast Dixon scans, obtaining an average DSC on the training dataset > 0.85 (Ding et al. [2020](#)). The obtained DNN-generated segmentations were shown to be unsuitable for patients with markedly severe fat infiltration, since limited data of such cases were available to train their network. Indeed, they found average DSC values of 0.85–0.93 for the single thigh muscles considered, with the lowest value corresponding to the smallest muscle, but they declared (without further investigations) that their DNN was not suitable for patients with severe fat infiltration (Ding et al. [2020](#)).

Moreover, in Renkun et al. [2019](#) a cascade 3-D convolutional DNN segmentation framework, consisting of two-stage process, was designed to capture location and detailed features of muscles, reporting DSCs values of 0.78–0.97 for small and large muscles, respectively.

In the present work, as a further step towards the automatization of muscle ROI drawing, we aimed to develop an automatic segmentation tool based on deep learning techniques to create single-muscle segmentation maps at thigh and leg level, starting from manually segmented multi-contrast quantitative

muscle MRI scans of both healthy subjects and patients affected by two different neuromuscular diseases. In the interest of reproducibility and of benefiting the community, we are sharing the resulting automatic segmentation tool as an open-source repository, available at (Agosti et al. [2021](#)).

III.2 Materials and methods

III.2.1 Subjects

For this project, we included 54 subjects (6 healthy controls and 48 patients affected by facioscapulohumeral dystrophy (FSHD) ($n = 30$) and by amyotrophic lateral sclerosis (ALS) ($n = 18$), that presented muscle alterations. Each subject was scanned at different time points (up to three). Subjects gave their informed consent to the examination. This study was approved by the Local Ethics Committee.

III.2.2 MRI acquisition

All examinations were performed on a 3T MRI whole-body scanner (Skyra, Siemens Healthineers AG Erlangen, Germany) using integrated spine and body surface coils. The patient was lying supine in the scanner with 18-channel phased-array coils positioned either on the thighs and the legs during acquisition, with simultaneous acquisition of both sides (total scanning time of approximately 20 min for the thighs and 15 min for legs). The MRI protocol included a 3D six-point multi-echo gradient echo (GRE) sequence with interleaved echo sampling (matrix size = $432 \times 432 \times 52$ for the thighs, $432 \times 432 \times 36$ for the legs, TR = 35 ms, TE = 1.7–9.2 ms, resolution = $1.04 \times 1.04 \times 5.0 \text{ mm}^3$, bandwidth 1050 Hz/Px, flip angle 7°) and a 2D multi-slice multi-echo spin echo (MESE) sequence (matrix size = $384 \times 192 \times 7$ for the thighs, $384 \times 192 \times 5$ for the legs, TE = 10.9 ms both for the first TE and the echo spacing,

TR = 4100.0 ms, resolution = $1.2 \times 1.2 \times 10.0 \text{ mm}^3$, slice gap=30 mm, 17 echo times) at thigh and leg level.

III.2.3 Post-processing of MRI sequences

A total of 12 muscle ROIs per thigh and 6 muscle ROIs per leg for each side were manually drawn by a single experienced operator using ITK-snap v3.0 (Yushkevich, Gao, and Gerig 2016). ROIs were drawn on the first echo images of the MESE sequence by an expert operator (FS) with 3 years of experience, avoiding the muscle fascia and bone contours of the femur and tibia.

For what concerns the thigh, ROIs were drawn in the inner thigh slices (5 out of 7) of the MESE acquisition, equidistant from the femur head and the tip of the patella, and were subsequently registered to the multi-echo GRE dataset with the creation of new corresponding ROIs, which were manually adjusted by the same operator. Two additional ROIs were drawn in the GRE space in the neighboring slices to the medial registered slice, ending in a final number of 7 slices per thigh segmented.

For what concerns the leg, segmentation was performed in the third slice of the MESE acquisition and then subsequently registered to the multi-echo GRE dataset where it was manually adjusted. Two additional ROIs were drawn in the multi-echo GRE dataset on the neighboring slices, ending in a final number of 3 slices per leg segmented.

The slices to be segmented were chosen as the most representative of the upper, middle and lower thigh, and, for simplicity, only for the middle portion of the lower leg (also to include all the most important muscles that may not be represented especially in the lower slices closer to the ankle).

III.2.4 Training, validation and test dataset

We separated the available dataset of scanned subjects into training and validation subsets, for the DNN learning process, and a test subset for its testing. 44 subjects (comprising the 6 healthy controls) at the different time points, for a

total number of 110 scans, were included in the training and validation subsets, whereas remaining 10 patients at their initial scan time-point were included in the test subset.

A total number of 770 thigh and 330 leg slices with corresponding manually-drawn ground truth segmentations were thus available as a working dataset for the DNN learning process and cross-validation.

III.2.5 Preprocessing and data augmentation

We processed the input volume with a slice-wise approach. Figure [III.1](#) shows muscle segmentation of an exemplary subject, with segmented muscles reported in the figure legend. Each manual segmentation map was preprocessed through the application of consecutive area opening and closing filters, with an area threshold of 4 pixels, to eliminate small structures which resulted from noise in the registration operation of the MESE onto the GRE dataset.

We applied data augmentation to the available annotated slices in the training and validation datasets to gain robustness in the network predictions on unseen cases and to make the network learn realistic deformations without these being represented in the available training data. In particular, on each training and validation image and on each corresponding manual segmentation we randomly applied elements in the following sequence of transformations (bicubic spline interpolation was used for the input images, and nearest-neighbor interpolation was used for the binary segmentation masks):

- *Horizontal and vertical translations*: separate independent translations of the left and right thighs (or legs) per image in the horizontal and vertical directions, with bi-cubic spline interpolation. The amounts of each translation were uniformly sampled in an interval of values computed per image with the maximum value given by the shortest distance of the thighs (or legs) to the image borders. These transformations enhanced invariance with respect to the relative position between the left and right thighs (or legs) in the training process;
- *Rotations*: independent rotations of the left and right thighs (or legs) by

amounts uniformly sampled per image in the interval $[-7, 7]$ degrees, with bi-cubic spline interpolation. These transformations enhanced rotation-invariance in the training process;

- *Piecewise affine transformations*: separate affine transformations applied on each neighborhood of points on a 4×4 grid, with each grid point moving of an amount sampled from a normal distribution with scaled amplitude randomly sampled per image from the interval $[0.1, 1]$ percent of the image height/width. Bi-cubic spline interpolation was chosen to determine per-pixel values for the transformations. These transformations enhanced local distortions-invariance in the training process;

- *Elastic transformations*: local transformations obtained in terms of displacement fields with Gaussian kernel smoothing, with strength uniformly sampled per image from the interval $[0, 20]$ and standard deviation of the kernel uniformly sampled per image from the interval $[5, 10]$. Bi-cubic spline interpolation was chosen to determine new pixel values for the transformations. These transformations enhanced elastic distortions-invariance, representing realistic tissue variations, in the training process. The aforementioned data augmentation was applied to the available dataset of 770 thigh and 330 leg slices to obtain 5000 annotated images for thigh and leg respectively. We randomly separated this augmented dataset into a training dataset of 4500 elements and a validation dataset of 500 elements, to perform a cross-validation analysis on the network performance.

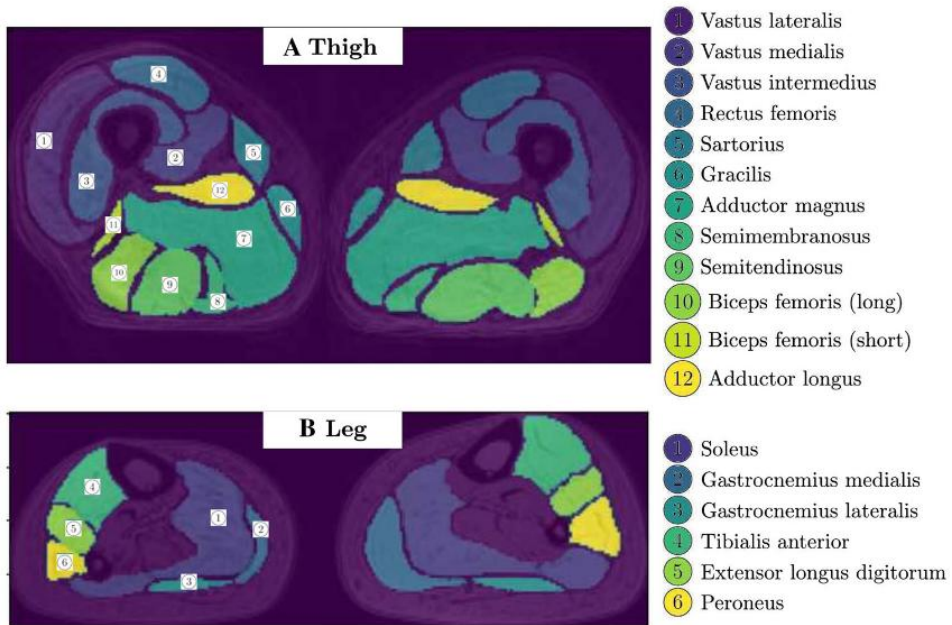


Figure III.1: Illustrative example of thigh and leg slices from MRI scans with the superposition of the corresponding muscles' manual segmentation and indications of the muscles' names. **A** Thigh case; **B** Leg case

III.2.6 Deep learning analysis

We considered the segmentation problems for the thigh's and leg's muscles as multi-class localized classification problems for the 2D images with 13 and 7 classes (comprising background and muscles) respectively, where a class label is assigned to each pixel. We achieved this goal using properly designed deep convolutional neural networks, inserted in a tree-like structure with two branches, where the inner node performs a global classification of the given input 2D image into a thigh's or leg's geometry, and according to the classification result two leaf nodes perform the corresponding segmentation task on the same input image. The deep convolutional networks used in this work were customized versions of the VNet (Milletari, Navab, and Ahmadi [2016](#)) and ResNet (He et al. [2016](#)) architectures, where a contracting network topology is used for the purpose of classification tasks and deep

features extraction from increasingly compressed levels of resolution, whereas an expanding network topology is used for resolution decompression and for the segmentation task. The VNet (Milletari, Navab, and Ahmadi [2016]) and ResNet (He et al. [2016]) architectures were developed to solve problems in biomedical image segmentation and image classification respectively, based on a fully convolutional architecture with the key extension that each convolutional layer learns a residual function. In particular, the VNet architecture was proven to ensure faster convergence during the learning process, mitigating the accuracy degradation with increased network depth, with respect to similar encoder–decoder architectures without residual units (e.g. the Unet network (Ronneberger, Fischer, and Brox [2015])). These networks and their variants have been applied with success in recent years in solving different image segmentation, classification and reconstruction problems (Litjens et al. [2017]), becoming the gold–standard DL tools for solving these tasks. The platform nn–Unet (Isensee et al. [2021]) recently showed that a basic U-Net, properly calibrated on specific datasets, was able to obtain the highest accuracy over quite different biomedical semantic segmentation tasks with respect to other even more sophisticated architectures. We thus choose to use VNet and ResNet architectures in our work, properly calibrated on our dataset (as will be explained in the sequel). Since we run our DL implementation on a CPU, we choose to use residual units to possibly accelerate the convergence of the training process and limit the needed computational resources. Before going into the details and rationale of the networks, we report in Fig. III.2 a graphical representation of the building blocks of the networks. The network weights were initialized from a Glorot normal distribution (Glorot and Bengio [2010]), and batch normalization (Ioffe and Szegedy [2015]) was applied at different levels, which normalized the distributions of the layers input and helped in quickening the learning convergence for deep networks. Each convolution and deconvolution operation was applied with appropriate constant padding, to keep equal dimensions between its input and output. The architecture of the residual block (RB) layers RB_l and RB_r was based on the scheme *Convolution–Batch Normalization–Skip*

Connection-Activation, which proved to give optimal convergence properties between the different ResNet implementations analyzed in literature. The network architectures and the learning algorithms were implemented in the *Tensorflow* platform (Abadi and al. 2015), using the deep learning interfaces provided by the Keras API (Chollet and al. 2015). The resulting DNN automatic segmentation tool has been shared as an opensource repository, available at Agosti et al. 2021.

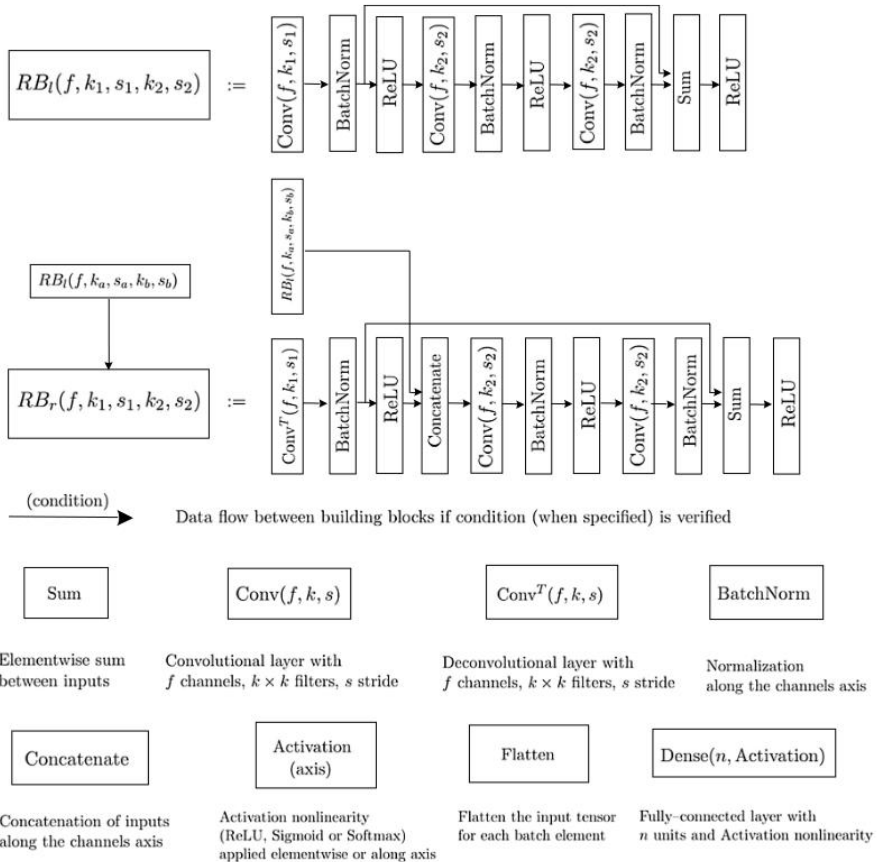


Figure III.2: Building blocks of the networks' architectures, with descriptions of the performed operations

III.2.7 Network architecture

Classification Network. In Fig. III.3 we report the network’s architecture for the classification task into the thigh’s or leg’s category.

The classification network takes as inputs down-sized images (to 128×128 size) through cubic spline interpolation and anti-aliasing, to reduce the computational burden. The input image goes through 5 residual block layers RB_l with doubled channel dimension and halved resolution at each level, extracting features at different spatial aggregation levels (receptive fields). The first residual block applies a first convolutional layer with 32 channels and unit kernel filter and stride, to map the input image to a first set of normalized outputs as a shortcut, after batch normalization, for the residual map. Then, a sequence of 2 convolutional layers with the same channel dimension, a 3×3 kernel filter and a unit stride are applied, to extract independent translation invariant features at this receptive field resolution after the application of nonlinear units. The remaining four residual blocks apply a first convolutional layer with doubled channel dimension with respect to the previous layer and a kernel filter and stride of dimension 2, working both as a downsampling and as a shortcut, after batch normalization, for the corresponding residual map. Then, a sequence of 2 convolutional layers with the same channel dimension, a 3×3 kernel filter and a unit stride is applied. Finally, all the extracted features at the different depth levels are collected into a vector of output neurons and used as an input to a fully connected layer for the binary classification task. The output of this final layer (indicated as **Output categorical** in Fig. III.5) consists of a two-dimensional vector of probabilities to belong to a specific category, given the one-hot representation (1, 0) for the thigh class and (0, 1) for the leg class.

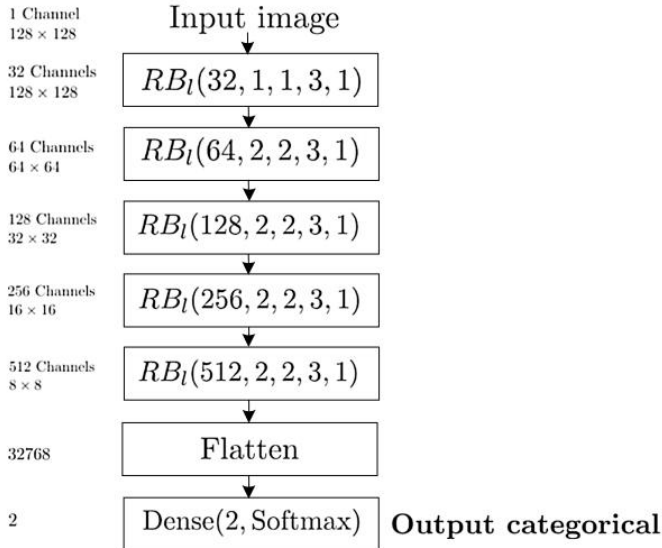


Figure III.3: Graphical representation of the network’s architecture for the classification task. The number of channels, spatial dimensions and number of neurons are indicated next to each building block, together with the indications of the input and the output of the data flow

Segmentation Networks Figure III.4 graphically represents the network’s architecture for the segmentation of both thigh’s and leg’s MRI.

The segmentation networks take as inputs the images with full 432×432 size. They are customized versions of the *VNet* (Milletari, Navab, and Ahmadi 2016), consisting of a fully convolutional architecture with a contracting path, composed by a sequence of 6 residual blocks RB_l , and an expanding path, composed by a sequence of 6 residual blocks RB_r . The first 5 residual blocks of the contracting path apply the same operations as the 5 residual blocks of the classification network. To extend the receptive field to cover the spatial resolution of the full 432×432 images and to introduce a higher number of features at more abstract aggregation levels, which is necessary to solve the segmentation task, we add a sixth layer with 1024 channels and a 1/3 downsampling. The 6 residual blocks of the expanding path increase the spatial resolution in a symmetric way with respect to the contracting path, halving

the channel dimension at each level and concatenating with the corresponding resolution features from the contracting path to recover context information. A final convolutional layer with unit kernel filter and stride is applied to map the 32 channels space to the desired probabilistic space with dimension given by the proper number of classes, after the application of the Softmax nonlinearity pixelwise.

We note that the use of small kernel filters (up to dimension 3×3) gave us the possibility to go deeper into the network’s architecture, introducing a fewer number of weights with respect to bigger filters when covering the same receptive fields, at the expense of adding additional layers. This reduced the dimensionality of the network and the computational burden. Also, it introduced smooth variations in the receptive fields between the different layers, distributing the spatial resolution of the extracted features uniformly on the spatial domain and thus covering the patterns’ variability at each spatial scale. To obtain this result, we had to ensure that the receptive fields cover the whole extension of the greatest objects detectable in the images (such as the whole thigh or leg). In Table [III.1](#) we report the progression of the receptive fields for each layer in the classification network (with input 128×128 images) and in the contracting path of the segmentation network (with input 432×432 images) in the tree-like network in Fig. [III.5](#).

We can observe from Table [III.1](#) that the receptive fields span uniformly through all the relevant spatial dimensions for 128×128 (first 5 residual blocks, reaching up to dimension 140×140) and for 432×432 images (all six residual blocks). In this latter case, we must consider that a single thigh or leg object extends up to half of the image, and the dimension 380×380 contain information about the single thigh (or leg) and the relative positions between left and right thighs (or legs).

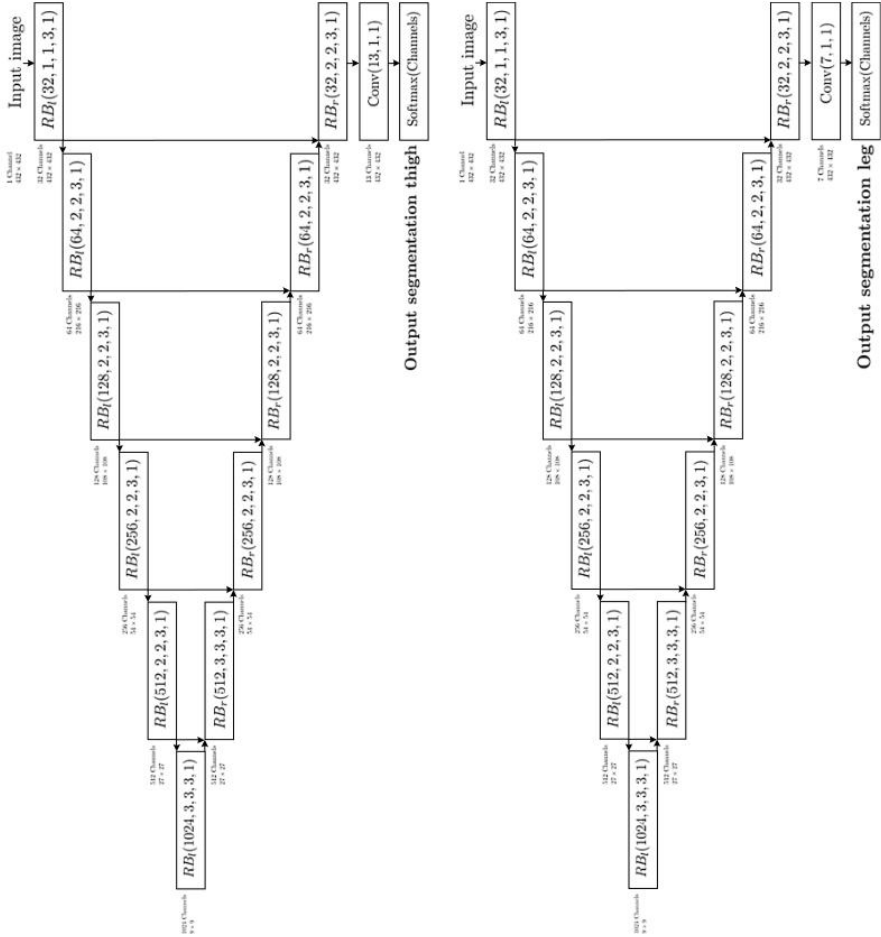


Figure III.4: Graphical representation of the network’s architecture for the segmentation tasks. The number of channels, spatial dimensions and number of neurons are indicated next to each building block, together with the indications of the input and the different outputs of the data flow

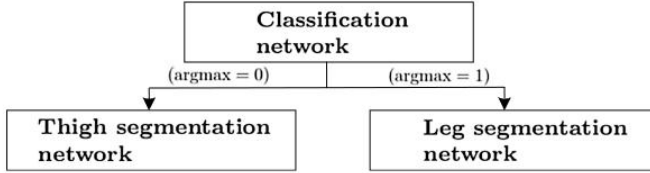


Figure III.5: Graphical representation of the network’s architecture as a tree-like structure

Residual Block RB_l	Receptive fields
$RB_l(32,1,1,3,1)$	$1 \times 1, 3 \times 3, 5 \times 5$
$RB_l(64,2,2,3,1)$	$6 \times 6, 10 \times 10, 14 \times 14$
$RB_l(128,2,2,3,1)$	$16 \times 16, 24 \times 24, 32 \times 32$
$RB_l(256,2,2,3,1)$	$36 \times 36, 52 \times 52, 68 \times 68$
$RB_l(512,2,2,3,1)$	$76 \times 76, 108 \times 108, 140 \times 140$
$RB_l(1024,3,3,3,1)$	$188 \times 188, 284 \times 284, 380 \times 380$

Table III.1: Receptive fields associated to each convolutional operation in the successive residual blocks RB_l

Networks concatenation. Figure [III.5](#) graphically represents the concatenation of the classification and segmentation networks for the classification and segmentation of both thigh’s and leg’s MRI.

It consists of a tree-like structure, where the inner node performs the classification of the 2D downsized input image into the thigh’s or leg’s category. The two branches of the network perform an argmax operation on **categorical Output**, splitting the data flow towards the left or right leaves depending on the classification outcome: if $\text{argmax} = 0$, the input image with full 432×432 size is processed by the left segmentation network with output a probabilistic segmentation for 13 classes (**Output segmentation thigh**), whereas, if $\text{argmax} = 1$, it is processed by the right segmentation network with output a probabilistic segmentation for 7 classes (**Output segmentation leg**).

III.2.8 Hyperparameters optimization, training and evaluation

The network was trained on the augmented dataset of input images and corresponding manual segmentations by means of a stochastic gradient descent method, including data subsampling in mini-batches and dropout regularization in the input layer. The accuracy of the network was monitored during training both on the training and validation datasets. We used the *AMSGrad* variant of the *Adam* algorithm (Kingma and Ba [2015]; Reddi, Kale, and Kumar [2015]) as an efficient method for stochastic optimization both from the computational and the convergence rate points of view. We also added L^2 weights regularization to the objective functions to reduce overfitting.

We first tuned the hyperparameters of the training algorithms by means of the hyperband algorithm (Li et al. [2018]), which adaptively allocate computational resources in an efficient way, choosing as a measure of configurations' performance the evaluation metrics on the validation dataset and exploring the discrete space of hyperparameters $(lr, dr, reg) \in (0.0001 \ 0.01) \times (0 \ 0.5) \times (0 \ 0.1)$, for 20 epochs keeping fixed the batch size to 5. Here, lr is the learning rate, dr is the dropout rate and reg is the factor for the L^2 weights regularization. Note that, thanks to the algebraic preconditioning introduced by the use of residual maps, the learning rate can take higher values than the typical optimized values given in Kingma and Ba [2015].

After hyperparameters optimization, the training algorithm was implemented with a scheduling which reduced the learning rate of the gradient method by a factor of 1/2 when no improvements in the validation loss were observed after 4 epochs, which helped in overcoming plateau domains and local minima of the loss objective functional.

We chose the *Categorical Cross-Entropy* - $\sum_{i=1}^2 gt_i \log(sf_i)$, where gt_i is the ground truth score of class i and sf_i is the output of the softmax activation, as the loss function for **Output categorical** in the classification part of the network. We moreover measured the classification network's accuracy on a

given dataset by means of the *Categorical Accuracy* metrics, which is defined as the percentage of predicted values that matches with the ground truth values. For what concerns the segmentation tasks, we considered a class-balanced *weighted Cross-Entropy* both for **Output segmentation thigh** and **Output segmentation leg**. The weights were chosen, as in Ronneberger, Fischer, and Brox [2015], to compensate the different frequency of pixels belonging to a certain class in the training dataset, thus giving more importance to foreground pixels than background ones during learning, giving in particular the most importance to pixels in small muscles, which are more difficult to segment. Moreover, the background regions separating neighboring muscles, computed using morphological operations as in Ronneberger, Fischer, and Brox [2015], were associated to large weights in order to force the network to learn separation borders and background regions between muscles. The weighted Cross-Entropy loss function had the following form

$$L = - \sum_{\mathbf{x} \in \Omega} w(\mathbf{x}) \log(p_{l(\mathbf{x})}(\mathbf{x})), \quad (\text{III.1})$$

where $p_{l(\mathbf{x})}$ is the output value of the Softmax layer at the pixel value $\mathbf{x} \in \Omega$ associated to pixel's true label $l(\mathbf{x}) \in \{1, \dots, 13\}$ or $\{1, \dots, 7\}$, and

$$w(\mathbf{x}) = w_{l(\mathbf{x})}(\mathbf{x}) + w_0 \exp\left(-\frac{(d_1(\mathbf{x}) + d_2(\mathbf{x}))^2}{2\sigma^2}\right), \quad (\text{III.2})$$

with $w_{l(\mathbf{x})}(\mathbf{x})$ the inverse of the frequency of the true class $l(\mathbf{x})$ in the training dataset and $d_1(\mathbf{x})$ and $d_2(\mathbf{x})$ the distances of pixel \mathbf{x} to the nearest muscle and second nearest muscle respectively. The value of σ was chosen to represent the maximum distance between neighboring muscles. We set $w_0 = 10$, $\sigma = 7$ for the thigh dataset and $\sigma = 8$ for the leg dataset. Finally, the segmentation's accuracy was measured by means of the *Dice* coefficient (DSC)

$$DSC = \frac{2TP}{FP + 2TP + FN}, \quad (\text{III.3})$$

which is a standard metrics for the overlap between the manual and the automatic segmentation, where TP, FP and FN are the numbers of true positive, false positive and false negative.

III.2.9 Network testing with a qualitative assessment for mild and severe disease conditions

We tested the performance of the network on the 10 patients of the test dataset, which were unseen during the learning process, by measuring the DSC between the manual and DNN generated segmentations for both their thighs and legs. As a secondary aim, to qualitatively test the performance of the network in the cases of mild and severe fat infiltrations, the 10 patients of the test dataset were chosen to include 5 subjects with mild and 5 subjects with severe fat replacement, on the basis of visual assessment of SE scans by the Mercuri scale (Mercuri et al. [2005](#)).

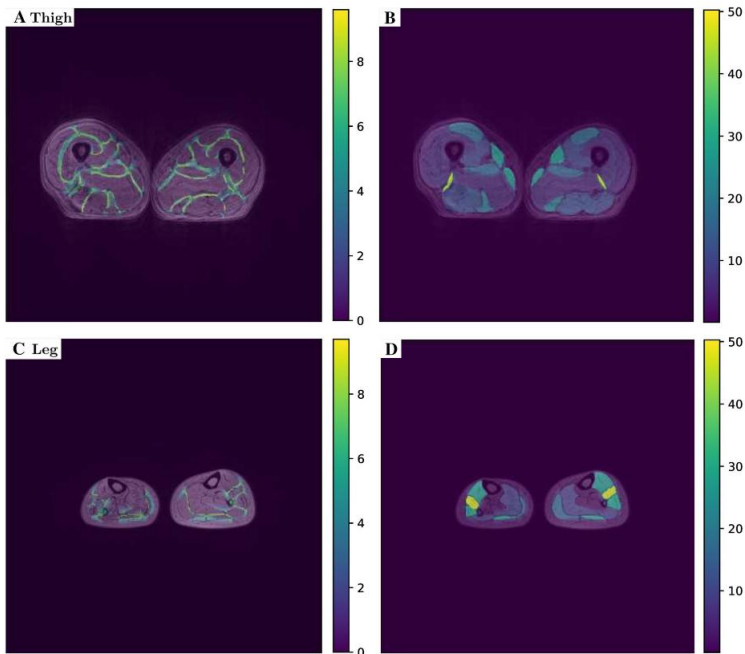


Figure III.6: Illustrative example of thigh and leg plots of the weight maps ([III.2](#)). **A** Weights map associated to the background regions separating neighboring muscles for the thigh case; **B** Full weight map for the thigh case; **C** Weights map associated to the background regions separating neighboring muscles for the leg case; **D** Full weight map for the leg case

III.3 Results

To illustrate the results of the DNN input creation step, in Fig. III.6 we show an illustrative example for the thigh and leg geometries with the plots of the weight maps associated to the background regions separating neighboring muscles [(second term in the right-hand side of III.2) and of the full weight maps (Eq. III.2)]. We can observe that the background regions separating neighboring muscles are associated to a high value of the weight, while the highest weight values are associated with the smallest muscles.

III.3.1 Hyperparameters optimization, training and validation

We first tuned the hyperparameters of the training algorithm for the left segmentation network in Fig. III.5, working on the thigh dataset, and we obtained the optimized values $lr = 0.009765$, $dr = 0.2$, $reg = 0.01$, by which averaged DSC of 0.8744 on the training dataset and 0.8487 on the validation dataset were obtained after 20 epochs. We used these optimized values of the hyperparameters also for the other segmentation and classification networks in the tree.

In Fig. III.7 we show the plots of the model losses and model accuracies during the training, with optimized hyperparameters, of the classification and segmentation network nodes in the tree-like architecture in Fig. III.5

We found that the *Categorical accuracy* of the classification network and the DSC of the segmentation networks had an overall monotonical increase during training on both the training and validation datasets, reaching a plateau which invariably happens after 40 epochs of training for all the networks.

In Table III.2 we also report the Categorical accuracy and DSC for the classification and the segmentation networks obtained after 40 epochs of training.

We thus obtained 100% accuracy of the thigh-leg classification network on both the training and the validation dataset. We highlight the fact that, since the classification network must solve a binary classification problem based on the overall extended spatial features which distinguish between the thigh's and the leg's morphology, we found that working on down-sized images to 128×128 dimension was sufficient to achieve 100% accuracy for the classification problem. Indeed, it was unnecessary to extract localized features from the full resolution image to solve this task. We obtained high DSC for both the thigh and leg segmentation networks, namely 93% and 95% respectively on the training dataset, and 89% and 93% respectively on the validation dataset.

In Fig. [III.8](#) we report illustrative comparisons between the manual segmentation and the DNN generated segmentation for three elements randomly chosen in the training dataset and three elements randomly chosen in the validation dataset, for both the thigh and the leg case.

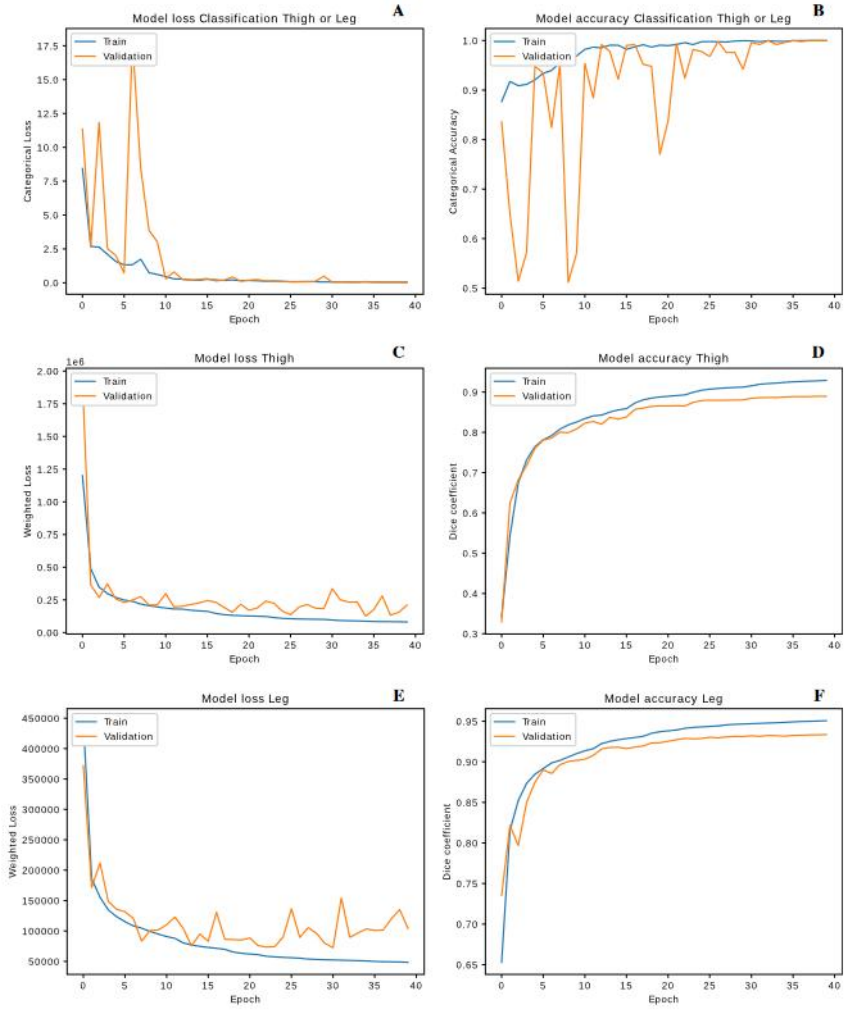


Figure III.7: Plots of the model losses and model accuracies during the training of the classification network (**A** and **B**), the thigh segmentation network (**C** and **D**) and the leg segmentation network (**E** and **F**)

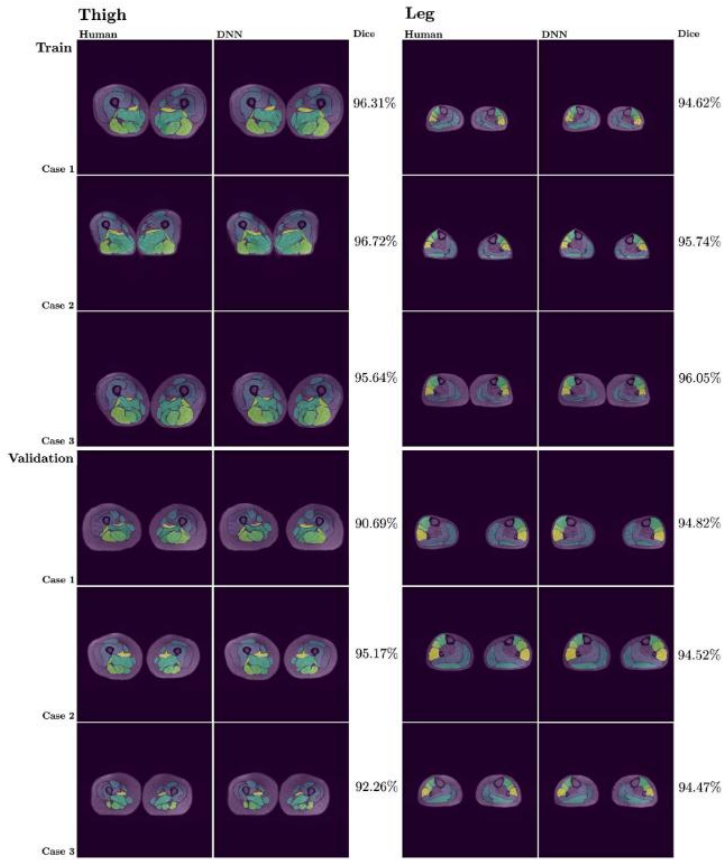


Figure III.8: Illustrative comparisons between the manual segmentation and the network (DNN) generated segmentation for three elements in the training and three elements in the validation datasets, for both the thigh and leg case, with the corresponding *Dice coefficient* score

network type	Train accuracy	Validation accuracy
Classification network	Categorical	Categorical
	1.0	1.0
Thigh segmentation network	DSC	DSC
	0.9292	0.8894
Leg segmentation network	DSC	DSC
	0.9507	0.9336

Table III.2: Model accuracy after 40 epochs

III.3.2 Network testing

With regards to the test dataset including selected subgroups of subjects with mild or severe fat replacement (see Sect. III.2.9), we found that the network segmentation had good and comparable performances for both mild and severe cases, with average 88% and 93% accuracies, respectively for the thigh and the leg, for the subjects with mild fat replacement, and average 87% and 93% accuracies, respectively for the thigh and the leg, for the subjects with severe fat replacement. In Table III.3 we report the average DSC over the slices, obtained by the network for the 10 test subjects, separated into two subgroups with mild or severe fat replacement.

Figures III.9 and III.10 report the 10 selected cases, with an indication of the DSC metrics for single slices. The bottom (leftmost column), inner and top (rightmost column) slices are reported for the thigh, whereas the inner slice is reported for the leg.

Finally, to evaluate the performance of the DNN on the slices throughout the 3D stack that were unseen during the training process, our expert operator manually segmented 4 additional slices around the middle portion of the thigh and the leg for two subjects randomly chosen in the test dataset, subject A and subject B, both with severe disease involvement (with subject B presenting a higher degree of severity with respect to subject A). In Fig. III.11 we show two coronal and sagittal slices along the 3D stack of the thigh and leg images for subject A and subject B, together with the manual and the DNN generated segmentation.

in Table III.4 we also report the DSC between the manual and the DNN generated segmentations on the 4 additional slices manually segmented along the 3D stack for both Subject A and Subject B.

We can observe an overall decrease of the DNN performance to DSC between 0.75 and 0.90 on the slices throughout the 3D stack that were unseen during the training process (at least on the slices around the middle portion of the thigh and the leg of the subjects).

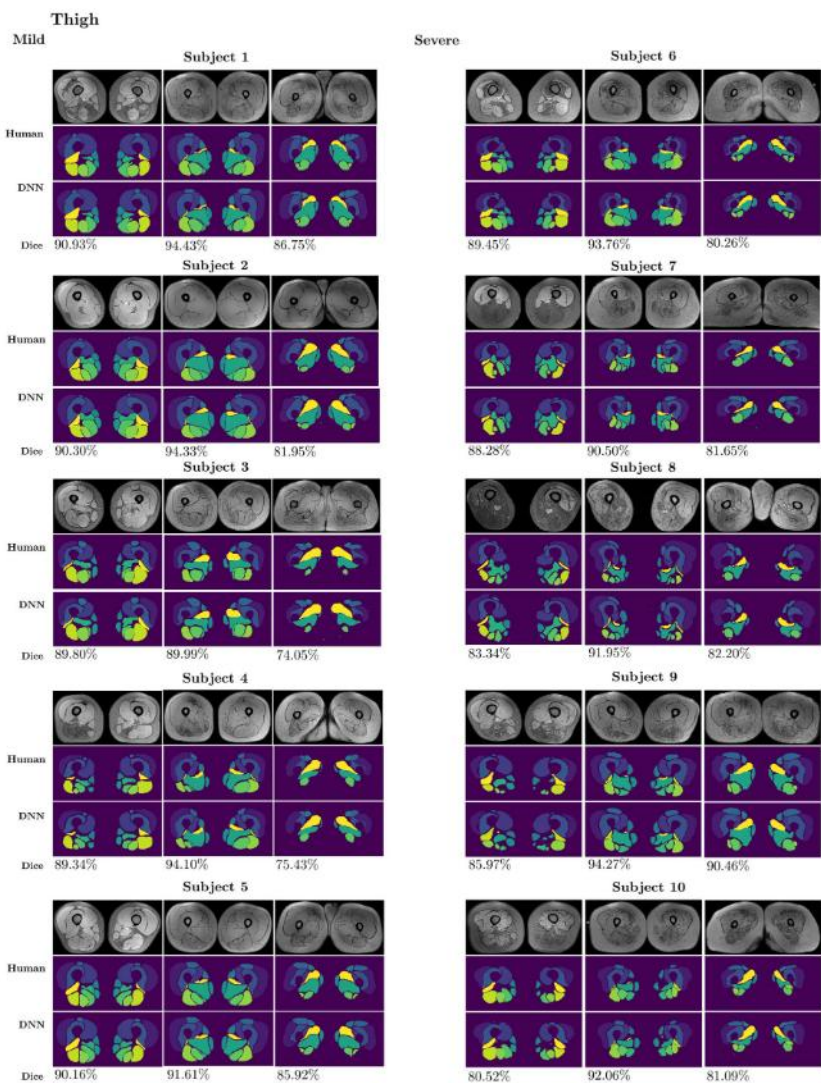


Figure III.9: Comparisons between the manual segmentation and the network (DNN) generated segmentation of thigh muscles for 5 patients with mild and 5 patients with severe fat infiltrations in the test dataset. The bottom (leftmost column), inner and top (rightmost column) slices are reported

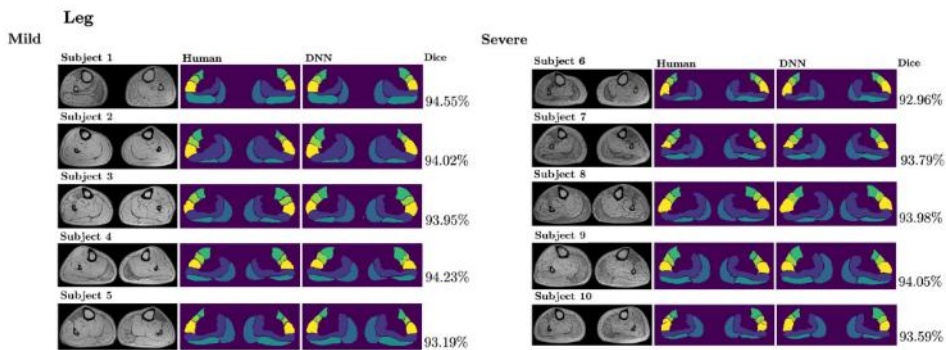


Figure III.10: Comparisons between the manual segmentation and the network (DNN) generated segmentation of leg muscles for 5 patients with mild and 5 patients with severe fat infiltrations in the test dataset. The inner slice is reported

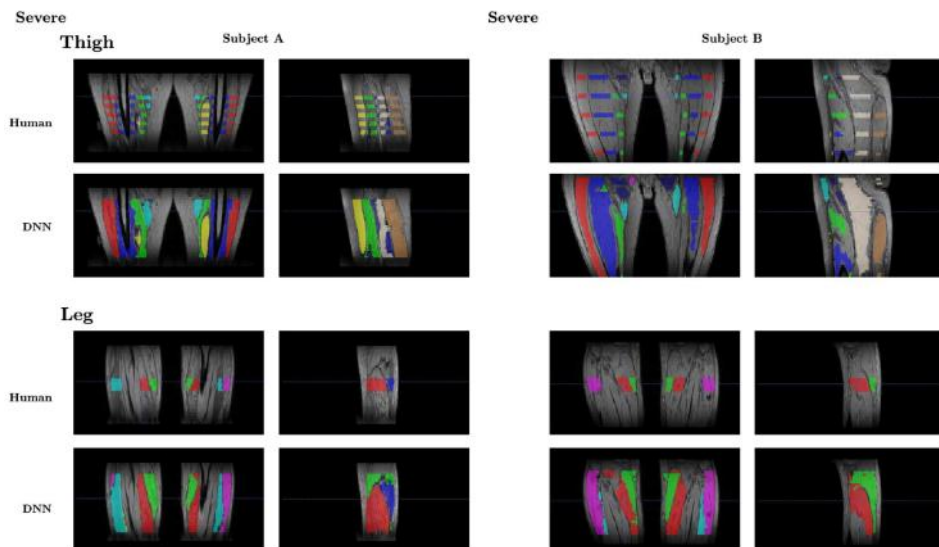


Figure III.11: Comparisons between the manual segmentation and the network (DNN) generated segmentation of the thigh and leg muscles for subject A and subject B, shown along with two coronal and sagittal slices

Subject	Thigh Average DSC	Leg Average DSC
Mild		
Subject 1	0.9009	0.9367
Subject 2	0.9016	0.9310
Subject 3	0.8531	0.9319
Subject 4	0.8651	0.9341
Subject 5	0.8892	0.9243
Severe		
Subject 6	0.8762	0.9247
Subject 7	0.8765	0.9295
Subject 8	0.8695	0.9303
Subject 9	0.8923	0.9331
Subject 10	0.8643	0.9285

Table III.3: Average DSC for the 10 test subjects, with an indication of their disease severity

III.4 Discussion

In this study, we approached the automatic segmentation of selected muscles from MRI scans, working on a training dataset composed by thighs and legs of both healthy subjects and patients affected by two different diseases with muscle involvement, and testing the results on a dataset including two subgroups with mild or severe fat replacement. With the aim to standardize and accelerate the process of ROI drawing we developed a deep neural network architecture, consisting of a classifier and two segmentation networks with residual units and contracting and expanding topologies inserted in a tree-like structure, which gave a unified framework for the automatic segmentation of both thigh and leg muscles. Our experience proved the feasibility of a convolutional neural network approach into the automatic segmentation of muscles ROIs for both thighs and legs, with very high accuracy. Specifically, the DNN showed an average DSC of 0.93 and 0.89 on the training and validation sets for the thighs, and of 0.95 and 0.93 on the training and validation sets for the legs, compared to the manually segmented reference ROIs. On the test dataset, an average DSC of 0.88 and 0.87 is found for the thighs of subjects with mild and severe fat replacement respectively, whereas a value of 0.93 is found for the legs of the subjects in both

subgroups. We hypothesize that the leg segmentation network we used actually performed better with respect to the thigh segmentation due to a minor variance in the available manually segmented slices along the scanned volume.

The accuracy level obtained by our network was comparable with results obtained by deep neural networks applied to discriminate between different tissues (*i.e.* fat, muscle tissue, etc.) found in the literature. Such studies which used deep learning methods to discriminate thigh and leg tissues from MRI scans obtained very high accuracy performances, namely DSC of 0.97, 0.94 and 0.80 (Anwar et al. [2020](#)) and 0.96, 0.92 and 0.93 (Amer et al. [2019](#)) for muscle, fat and inter-muscular adipose tissue respectively. In our study, however, as in Ding et al. [2020](#) we used a different approach as we started from ground truth segmentation of muscles based on their anatomy, resulting in a network capable of replicating the manual segmentation of muscles ROIs done by hand. As muscle MRI studies and also clinical trials often concentrate on single slices or restricted group of muscles as focus for their analysis, the possibility to quantify muscle tissue parameters on a single-muscle level is, in our opinion, of more practical interest. For what concerns tissue segmentation of selected muscles (ROI-based approach), Ding et al. [2020](#) found average DSC values of 0.85–0.93 for the single thigh muscles considered, with the lowest value corresponding to the smallest muscle, while DSC values of 0.78–0.97 have been reported in Renkun et al. [2019](#) for small and large muscles respectively. Even if our work exploits 2D slices it reaches results similar to the 3D network topology reported in Renkun et al. [2019](#), with the advantage to train only one network for all thigh’s muscles and only one for all leg’s muscles in contrast to Renkun et al. [2019](#) in which the authors train individual networks for each target muscles.

As explained in the Methods, the network was trained on the augmented dataset by means of a stochastic gradient descent method, with a schedule of the learning rate to overcome plateau domains of the loss objective functionals. The hyperparameters of the networks were chosen in advance by solving an adaptive optimization problem based on monitoring the DSC on the validation dataset. The proposed supervised training algorithms converged with an

overall monotone behavior to a local minimum for each component networks, proving robustness of the learning process. We cross-validated the networks performances on a validation set of unseen slices, which were excluded from the training dataset, and we tested their performances on a test dataset of unseen subjects, obtaining very high DSC values between the human and network generated segmentations, in the order of 90%.

In addition to this our classification network obtained a 100% accuracy, both over the training and validation datasets, in classifying between the thigh or leg geometry. This paves the way to a consistent extension of our deep learning network to automatically segment proper labels for different anatomical districts, once the classifier is also trained on a properly adapted dataset from different sequences with different contrast and resolutions.

One secondary aim of our study was to evaluate whether the performance of our DNN was affected by the different level of muscle involvement (*i.e* more or less fat replaced muscles) in the subjects. We found that when evaluating subjects with mild disease involvement, our DNN showed a high level of accuracy, comparable to that of previous tissue discriminating networks and also to the previous experience of Ding et al. [2020] and Renkun et al. [2019]. Differently from the reported literature and due to the subjects' variability in our data set (control subjects and subjects affected by different diseases), a high level of accuracy was also obtained by our DNN when evaluating subjects with the most severe disease involvement.

The current study had some limitations. First, since ground truth segmentations were available only on selected slices of the MRI volume stack (see Sect. III.2.3), the DNN performance on the other slices that were unseen during the training process is lower than on selected slices, and manual corrections were needed on the DNN generated segmentations on unseen slices in the overall subject volumes. Second, the DNN was trained and tested only on the available thigh and leg datasets, achieving high accuracy performances, but an external validation and eventually incremental training on independent datasets acquired with different sequence parameters or even different sequences or systems

would be further needed to ensure the reproducibility of our segmentation tool to clinical practice. Also no evaluation was performed on data from healthy volunteers. As a future development, incremental learning will be used to incorporate information from other contrasts and thus aim at a higher generalizability of the model.

Subject	Thigh DSC	Leg DSC
Subject A		
Subject 1	0.8041	0.9018
Subject 2	0.8063	0.8954
Subject 3	0.8058	0.9084
Subject 4	0.8113	0.9005
Subject B		
Subject 1	0.7514	0.8383
Subject 2	0.7546	0.8529
Subject 3	0.7520	0.8447
Subject 4	0.7327	0.8390

Table III.4: DSC for the 4 additional slices for Subject A and Subject B

III.5 Conclusion

In this study, we explored the applicability of deep neural networks in ROI drawing of muscles of the lower limbs, with promising results in terms of accuracy compared to the standard manual reference currently in use. The application of neural networks to substitute or at least greatly accelerate the work of human operators in ROI drawing can be extremely helpful in clinical studies, where a large amount of data have to be analyzed. Once reliable dedicated datasets of muscle ROIs are collected, deep neural networks can be promisingly applied for segmentation of other sequences with different contrast and image resolution and also to different anatomic districts.

References

- Abadi, M and al., et. (2015). “ TensorFlow: large-scale machine learning on heterogeneous systems ”. In.
- Agosti, A. et al. (2021). “Deep learning for automatic segmentation of thigh and leg muscles.” In: *Magma (New York, N.Y.)*
- Amer, R. et al. (2019). “ Automatic segmentation of muscle tissue and inter-muscular fat in thigh and calf MRI images”. In.
- Anwar, S.M. et al. (2020). “Semi-supervised deep learning for multi-tissue segmentation from multi-contrast MRI”. In.
- Barnouin, Y. et al. (2014). “ Manual segmentation of individual muscles of the quadriceps Femoris using MRI: a reappraisal”. In: *J Magn Reson Imaging* vol. 40, pp. 239–247.
- Barra, V. and Boire, J.Y. (2002). “ Segmentation of fat and muscle from MR images of the thigh by a possibilistic clustering algorithm”. In: *J Magn Reson Imaging* vol. 68 (3), pp. 185–193.
- Carrier, P. et al. (2016). “Skeletal muscle quantitative nuclear magnetic resonance imaging and spectroscopy as an outcome measure for clinical trials”. In: *J Neuromuscul Dis.* vol. 3, pp. 1–28.
- Chollet, F. and al., et. (2015). “ Keras”. In.
- Ding, J. et al. (2020). “ Deep learning-based thigh muscle segmentation for reproducible fat fraction quantification using fat-water decomposition MRI.” In: *Insights Imaging.*
- Gadermayr, M. et al. (2018). “ A comprehensive study on automated muscle segmentation for assessing fat infiltration in neuromuscular diseases.” In: *J Magn Reson Imaging* vol. 48, pp. 20–26.
- Glorot, X. and Bengio, Y. (2010). “ Understanding the difficulty of training deep feedforward neural networks”. In: *Proceedings of the Thirteenth International Conference on Artificial Intelligence and Statistics, JMLR Workshop and Conference Proceedings 9*, pp. 249–256.

- He, K. et al. (2016). “ Deep residual learning for image recognition.” In: *2016 IEEE Conference on Computer Vision and Pattern Recognition (CVPR), Las Vegas, NV*, pp. 770–778.
- Ioffe, S. and Szegedy, C. (2015). “ Batch normalization: accelerating deep network training by reducing internal covariate shift”. In: *Proceedings of the 32nd International Conference on Machine Learning, PMLR 37*, pp. 448–456.
- Isensee, F. et al. (2021). “ NNU-net: a self-configuring method for deep learning-based biomedical image segmentation”. In: *Nat Methods* vol. 18 (2), pp. 203–211.
- Kingma, D. and Ba, L. (2015). “ Adam: a method for stochastic optimization”. In: *International Conference on Learning Representations (ICLR), ICLR*, pp. 448–456.
- Le Troter, A. et al. (2016). “ Volume measurements of individual muscles in human quadriceps femoris using atlas-based segmentation approaches.” In: *MAGMA* vol. 29, pp. 245–257.
- Li, L. et al. (2018). “ Hyperband: a novel bandit-based approach to hyperparameter optimization”. In: *J Mach Learn Res* vol. 18, pp. 1–52.
- Litjens, G. et al. (2017). “ A survey on deep learning in medical image analysis.” In: *Med Image Anal.*
- Mercuri, E. et al. (2005). “ Muscle MRI in ullrich congenital muscular dystrophy and bethlem myopathy”. In: *Neuromuscul Disord* vol. 15(4), pp. 303–310.
- Milletari, F., Navab, N., and Ahmadi, S. (2016). “ V-net: fully convolutional neural networks for volumetric medical image segmentation”. In: *2016 Fourth International Conference on 3D Vision (3DV), Stanford, CA*, pp. 565–571.
- Ogier, A.C. et al. (2021). “ SOver- view of MR image segmentation strategies in neuromuscular disorders.” In: *Front Neurol.*
- Orgiu, S. et al. (2016). “ Automatic muscle and fat segmentation in the thigh from t1-weighted MRI”. In: *J Magn Reson Imaging* vol. 43, pp. 601–610.

- Paoletti, M et al. (2019). “Advances in Quantitative Imaging of Genetic and Acquired Myopathies: Clinical Applications and Perspectives”. In: *Frontiers in Neurology* vol. 10.
- Pons, C. et al. (2018). “Quantifying skeletal muscle volume and shape in humans using MRI: a systematic review of validity and reliability”. In: *PLoS One*.
- Reddi, S., Kale, S., and Kumar, S. (2015). “On the convergence of Adam and beyond.” In: *Int Conf Learn Represent (ICLR), ICLR*.
- Renkun, R. et al. (2019). “Automatic segmentation of all lower limb muscles from high-resolution magnetic resonance imaging using a cascaded three-dimensional deep convolutional neural network”. In: *J Med Imaging* vol. 6 (4).
- Ronneberger, O., Fischer, P., and Brox, T. (2015). “U-net: convolutional networks for biomedical image segmentation”. In: *Medical Image Computing and Computer-Assisted Intervention – MICCAI 2015. Lecture Notes in Computer Science* vol. 9351, pp. 234–241.
- Schroeder, J. et al. (2019). “Intra-rater and inter-rater reliability of quantitative thigh muscle magnetic resonance imaging”. In: *Imaging Med* vol. 11(2).
- Yang, Y.X. et al. (2016). “Automated assessment of thigh composition using machine learning for dixon magnetic resonance images”. In: *MAGMA* vol. 29(5), pp. 723–731.
- Yao, J. et al. (2017). *Holistic segmentation of intermuscular adipose tissues on thigh MRI*. In: *Descoteaux M, Maier-Hein L, Franz A, Jannin P, Collins D, Duchesne S (eds) Medical image computing and computer assisted intervention MICCAI 2017. Lecture notes in computer science*. Vol. 10433. Springer, Cham.
- Yushkevich, P.A., Gao, Y., and Gerig, G. (2016). “Itk-snap: an interactive tool for semi-automatic segmentation of multi-modality biomedical images.” In: *38th Annual International Conference of the IEEE Engineering in Medicine and Biology Society (EMBC)*, pp. 3342–3345.

Part 2

**Kinetic Theory and
Uncertainties Quantification
for Tumor Growth**

Introduction

Tumor formation and evolution is the result of different and complex multistep processes. The latter starts with unrepaired DNA damages or epigenetic alteration (a mutation in the expression of a gene) caused by environmental and genetic factors that lead to genome alteration and abnormal proliferation of a single cell in absence of apoptosis (Frank [2018](#)). Cell proliferation drives the outgrowth of a population clonally derived from the initial mutated cell (Cooper, Hausman, and Hausman [2007](#)). Then, tumor progression is sustained by additional mutations within cells which confer selective advantages, such as more rapid-growing and increasingly malignant characteristics.

In the past decades, several mathematical models have been developed to describe and predict the growth trend of the tumor progression. The goal of these efforts is to aid in the understanding of the root causes of solid tumor and metastasis, in the explanation of experimental and clinical observations for the purpose of finding new treatment strategies, which could eventually optimize therapy protocols and minimize patient suffering (Cristini and J. Lowengrub [2010](#), J. S. Lowengrub et al. [2009](#)). The easiest but still most used way to model the cancer growth law or rather the evolution in time of the tumor volume is by ordinary differential equations (ODEs), usually named according to the form of the right-hand side, *e.g.* Malthus (*i.e.*, the exponential growth law), Verhulst (*i.e.*, logistic growth law), Gompertz, Von Bertalanffy and West (see Marušić, Vuk-Pavlovic, and Frejer [1994](#); West, Brown, and Enquist [2001](#); Wodarz and Komarova [2014](#)). Most of these models show a similar sigmoidal trend with an asymptotic tendency to an equilibrium due to the presence of a carrying capacity (Preziosi, Toscani, and Zanella [2021](#)). The definition of the model parameters is obtained through an optimization procedure in a way that the

resulting trajectory of the models fit the collected experimental and clinical data. More recent works approach the description from different representation scales: discrete models focus on microscopic and mesoscopic scale, continuum model on macro scale and the hybrid ones combine both previous representations. For further details see Preziosi, Toscani, and Zanella [2021](#). Despite all the refined mathematical models used for studying cancer evolution there is no unanimous consensus on the type of growth law that is more appropriate to fit data and describe the tumor dynamics, with stochasticity often driving the difference among the predicted evolution associated to different models.

Rather than modeling the tumor with a stochastic version of the ODE growth models, we can describe it as an emerging collective and self-organized phenomenon whose behavior is the result of interactions at the microscopic level. In particular, we can consider the tumor as an ensemble of identical copies of the initial mutated cell, which interact mutually and with the surrounding environment. This approach allows us to take advantage of concepts and methods of the statistical physics and in particular of the kinetic theory of the rarefied gases (Pareschi and Toscani [2013](#)). Previous approaches in this direction could be found in Perthame [2006](#). The growth of the tumor volume is described in terms of distribution function. The temporal evolution of such distribution is the result of elementary interactions occurring at cellular level and characterized by a transition function which takes into account both random fluctuation and environmental influence, while being coherent with known microscopic ODE models for tumor growth. The microscopic system can be described through a Boltzmann-type equation expressing the thermalization of the particles towards an equilibrium distribution. The latter is the solution of a Fokker-Planck-type equation, obtained considering the *grazing limit* of the Boltzmann equation. Therefore, kinetic equations allow us studying the emergent behavior of tumor-complex-system and the spontaneous formation of spatio-temporal structures as result of local interactions. This also means that the statistical behaviour of the system is mainly related to the way agents interact and not to their internal complex structure.

The equilibrium distribution shows heterogeneous steady behavior according to different regimes of transition function parameters that translate in terms of different tails distribution decay. In particular, it is contemplated the steady solution of a generalized Gamma density function with slim tail, *i.e.* by an exponential decay, in the suitable limit of a transition function related to logistic-type growth and an Amoroso-type distribution with polynomial decay, *i.e.*, fat tail, in the case in which transition law is related to Von-Bertalanffy growth-type. Indeed, a lognormal-type of equilibrium with slim tail is associated to a Gompertz growth law. From a phenomenological point of view a fat-tailed distributions can take into account the possibility of having higher probability of finding large tumor.

In paper [IV](#) we also introduce a more realistic description that incorporates uncertainties in the tumor dynamics in order to take into account the proper body-response and the different clinical history of each patient. From a mathematical point of view, the introduced uncertainties at the cellular level translate into an increased dimensionality of the resulting kinetic problem that also affects the statistical equilibrium state. Consequently, the average behaviour of the tumor is the result of the superposition of different dynamics produced by different values of the variable associates to this extra dimensionality. In this scenario, we model therapies as a control, a deterministic external action that acts as an instantaneous correction of the microscopic interaction. The dumping of structural uncertainties of the system is achieved at macroscopic level. This is supported by the implementation of suitable numerical methods, based on stochastic Galerkin formulation of the resulting kinetic equations.

Thanks to the multiscale proprieties of the proposed model, we have the possibility to make a connection between cellular dynamics and observable patterns in a group of patient and so to calibrate the resulting kinetic model by means of experimental data. To validate theoretical and simulated results of the model we compared the patient tumor volume with the expected values of the first order momentum of the obtained distribution function, that is the expected dimension of the tumor volume predicted by the model. In our

work [IV](#), we consider the particular case of the very aggressive glioblastoma tumor, characterized by invasive cell migration, phenotypic plasticity, infiltrative growth morphologies (Alfonso et al. [2017](#)), robust angiogenesis mostly through the white matter and genomic instability (Furnari et al. [2007](#)). To construct the validating dataset, thus to estimate tumor volume at different time points for each subjects, we take advantage of the magnetic resonance imaging (MRI). More precisely we use the T1-weighted 3D MRI with contrast agent. This MRI sequence, exploiting the spin-lattice interactions, allows differentiating tissue type and anatomical structure on the base of longitudinal relaxation time.

Therefore, the combination of mathematical modelling through the kinetic theory and the extraction of information from magnetic resonance imaging give us the possibility to deal, from a different perspective, with the studying and prediction of the tumor volume evolution and to mimic the action of therapies in shrinking the tumor dimension towards a defined target volume.

References

- Alfonso, JCL et al. (2017). “The biology and mathematical modelling of glioma invasion: a review”. In: *Journal of the Royal Society Interface* vol. 14, no. 136, p. 20170490.
- Cooper, Geoffrey M, Hausman, Robert E, and Hausman, Robert E (2007). *The cell: a molecular approach*. Vol. 4. ASM press Washington, DC.
- Cristini, Vittorio and Lowengrub, John (2010). *Multiscale modeling of cancer: an integrated experimental and mathematical modeling approach*. Cambridge University Press.
- Frank, Steven A (2018). *Dynamics of cancer*. Princeton University Press.
- Furnari, Frank B et al. (2007). “Malignant astrocytic glioma: genetics, biology, and paths to treatment”. In: *Genes & development* vol. 21, no. 21, pp. 2683–2710.
- Lowengrub, John S et al. (2009). “Nonlinear modelling of cancer: bridging the gap between cells and tumours”. In: *Nonlinearity* vol. 23, no. 1, R1.

- Marušić, M., Vuk-Pavlovic, S., and Frejer, J. P. (1994). “ tumour growth in vivo and as multicellular spheroids compared by mathematical models ”. In: *Bull. Math. Biol.* vol. 56 (4), pp. 617–631.
- Pareschi, Lorenzo and Toscani, Giuseppe (2013). *Interacting multiagent systems: kinetic equations and Monte Carlo methods*. OUP Oxford.
- Perthame, Benoit (2006). *Transport equations in biology*. Springer Science & Business Media.
- Preziosi, Luigi, Toscani, Giuseppe, and Zanella, Mattia (2021). “Control of tumor growth distributions through kinetic methods”. In: *Journal of theoretical biology* vol. 514, p. 110579.
- West, G. B., Brown, J. H., and Enquist, B. J. (2001). “ A general model for ontogenetic growth”. In: *Nature* vol. 413, pp. 628–631.
- Wodarz, D. and Komarova, N. (2014). *Dynamics of Cancer: Mathematical Foundations of Oncology*. World Scientific.

Paper IV

Uncertainty quantification and control of kinetic models of tumour growth under clinical uncertainties

A. Medaglia¹, G. Colelli^{1,2}, L. Farina², A. Bacila², P. Bini³, E. Marchioni³, S. Figini⁴, A. Pichiecchio^{5,2}, M. Zanella^{1,*}

Published in *International Journal of Non-Linear Mechanics*, May 2022, DOI:

[10.1016/j.ijnonlinmec.2022.103933](https://doi.org/10.1016/j.ijnonlinmec.2022.103933)

Abstract

In this work, we develop a kinetic model for tumour growth taking into account the effects of clinical uncertainties characterising the tumours' progression. The action of therapeutic protocols trying to steer the tumours' volume towards a target size is then investigated by means of suitable selective-type controls acting at the level of cellular dynamics. By means of classical tools of statistical mechanics for many-agent systems, we are able to prove that it is possible to dampen clinical uncertainties across the scales. To take into account the scarcity of clinical data and the possible source of error in the image segmentation of tumours'

¹ Department of Mathematics "F. Casorati", University of Pavia, Italy

² Neuroradiology Department, IRCCS Mondino Foundation, Pavia, Italy

³ Neurology Department, IRCCS Mondino Foundation, Pavia, Italy

⁴ Department of Political and Social Sciences, University of Pavia, Italy

⁵ Department of Brain and Behavioural Sciences, University of Pavia, Italy

evolution, we estimated empirical distributions of relevant parameters that are considered to calibrate the resulting model obtained from real cases of primary glioblastoma. Suitable numerical methods for uncertainty quantification of the resulting kinetic equations are discussed and, in the last part of the paper, we compare the effectiveness of the introduced control approaches in reducing the variability in tumours' size due to the presence of uncertain quantities.

Keywords: kinetic modelling; tumour growth; uncertainty quantification; optimal control

IV.1 Introduction

The processes of tumour formation are highly complex phenomena involving different stages starting from damages in the DNA molecules leading to harmful mutations in the cell's genome that are not repaired in absence of cellular apoptosis. This mechanism leads to an unregulated mitosis and then to the formation of tumours. These mutations may be triggered by many aspects, including both environmental and genetic factors, see (Frank [2007](#); Grizzi and Chiriva-Internati [2006](#); Langer et al. [1980](#)).

In the last decades, extensive research efforts have been devoted to the mathematical formalisation of tumour growth dynamics and to the formalisation of growth factors, see *e.g.* (Albano and Giorno [2006](#); Gerlee [2013](#); Henscheid et al. [2018](#); Leory-Ler tre et al. [2017](#); Nobile and Ricciardi [1980](#); Rodriguez-Brenes, N. J. Komarova, and Wodarz [2013](#); Roose, J. Chapman, and Maini [2007](#)). Among the easiest way to describe these biological phenomena can be found in the literature of population dynamics to describe the evolution in time of the volume of a tumour. This modelling approach is based on first order ODEs that are named according to the form of the right-hand side. Leading examples are Gompertz and von Bertalanffy models. More recently, West and collaborators proposed a variation to the von Bertalanffy model in (G. B. West, Brown, and Enquist [2001](#)). It is worth mentioning that there is no unanimous consensus on the most appropriate modelling setting and several proposals have been introduced to better describe these dynamics. In particular, in (Preziosi, G. Toscani, and Zanella [2021](#)) the authors proposed a statistical approach based on kinetic theory to describe the growth of tumour cells in terms of the evolution of a distribution function. The temporal variation of such distribution is considered as a result of elementary transitions occurring at the cellular level which takes environmental cues and random fluctuations into account. The expected cellular variations are coherent with the mentioned ODE-based models in suitable limits. Furthermore, through the explicit computation of the equilibrium states of the resulting Fokker-Planck-type equation, we get

additional information on the decay of the tails. In particular, it is shown that von Bertalanffy-type models lead to fat tailed distributions of the volumes of tumours, whereas Gompertz-type models are linked to slim tailed distributions. The mathematical understanding of the behaviour of the tails is essential to quantify the probability of having tumours growing to sizes that are harmful to the human body. Existing kinetic models for statistical growth dynamics are linked to cell mutations (Kashdan and Lorenzo Pareschi [2012](#); Giuseppe Toscani [2013](#)). In Particular, in recent years a huge literature on mathematical modeling for glioma growth have been developed, (see Conte and Surulescu [2021](#); Engwer et al. [2015](#); Painter and Hillen [2013](#)) and the references therein.

Even if the mathematical simplicity of ODE-based modelling allows to handle more efficiently parameter estimation tasks, see *e.g.* Benzekry et al. [2014](#); Marušić, Vuk-Pavlovic, and Frejer [1994](#); Norton [1988](#); J. West and Newton [2019](#); Wheldon. [1988](#); Wodarz and N. Komarova [2014](#), the models based on partial differential equations are capable to describe the phenomenon under study in a statistical way (Loy and Preziosi [2020](#); Preziosi, G. Toscani, and Zanella [2021](#)) or highlighting the mechanical properties of the tissues, see *e.g.* Agosti et al. [2018](#); Giverso and Preziosi [2019](#). Furthermore, the lack of accurate clinical data introduces many sources of uncertainties stemming out at various levels of observation when facing the progression of human cancer. To mention a few, the main limitation consists in a limited set of observations due to clinical constraints. The second one may arise from the manual corrections of 3D semi-automatic tumours segmentation. The third comes from the fact that the evolution may differ strongly from one individual to another, since in each host the response of the body is influenced by many factors, like the clinical history of a patient. For these reasons, to produce effective predictions and to better understand the physical phenomena under study, we incorporate ineradicable uncertainties in the dynamics from the beginning of the modelling. The introduction of uncertain quantities points in the direction of a more realistic description of the underlying processes and helps us to compute possible deviations from the prescribed deterministic behaviour.

Once established the emerging distribution of the kinetic model in presence of uncertain quantities we further propose a robust approach to steer the system towards a prescribed target to mimic implementable therapeutic protocols. The control is here conceived as an additional external dynamics depending on the state of the system. The proposed control setting has roots in Boltzmann-type controls proposed in Albi, Fornasier, and Kalise. [2016](#) Albi, Herty, and L. Pareschi [2015](#); Albi and L. Pareschi [2018](#); Albi, L. Pareschi, and Zanella [2014](#) where an optimal control problem is solved at the microscopic level and then studied at the mesoscopic scale through classical methods of kinetic theory (Cercignani [1988](#); L. Pareschi and G. Toscani [2013](#)). This approach has connections with classical approaches for the control of mean-field equations, see Bensoussan, Frehse, and Yam [2013](#). Aside from the mentioned methods, the control of emergent behaviour has been studied also on the level of the microscopic agents, see *e.g.* Bailo et al. [2018](#) as well as fluid–dynamic equations. The contributions have to be further distinguished depending on the type of applied control. Without intending to review all literature we give some references on certain classes of control, *e.g.* sparse control (Fornasier, Piccoli, and Rossi [2014](#)), Nash equilibrium control (Degond, Herty, and Liu [2017](#)), control using linearised dynamics and Riccati equations (Herty, Steffensen, and L. Pareschi [2015](#)).

In the proposed setting, we discuss analytical properties of the asymptotic regime highlighting that a damping of structural uncertainties of the system is achieved at the macroscopic/observable level. Furthermore, the proposed approach is genuinely multiscale since it makes it possible to bridge actions on the individual cellular-based dynamics to observable patterns in the cohort of patients. In a different context, the asymptotic properties of such controls have been investigated in Tosin and Zanella [2021](#).

From the mathematical viewpoint, the introduction of such clinical uncertainties translates in an increased dimensionality of the resulting kinetic problem whose equilibrium depends on all the uncertainties introduced at the cellular level. The construction of numerical schemes for the resulting equations needs

to guarantee spectral convergence on the random field under suitable regularity assumptions together with the preservation of the main physical properties of the model, see *e.g.* Carrillo, L. Pareschi, and Zanella [2019]; Carrillo and Zanella [2019]; L. Pareschi and Zanella [2020]; Xiu [2010].

In more details, the paper is organised as follows: in Section [IV.2] we introduce the kinetic model of interest and we discuss the role of the uncertain parameters present at the level of the transition function. Hence, we briefly derive in the quasi-invariant limit reduced order models of Fokker-Planck-type from which large time distributions are explicitly computable. In Section [IV.3] we introduce a hierarchical control protocol with the aim to steer the tumour's size towards a prescribed size through the minimisation of two possible cost functionals. The emerging macroscopic properties of the introduced approach is then discussed together with their interplay with the model uncertainties. In Section [IV.4] we face the calibration of the model with real clinical data provided and in Section [IV.5] we introduce suitable numerical strategies to deal with uncertainty quantification of Boltzmann-type and Fokker-Planck-type equations.

IV.2 Kinetic modelling of tumour growth dynamics with clinical uncertainties

Let us characterise the microscopic state of an evolving tumour by means of a variable $x \in \mathbb{R}_+$ representing the volume of the tumour. Furthermore, we collect all the source of uncertainties of the dynamics in the random vector $\mathbf{z} = (z_1, \dots, z_d) \in \mathbb{R}^d$ whose distribution is $\rho(\mathbf{z})$, *i.e.*

$$\mathbb{P}[\mathbf{z} \in A] = \int_A \rho(\mathbf{z}) dz,$$

for any $A \subseteq \mathbb{R}^d$. In details, for any fixed \mathbf{z} , if $X(\mathbf{z}, t)$ is a random variable expressing the volume of the tumour, the probability density associated to $X(\mathbf{z}, t)$ is $f(\mathbf{z}, x, t)$ and $\int f(\mathbf{z}, x, t) dx$ is the fraction of tumours that, at time $t \geq 0$, are characterised by a volume between x and $x + dx$. It is worth to

mention that the knowledge of the evolution of $f(\mathbf{z}, x, t)$ allows to compute the evolution of macroscopic quantities that are given by

$$\int_{\mathbb{R}_+} \varphi(x) f(\mathbf{z}, x, t) dx,$$

where φ is a test function. We can observe that the macroscopic quantity of interest still depends on the introduced uncertainties.

In details, for a given volume $x \in \mathbb{R}_+$ of cancer cells, we characterise an elementary variation $x \rightarrow x'$ as follows

$$x' = x + \Phi_\delta^\epsilon(x/x_L, \mathbf{z})x + x\eta_\epsilon, \quad \epsilon \ll 1. \quad (\text{IV.1})$$

where Φ_δ^ϵ is a transition function taking into account variations due to environmental cues and which depends on the tumour size x and on additional clinical uncertainties expressed by the random vector $\mathbf{z} \in \mathbb{R}^d$ characterising the lack of knowledge of parameters. The quantity $x_L = x_L(\mathbf{z}) > 0$ is a characteristic patient-based tumour size, *e.g.* the carrying capacity. Furthermore, in [\(IV.1\)](#) the random variable η_ϵ takes into account unpredictable changes in the transition dynamics and such that $\langle \eta_\epsilon \rangle = 0$ and $\langle \eta_\epsilon^2 \rangle = \epsilon\sigma^2$, where $\langle \cdot \rangle$ denotes the expectation with respect to the distribution of η_ϵ . Therefore, in a single transition the tumour's size can be modified by two multiplicative mechanisms parametrised by the positive constant $\epsilon \ll 1$ and by the uncertain parameter $\delta = \delta(\mathbf{z}) \in [-1, 1]$ influencing the considered type of growth.

IV.2.1 Transition functions

The transitions characterising the proposed elementary growths should be considered arbitrary small. For this reason, coherently with Preziosi, G. Toscani, and Zanella [2021](#), we require that Φ_δ^ϵ is of order ϵ and that

$$\lim_{\epsilon \rightarrow 0^+} \frac{\Phi_\delta^\epsilon(x/x_L, \mathbf{z})}{\epsilon} = \Phi_\delta(x/x_L, \mathbf{z}).$$

Having in mind this requirement we now characterise a general transition function that is coherent with known microscopic models for tumour growth.

We consider

$$\Phi_\delta^\epsilon(y, \mathbf{z}) = \mu \frac{1 - e^{\epsilon(y^\delta - 1)/\delta}}{(1 + \lambda)e^{\epsilon(y^\delta - 1)/\delta} + 1 - \lambda}, \quad y = \frac{x}{x_L} \quad (\text{IV.2})$$

where we introduced the uncertain parameters $\mu = \mu(\mathbf{z}) \in (0, 1)$ and $\lambda = \lambda(\mathbf{z}) \in [0, 1)$ characterising birth and death rates of tumour cells in a single transition since, independently on $\epsilon \ll 1$, we have

$$-\frac{\mu}{1 + \lambda} \leq \Phi^\epsilon(x/x_L, \mathbf{z}) \leq \frac{\mu}{1 - \lambda}.$$

In absence of fluctuations, we have $x' > x$ when $x < x_L$ for all values of the parameter δ . In terms of δ , the transition function do not behave in the same way in the region $x < x_L$. As highlighted in Giacomo Dimarco and Giuseppe Toscani [2020], Preziosi, G. Toscani, and Zanella [2021], the transition function Φ_δ^ϵ with $\delta > 0$ is increasing convex for all $x \leq x_L$, whereas it is concave in an interval $[0, \bar{x}]$, $\bar{x} < x_L$ and then convex for $\delta < 0$. A compatibility condition for the elementary variations [IV.1] with the transition functions [IV.2] is that x' remains in \mathbb{R}_+ . This can be guaranteed by imposing the following sufficient condition on the fluctuation η_ϵ . In particular, by considering for any $\mathbf{z} \in \mathbb{R}^d$ a random variable such that

$$\eta_\epsilon \geq -1 + \max_{\mathbf{z} \in \mathbb{R}^d} \frac{\mu}{1 + \lambda},$$

the post-transition size x' is positive.

It is worth to remark that in the limit $\epsilon \rightarrow 0^+$ we have

$$\Phi^\epsilon(x/x_L, \mathbf{z}) \approx \epsilon \mu \frac{(y^\delta - 1)/\delta}{(1 + \lambda)\epsilon(1 - y^\delta)/\delta + 2}, \quad y = \frac{x}{x_L}$$

which implies

$$\lim_{\epsilon \rightarrow 0^+} \frac{\Phi^\epsilon(x/x_L, \mathbf{z})}{\epsilon} = \frac{\mu}{2\delta} \left(1 - \left(\frac{x}{x_L} \right)^\delta \right).$$

Therefore, the proposed transition function is coherent in the limit $\epsilon \rightarrow 0^+$ with existing models for the description of tumour growth. In particular, if we consider the following first order Bernoulli differential equation

$$\frac{d}{dt} x(\mathbf{z}, t) = \frac{\mu}{2\delta} \left(1 - \left(\frac{x(\mathbf{z}, t)}{x_L} \right)^\delta \right) x(\mathbf{z}, t), \quad (\text{IV.3})$$

in the limit $\delta \rightarrow 0$ we recover Gompertz growth dynamics since (IV.3) corresponds to

$$\frac{d}{dt}x(\mathbf{z}, t) = -\frac{\mu}{2} \log\left(\frac{x(\mathbf{z}, t)}{x_L}\right) x(\mathbf{z}, t), \quad (\text{IV.4})$$

whereas for any $\delta < 0$ we recover von Bertalanffy dynamics of the form

$$\frac{d}{dt}x(\mathbf{z}, t) = px(\mathbf{z}, t)^{\delta+1} - qx(\mathbf{z}, t), \quad (\text{IV.5})$$

with $q = q(\mathbf{z}) = -\frac{\mu}{2\delta}$, $p = p(\mathbf{z}) = -\frac{\mu}{2\delta x_L^\delta}$. It can be easily observed that for any $\delta > 0$ we recover logistic-type growth that are not of limited interest in the present context.

Remark IV.2.1. The dynamics described by (IV.3) are coherent with the expected transition scheme (IV.1). Indeed, if we introduce a forward time discretisation with time step $\Delta t > 0$ from (IV.3) we get

$$x^{n+1}(\mathbf{z}) = x^n(\mathbf{z}) + \Delta t \frac{\mu}{2\delta} \left(1 - \left(\frac{x^n(\mathbf{z})}{x_L} \right)^\delta \right) x^n(\mathbf{z}),$$

where $x^n(\mathbf{z}) = x(t^n, \mathbf{z})$ and $t^n = n\Delta t$, $n \in \mathbb{N}$. Hence, by identifying $\Delta t = \epsilon$ we can recognise the transition scheme in (IV.1).

IV.2.2 Kinetic models and equilibria

Let $f = f(\mathbf{z}, x, t)$ be the distribution function of cells of size $x \in \mathbb{R}_+$ at time $t \geq 0$ and depending on the epistemic uncertainties collected in \mathbf{z} . The evolution of f is then given by the following kinetic equation

$$\partial_t f(\mathbf{z}, x, t) = Q_G(f)(\mathbf{z}, x, t), \quad (\text{IV.6})$$

where the transition operator $Q_G(\cdot)(\mathbf{z}, x, t)$ is defined as follows

$$Q_G(f)(\mathbf{z}, x, t) = \int_{\mathbb{R}_+} \frac{1}{|J|} f(\mathbf{z}, 'x, t) dx - f(\mathbf{z}, x, t), \quad (\text{IV.7})$$

being $'x$ the pre-transition state and $'J$ is the absolute value of the Jacobian of the transformation from the pre-transition state $'x$ to the state x . The kinetic

equation (IV.6) can be fruitfully written in weak form to evaluate the evolution of observable quantities as follows

$$\frac{d}{dt} \int_{\mathbb{R}_+} \varphi(x) f(\mathbf{z}, x, t) dx = \int_{\mathbb{R}_+} \langle \varphi(x') - \varphi(x) \rangle f(\mathbf{z}, x, t) dx, \quad (\text{IV.8})$$

where φ is a smooth function. Since the computation of equilibrium distribution of (IV.6) is very hard it is convenient to resort to a surrogate model with which we can analytically obtain the large type distribution of the studied phenomenon. This approach is defined as quasi-invariant limit and it has roots in the grazing limit of kinetic theory. Several applications of this approach have been employed in recent years for the statistical description of collective phenomena, see L. Pareschi and G. Toscani [2013]; G. Toscani [2006] for an introduction. In the following we briefly recall the derivation of Fokker-Planck-type equations from (IV.6) thanks to a quasi-invariant limit technique.

We may observe that for $\epsilon \ll 1$ the difference $x' - x$ is small and we can perform the following Taylor expansion up to order three

$$\varphi(x') - \varphi(x) = (x' - x) \frac{d\varphi(x)}{dx} + \frac{1}{2} (x' - x)^2 \frac{d^2\varphi(x)}{dx^2} + \frac{1}{6} (x' - x)^3 \frac{d^3\varphi(\bar{x})}{dx^3},$$

with $\bar{x} \in (\min\{x, x'\}, \max\{x, x'\})$. Since $x' - x = \Phi_\delta^\epsilon(x/x_L, \mathbf{z}) + x\eta_\epsilon$ we can plug this expression in (IV.8) to obtain

$$\begin{aligned} \frac{d}{dt} \int_{\mathbb{R}_+} \varphi(x) f(\mathbf{z}, x, t) dx &= \int_{\mathbb{R}_+} \frac{\Phi_\delta^\epsilon(x/x_L, \mathbf{z})}{\epsilon} x f(\mathbf{z}, x, t) \frac{d\varphi(x)}{dx} dx \\ &\quad + \frac{\sigma^2}{2} \int_{\mathbb{R}_+} x^2 f(\mathbf{z}, x, t) \frac{d^2\varphi(x)}{dx^2} dx + R_\varphi(f)(\mathbf{z}, x, t), \end{aligned} \quad (\text{IV.9})$$

where we have exploited the fact that $\langle \eta_\epsilon \rangle = 0$ and we have defined the rest $R_\varphi(f)(\mathbf{z}, x, t)$ as

$$\begin{aligned} R_\varphi(f)(\mathbf{z}, x, t) &:= \frac{1}{2} \int_{\mathbb{R}_+} \frac{(\Phi_\delta^\epsilon(x/x_L, \mathbf{z}))^2}{\epsilon} x^2 f(\mathbf{z}, x, t) \frac{d^2\varphi(x)}{dx^2} dx \\ &\quad + \frac{1}{6} \int_{\mathbb{R}_+} \frac{\langle \Phi_\delta^\epsilon(x/x_L, \mathbf{z}) x + x\eta_\epsilon \rangle^3}{\epsilon} f(\mathbf{z}, x, t) \frac{d^3\varphi(x)}{dx^3} dx. \end{aligned}$$

Assuming that the third order moment of η_ϵ is bounded, *i.e.* $\langle |\eta_\epsilon|^3 \rangle < +\infty$, thanks to the smoothness of φ we have

$$|R_\varphi(f)(x, t, \mathbf{z})| \lesssim \epsilon + \epsilon^2 + \epsilon + \sqrt{\epsilon},$$

where we use the notation $a \lesssim b$ to mean that there exists a constant $K > 0$ such that $a \leq Kb$. Hence, in the limit $\epsilon \rightarrow 0^+$ we have $|R_\varphi(f)(\mathbf{z}, x, t)| \rightarrow 0$, for every $x \in \mathbb{R}_+$, $t > 0$ and $\mathbf{z} \in \mathbb{R}^d$. As a consequence, if we introduce the new time scale $\tau = \epsilon t$, for $\epsilon \ll 1$, such that $f(\mathbf{z}, x, \tau) = f(\mathbf{z}, x, \tau/\epsilon)$ and we observe that $\frac{d}{dt} = \epsilon \frac{d}{d\tau}$, the model defined in (IV.9) for $\epsilon \rightarrow 0^+$ converges to

$$\begin{aligned} \frac{d}{d\tau} \int_{\mathbb{R}_+} \varphi(x) f(\mathbf{z}, x, \tau) dx &= \int_{\mathbb{R}_+} \Phi_\delta(x/x_L, \mathbf{z}) x f(\mathbf{z}, x, \tau) \frac{d\varphi(x)}{dx} dx \\ &\quad + \frac{\sigma^2}{2} \int_{\mathbb{R}_+} x^2 f(\mathbf{z}, x, \tau) \frac{d^2\varphi(x)}{dx^2} dx, \end{aligned}$$

where

$$\Phi_\delta(x/x_L, \mathbf{z}) = \frac{\mu}{2\delta} \left(1 - \left(\frac{x}{x_L} \right)^\delta \right). \quad (\text{IV.10})$$

Hence, integrating back by parts we obtain the following Fokker-Planck-type equation with uncertainties

$$\partial_\tau f(\mathbf{z}, x, \tau) = \partial_x \left[-\Phi_\delta(x/x_L, \mathbf{z}) x f(\mathbf{z}, x, \tau) + \frac{\sigma^2}{2} \partial_x (x^2 f(\mathbf{z}, x, \tau)) \right]. \quad (\text{IV.11})$$

provided that for all $\tau \geq 0$ the density $f(\mathbf{z}, x, \tau)$ satisfies the following no-flux boundary condition

$$-\Phi_\delta(x/x_L, \mathbf{z}) x f(\mathbf{z}, x, \tau) + \frac{\sigma^2}{2} \partial_x (x^2 f(\mathbf{z}, x, \tau)) \Big|_{x=0} = 0. \quad (\text{IV.12})$$

Thanks to the obtained surrogate model we can study the large time behaviour of the system. In particular, the model (IV.11) with no-flux boundary condition (IV.12) admits a unique equilibrium distribution $f^\infty(\mathbf{z}, x)$ that is solution to

$$-\Phi_\delta(x/x_L, \mathbf{z}) x f^\infty(\mathbf{z}, x) + \frac{\sigma^2}{2} \partial_x (x^2 f^\infty(\mathbf{z}, x)) = 0.$$

see Risken [1996]. In view of (IV.10) we have

$$f^\infty(\mathbf{z}, x) = C_{\mu, \sigma^2, x_L}(\mathbf{z}) \left(\frac{x}{x_L} \right)^{\frac{\mu}{\sigma^2 \delta} - 2} \exp \left\{ -\frac{\mu}{\sigma^2 \delta} \left(\left(\frac{x}{x_L} \right)^\delta - 1 \right) \right\}, \quad (\text{IV.13})$$

with $C_{\mu, \sigma^2, x_L} > 0$ a normalisation constant.

In particular, we highlight that the two reference microscopic models we consider, corresponding to the choices $\delta < 0$ and $\delta \rightarrow 0$, generate slight different equilibria. In particular, the Gompertzian growths, obtained in the limit $\delta \rightarrow 0$, generates at the equilibrium the lognormal distribution

$$f^\infty(\mathbf{z}, x) = \frac{1}{\sqrt{2\gamma\pi x}} \exp\left\{-\frac{(\log x - k)}{2\gamma}\right\},$$

with $\gamma = \gamma(\mathbf{z}) = \sigma^2/\mu(\mathbf{z})$ and $k = k(\mathbf{z}) = \log x_L(\mathbf{z}) - \gamma(\mathbf{z})$. This distribution is characterised by slim tails with exponential decay. On the contrary, von Bertalanffy-type growths, obtained from (IV.2) with $-1 \leq \delta(\mathbf{z}) < 0$, are associated to Amoroso-type distributions

$$f^\infty(\mathbf{z}, x) = \frac{|\delta|}{\Gamma(k/|\delta|)} \frac{\theta^k}{x^{k+1}} \exp\left\{-\left(\frac{\theta}{x}\right)^{|\delta|}\right\},$$

$$k(\mathbf{z}) = \frac{1}{\gamma|\delta|} + 1, \quad \theta(\mathbf{z}) = x_L(\mathbf{z}) \left(\frac{1}{\gamma\delta^2}\right)^{1/|\delta|},$$

where again $\gamma = \gamma(\mathbf{z}) = \sigma^2/\mu(\mathbf{z})$. It is important to remark that the emerging equilibrium distribution in the case $\delta < 0$ exhibits fat tails with polynomial decay. From a phenomenological point of view this is a substantial difference, since fat-tailed distributions are associated to a higher probability that the tumour is large. We point the interested reader to Preziosi, G. Toscani, and Zanella (2021) for more details.

IV.3 Observable effect of therapeutic protocols

In the following, we interface the natural growth mechanisms under clinical uncertainties with a superimposed therapeutical protocol that seeks to steer tumours' size towards a prescribed target. Hence, at each transitions, the tumours' size is influenced by two competing dynamics, the first characterised by the uncertain growth, and the second by therapeutical protocols. In details, to determine measurable effects of therapies on growth dynamics, we include a deterministic external action as an instantaneous correction of the microscopic

interaction. In details, we distinguish two types of volume updates acting on the tumour growth:

- i) the first is based on the transition law discussed in (IV.1)
- ii) the second is the therapy that acts in reducing the volume of the tumour

$$x'' = x + \epsilon S(x)u, \quad (\text{IV.14})$$

where $u \in \mathcal{U}$, where \mathcal{U} is the set of admissible controls such that $x'' \geq 0$ and u is a control defined such that

$$u = \arg \min_{u \in \mathcal{U}} J(x'', u), \quad (\text{IV.15})$$

subject to the constraint (IV.14). We consider also a cost function of the form

$$J(x'', u) = (x'' - x_d)^2 + \nu |u|^p, \quad (\text{IV.16})$$

with $\nu > 0$ a penalisation coefficient and $x_d > 0$ the desired tumours' size reachable with the implemented therapeutical protocol. The function $S(\cdot)$ acts selectively with respect to the tumour size.

In the introduced framework, we highlight that the control obtained from (IV.15) subject to (IV.14) is independent on \mathbf{z} . Furthermore, it is worth to remark that the typical choices for the cost function (IV.16) are obtained for $p = 1, 2$. More general convex functions may be considered leading often to problems that are not analytically treatable. Furthermore, in the following we will concentrate on three possible selective functions $S(x) = 1, \sqrt{x}$.

The kinetic equation expressing the control strategy defined in (IV.1) and in (IV.14) is as a sum of transition operators

$$\partial_t f(\mathbf{z}, x, t) = Q_G(f)(\mathbf{z}, x, t) + Q_C(\mathbf{z}, x, t), \quad (\text{IV.17})$$

where $Q_G(\cdot)$ has been defined in (IV.7) and the influence of therapeutical protocols on the dynamics is expressed by the new operator $Q_C(\cdot)$ whose strong formulation is given by

$$Q_C(f)(\mathbf{z}, x, t) = \int_{\mathbb{R}^+} \frac{1}{J} f(\mathbf{z}, x'', t) dx'' - f(\mathbf{z}, x, t), \quad (\text{IV.18})$$

with $''J$ the the absolute value of the Jacobian of the transformation from $''x$ to x . Under suitable hypotheses is possible to obtain explicit formulation of the operator $Q_C(\cdot)$ by solving the control problem (IV.15) in feedback form at the cellular level. As before equation (IV.17) can be fruitfully rewritten in weak form

$$\frac{d}{dt} \int_{\mathbb{R}_+} \varphi(x) f(\mathbf{z}, x, t) dx = \int_{\mathbb{R}_+} \langle \varphi(x') - \varphi(x) \rangle f(\mathbf{z}, x, t) dx + \int_{\mathbb{R}_+} (\varphi(x'') - \varphi(x)) f(\mathbf{z}, x, t) dx. \quad (\text{IV.19})$$

The evolution of macroscopic quantities in the constrained setting is determined by suitable choices of the test function φ . In the following we will consider two main cases based on the minimisation of the cost (IV.16) with $p = 1, 2$.

IV.3.1 The case $p = 2$

Let us consider $p = 2$ in the cost function (IV.16). The minimisation of (IV.15) can be classically done by resorting to a Lagrangian multiplier approach. We recall for related approaches the works Albi, Herty, and L. Pareschi [2015] Albi, L. Pareschi, and Zanella [2014]. We consider the Lagrangian

$$\mathcal{L}(u, x'') = J(x'', u) + \alpha[x'' - x - \epsilon S(x)u], \quad (\text{IV.20})$$

where $\alpha \in \mathbb{R}$ is the Lagrange multiplier associated to the constraint (IV.14). Hence, the optimality conditions are the following

$$\begin{cases} \frac{\partial}{\partial u} \mathcal{L}(x'', u) = 2\nu u - \alpha \epsilon S(x) = 0 \\ \frac{\partial}{\partial x''} \mathcal{L}(x'', u) = 2(x'' - x_d) + \alpha = 0, \end{cases}$$

whence we find the optimal value

$$u^* = -S(x) \frac{\epsilon}{\epsilon^2 S^2(x) + \nu} (x - x_d). \quad (\text{IV.21})$$

Therefore, plugging the optimal control (IV.21) defined at the cellular level into (IV.15), we obtain the controlled transition

$$x'' = x - \frac{\epsilon^2 S^2(x)}{\epsilon^2 S^2(x) + \nu} (x - x_d).$$

In this way we can study the evolution of the kinetic distribution function solution of (IV.17)-(IV.18) through standard methods of kinetic theory. In details, we will study the evolution of observable quantities in presence of uncertain quantities. The interplay of the introduced control with epistemic uncertainties is of paramount importance to define robust protocols.

IV.3.1.1 Main properties

We define the first order moment $m(\mathbf{z}, t)$ and the second order moment $E(\mathbf{z}, t)$, or energy, respectively as

$$m(\mathbf{z}, t) = \int_{\mathbb{R}_+} x f(\mathbf{z}, x, t) dx$$

$$E(\mathbf{z}, t) = \int_{\mathbb{R}_+} x^2 f(\mathbf{z}, x, t) dx,$$

whose evolutions are obtained by considering $\varphi(x) = x, x^2$ in (IV.19).

A convenient insight on the evolution of the first order moment $m(\mathbf{z}, t)$ can be obtained by scaling $\nu = \epsilon\kappa, \kappa > 0$. Under the introduced hypotheses we get

$$\begin{aligned} \frac{d}{dt} m(\mathbf{z}, t) = \frac{1}{\epsilon} \left\langle \int_{\mathbb{R}_+} (\Phi_\delta^\epsilon(x/x_L, \mathbf{z})x + x\eta_\epsilon) f(\mathbf{z}, x, t) dx \right\rangle \\ - \int_{\mathbb{R}_+} \frac{S^2(x)}{\epsilon S^2(x) + \kappa} (x - x_d) f(\mathbf{z}, x, t) dx. \end{aligned}$$

Therefore, in the time-scale $\tau = \epsilon t$, by indicating $m(\mathbf{z}, \tau) = m(\mathbf{z}, t/\epsilon)$, we get in the limit $\epsilon \rightarrow 0^+$

$$\frac{d}{d\tau} m(\mathbf{z}, \tau) = \int_{\mathbb{R}_+} \Phi_\delta(x/x_L, \mathbf{z}) x f(\mathbf{z}, x, \tau) dx - \int_{\mathbb{R}_+} \frac{S^2(x)}{\kappa} (x - x_d) f(\mathbf{z}, x, \tau) dx.$$

Arguing as before for the energy $E(\mathbf{z}, t)$ in the case of zero diffusion, *i.e.*, with $\eta_\epsilon \equiv 0$ in (IV.1), we obtain

$$\frac{d}{d\tau} E(\mathbf{z}, \tau) = \int_{\mathbb{R}_+} \Phi_\delta(x/x_L, \mathbf{z}) x^2 f(\mathbf{z}, x, \tau) dx - \int_{\mathbb{R}_+} \frac{S^2(x)}{\kappa} x(x - x_d) f(\mathbf{z}, x, \tau) dx.$$

Assuming $f(\mathbf{z}, x, t) \in L^1(\mathbb{R}_+)$ it is possible to show that the model (IV.19) has an unique equilibrium distribution $f^\infty(\mathbf{z}, x)$, we point the interested reader

to L. Pareschi and G. Toscani [2013](#) (Proposition 2.1). Hence, under the introduced regularity assumption, we can obtain some information on the large time behaviour of the first and second order moment, corresponding to the quantities $m^\infty(\mathbf{z})$ and $E^\infty(\mathbf{z})$. In the following we discuss the effect of the introduced control by considering different selective functions:

a) if $S(x) = 1$ the asymptotic mean is solution of the following identity

$$\int_{\mathbb{R}_+} \Phi_\delta(x/x_L, \mathbf{z}) x f^\infty(\mathbf{z}, t) dx = \frac{1}{\kappa} (m^\infty(\mathbf{z}) - x_d).$$

Note that since Φ_δ is bounded for all $\mathbf{z} \in \mathbb{R}^d$ by the following uncertain quantities

$$-\frac{\mu}{1+\lambda} \leq \Phi_\delta \leq \frac{\mu}{1-\lambda}$$

we have

$$\left| \int_{\mathbb{R}_+} \Phi_\delta(x/x_L, \mathbf{z}) x f^\infty(\mathbf{z}, t) dx \right| \leq \int_{\mathbb{R}_+} |\Phi_\delta(x/x_L, \mathbf{z})| x f^\infty(\mathbf{z}, t) dx \leq \frac{\mu}{1-\lambda} m^\infty(\mathbf{z}). \quad (\text{IV.22})$$

Hence, the following inequality holds

$$\frac{1}{\kappa} |m^\infty(\mathbf{z}) - x_d| \leq \frac{\mu}{1-\lambda} m^\infty(\mathbf{z}),$$

whose solution is such that

$$\frac{1-\lambda}{1-\lambda+\kappa\mu} x_d \leq m^\infty(\mathbf{z}) \leq \frac{1-\lambda}{1-\lambda-\kappa\mu} x_d$$

provided $\kappa < \min_{\mathbf{z} \in \mathbb{R}^d} \frac{1-\lambda}{\mu}$. We easily observe that in the limit $\kappa \rightarrow 0^+$ corresponding to vanishing penalisation of the control the large time mean size is such that $m^\infty(\mathbf{z}) \rightarrow x_d$. In other words, we have

$$-\frac{\kappa\mu}{1-\lambda+\kappa\mu} x_d \leq m^\infty(\mathbf{z}) - x_d \leq \frac{\kappa\mu}{1-\lambda-\kappa\mu} x_d,$$

and

$$|m^\infty(\mathbf{z}) - x_d| \leq \frac{\kappa\mu}{1-\lambda-\kappa\mu} x_d. \quad (\text{IV.23})$$

Let us assume that $\sigma^2 = 0$. Then, the second order moment is such that

$$\int_{\mathbb{R}_+} \Phi_\delta(x/x_L, \mathbf{z}) x^2 f^\infty(\mathbf{z}, t) dx = \frac{1}{\kappa} (E^\infty(\mathbf{z}) - m^\infty(\mathbf{z}) x_d).$$

We note that

$$\left| \int_{\mathbb{R}_+} \Phi_\delta(x/x_L, \mathbf{z}) x^2 f^\infty(\mathbf{z}, t) dx \right| \leq \int_{\mathbb{R}_+} |\Phi_\delta(x/x_L, \mathbf{z})| x^2 f^\infty(\mathbf{z}, t) dx \leq \frac{\mu}{1-\lambda} E^\infty(\mathbf{z}),$$

since Φ_δ is bounded for all $\mathbf{z} \in \mathbb{R}^d$, as we observed before. Consequently, we have

$$E^\infty(\mathbf{z}) - m^\infty(\mathbf{z}) x_d \leq \frac{\kappa \mu}{1-\lambda} E^\infty(\mathbf{z}),$$

that is

$$E^\infty(\mathbf{z}) \left(1 - \frac{\kappa \mu}{1-\lambda} \right) \leq m^\infty(\mathbf{z}) x_d.$$

Since in the limit $\kappa \rightarrow 0^+$ we have observed that $m^\infty(\mathbf{z}) \rightarrow x_d$ we can write

$$E^\infty(\mathbf{z}) - (m^\infty(\mathbf{z}))^2 \leq 0.$$

We observe also that $E^\infty(\mathbf{z}) - (m^\infty(\mathbf{z}))^2 \geq 0$ by definition, since it is the variance of the random variable $X \sim f^\infty(\mathbf{z}, x)$. In other words, in the limit $\kappa \rightarrow 0^+$ we have $\text{Var}_{f^\infty}[X] \rightarrow 0$, that is, the equilibrium distribution tends to a Dirac delta centred in $x = x_d$.

- b) We consider now the case $S(x) = \sqrt{x}$ corresponding to a heavier control on large sized tumours. We can observe that in this case the asymptotic first order moment solves

$$\int_{\mathbb{R}_+} \Phi_\delta(x/x_L, \mathbf{z}) x f^\infty(\mathbf{z}, x) dx = \frac{1}{\kappa} \int_{\mathbb{R}_+} x(x - x_d) f^\infty(\mathbf{z}, x) dx.$$

In details, since from the Jensen's inequality we have

$$\int_{\mathbb{R}_+} (x - x_d)^2 f^\infty(\mathbf{z}, x) dx \geq \left(\int_{\mathbb{R}_+} (x - x_d) f^\infty(\mathbf{z}, x) dx \right)^2.$$

we get

$$\frac{1}{\kappa} m^\infty(\mathbf{z}) (m^\infty(\mathbf{z}) - x_d) \leq \int_{\mathbb{R}_+} \Phi_\delta(x/x_L, \mathbf{z}) x f^\infty(\mathbf{z}, x) dx.$$

Therefore, thanks to (IV.22) we obtain

$$|m^\infty(\mathbf{z}) - x_d| \leq \frac{\mu\kappa}{1-\lambda}. \quad (\text{IV.24})$$

As obtained in point (a) we obtain that for vanishing penalisation $\kappa \rightarrow 0^+$ the asymptotic first order moment is such that $m^\infty(\mathbf{z}) \rightarrow x_d$.

Assuming now that $\sigma^2 = 0$ the asymptotic energy solves

$$\int_{\mathbb{R}_+} \Phi_\delta(x/x_L, \mathbf{z}) x^2 f^\infty(\mathbf{z}, x) dx = \frac{1}{\kappa} \int_{\mathbb{R}_+} x^2 (x - x_d) f^\infty(\mathbf{z}, x) dx,$$

from which we get

$$|(m^\infty(\mathbf{z}))^3 - x_d E^\infty(\mathbf{z})| \leq \frac{\mu\kappa}{1-\lambda} E^\infty(\mathbf{z}),$$

and in the limit $\kappa \rightarrow 0^+$ we obtain that the large time distribution tends to a Dirac delta centred in $x = x_d$.

In both the discussed cases and in particular from (IV.23) and (IV.24), we can observe that the introduced protocols induce the mean tumours' sizes to stick the deterministic target size x_d . These results have an important consequence on the uncertainties of the system. In particular, looking at the variance with respect to $\mathbf{z} \in \mathbb{R}^d$ we have

$$\text{Var}_{\mathbf{z}}(m^\infty(\mathbf{z})) = \text{Var}_{\mathbf{z}}(m^\infty(\mathbf{z}) - x_d) = \mathbb{E}_{\mathbf{z}}[(m^\infty(\mathbf{z}) - x_d)^2] - \mathbb{E}_{\mathbf{z}}[(m^\infty(\mathbf{z}) - x_d)]^2,$$

from which we get

$$\text{Var}_{\mathbf{z}}(m^\infty(\mathbf{z})) \leq \mathbb{E}_{\mathbf{z}}[(m^\infty(\mathbf{z}) - x_d)^2] \leq \max \left\{ \frac{\kappa\mu}{1-\lambda-\kappa\mu} x_d, \frac{\mu\kappa}{1-\lambda} \right\}. \quad (\text{IV.25})$$

Hence, since $\max \left\{ \frac{\kappa\mu}{1-\lambda-\kappa\mu} x_d, \frac{\mu\kappa}{1-\lambda} \right\} \rightarrow 0$ for $\kappa \rightarrow 0^+$, we argue that the introduced controls are capable to dampen invariably the variability due to the presence of clinical uncertainties $\mathbf{z} \in \mathbb{R}^d$.

IV.3.1.2 Large time behaviour of the controlled model

At this point, proceeding as in Section (IV.2.2) for the new kinetic model (IV.17) we can assess the effects of the control therapies on the emerging kinetic

distribution. In the limit $\epsilon \rightarrow 0^+$ and scaling $\nu = \epsilon\kappa$, where $\kappa > 0$ is the scaled penalisation, the kinetic equation converges to a Fokker-Planck equation with modified drift term that takes into account the presence of the control. The resulting Fokker-Planck-type equation reads

$$\begin{aligned} \partial_t f(\mathbf{z}, x, t) = \partial_x \left[-\Phi_\delta(x/x_L, \mathbf{z}) x f(\mathbf{z}, x, t) + \frac{\sigma^2}{2} \partial_x (x^2 f(\mathbf{z}, x, t)) \right] \\ + \frac{1}{\kappa} \partial_x [S^2(x)(x - x_d) f(\mathbf{z}, x, t)]. \end{aligned} \quad (\text{IV.26})$$

Since we have obtained in Section [IV.2.2](#) that if $\delta < 0$ the introduced model lead to equilibrium distributions with polynomial tails, linked to a high probability that the tumours' sizes are large, we concentrate on this case. Under this assumption, the asymptotic large time distribution of the controlled model is given by

$$f^\infty(\mathbf{z}, x) = C_{\mu, \sigma^2, x_L}(\mathbf{z}) \left(\frac{1}{x}\right)^{\frac{1}{\gamma|\delta|} + 2} \exp\left\{-\frac{2}{\sigma^2 \delta^2} \left(\frac{x}{x_L}\right)^\delta\right\} \exp\left\{-\frac{2}{\sigma^2 \kappa} \int \frac{S^2(x)(x - x_d)}{x^2} dx\right\},$$

with $C_{\mu, \sigma^2, x_L} > 0$ a normalisation constant. Hence, if $S(x) = 1$ a direct computation gives

$$f^\infty(\mathbf{z}, x) = C_{\mu, \sigma^2, x_L}(\mathbf{z}) \left(\frac{1}{x}\right)^{\frac{1}{\gamma|\delta|} + \frac{2}{\sigma^2 \kappa} + 2} \exp\left\{-\frac{2}{\sigma^2 \delta^2} \left(\frac{x}{x_L}\right)^\delta\right\} \exp\left\{-\frac{2x_d}{\sigma^2 \kappa} \frac{1}{x}\right\},$$

and the emerging equilibrium of the controlled exhibits again power law tails for large x 's. Anyway, it is worth to observe that the exponent increases due to the presence of the introduced control. On the other hand, for selective controls with $S(x) = \sqrt{x}$ we get

$$f^\infty(\mathbf{z}, x) = C_{\mu, \sigma^2, x_L}(\mathbf{z}) \left(\frac{1}{x}\right)^{\frac{1}{\gamma|\delta|} - \frac{2x_d}{\sigma^2 \kappa} + 2} \exp\left\{-\frac{2}{\sigma^2 \delta^2} \left(\frac{x}{x_L}\right)^\delta\right\} \exp\left\{-\frac{2}{\sigma^2 \kappa} x\right\},$$

provided $\kappa > 2x_d\gamma|\delta|/\sigma^2$, corresponding to a distribution with exponential decay of the tail. In other words, even if the introduced therapies are capable to reduce in any case the influence of clinical uncertainties, selective-type controls, whose action is heavier on large tumours, are necessary to modify the nature of the emerging distribution of tumours' sizes.

IV.3.2 The case $p = 1$

Let us consider $p = 1$ in (IV.16). Proceeding as before we consider the Lagrangian (IV.20) with the cost function $J(x'', u) = (x'' - x_d)^2 + \nu|u|$. The optimality conditions read now

$$\begin{cases} \frac{\partial}{\partial u} \mathcal{L}(x'', u) = \nu \operatorname{sign}(u) - \alpha \epsilon S(x) = 0 \\ \frac{\partial}{\partial x''} \mathcal{L}(x'', u) = 2(x'' - x_d) + \alpha = 0. \end{cases}$$

A direct solution of the previous system leads, as before, to a feedback formulation of the optimal control that can be written as follows

$$u^* = \Pi_U (\mathbb{S}^1(x - x_d)),$$

where the operator $\mathbb{S}^1(x - x_d)$ is defined as

$$\mathbb{S}^1(x - x_d) := \begin{cases} \frac{x - x_d}{|x - x_d|} \frac{\nu}{2\epsilon^2 S^2(x)} - \frac{x - x_d}{\epsilon S(x)}, & |x - x_d| > \frac{\nu}{2\epsilon S(x)}, \\ 0 & \text{otherwise} \end{cases}$$

and Π_U is the projection onto a compact subset $U \subset \mathbb{R}$. It should be noted that for any value of $\epsilon > 0$ the applied control is active only on a portion of tumours. This result is coherent with analogous works in related fields, see Albi, Fornasier, and Kalise. [2016] During, L. Pareschi, and G. Toscani [2018]

In this scenario, it is not possible to apply the same arguments of Section IV.3.1.2 to get analytical results on the evolution of observable quantities. Furthermore, the derivation of surrogate Fokker-Planck-type models does not help to obtain insights on the large time behaviour of the system. As a consequence, in the following we will focus on the consistent numerical approaches to have a qualitative indication of the emerging phenomena.

IV.4 Quantities of interest and data

In this section, we face the calibration of the kinetic model (IV.6) defined in Section IV.2.2 in presence of uncertain quantities by means of experimental

data. In particular, to obtain some evidence on the distribution of uncertain quantities, we focus on the microscopic laws defined in (IV.1) to get a patient-based estimation of all the relevant parameters characterising the dynamics. Thus, to deal with the uncertainties brought by the parameter \mathbf{z} and affecting the evolution of the distribution $f(\mathbf{z}, x, t)$, we consider as a quantity of interest (QoI) the expected evolution of the first order moment $\mathbb{E}_{\mathbf{z}}[m(\mathbf{z}, t)]$. In this way, we are able to compare the theoretical and numerical results with the measures of our dataset relative to the cohort of subjects affected by glioblastoma. Empirical measurements of a subject's tumour sizes correspond to a specific realisation of a particular value of the random variable \mathbf{z} . Therefore, the average behaviour of a glioblastoma is the result of the superposition of different dynamics, produced by different values of \mathbf{z} , incorporating the subjects' variability, that are then weighted by the associated probability measure $\rho(\mathbf{z})$.

In particular, we are interested in the analytical and numerical solutions obtained for $\delta \rightarrow 0$ and for $\delta < 0$, reproducing Gompertz and von Bertalanffy growth models respectively. Parameter estimation in tumour growth dynamics is a classical problem and we mention A. K. Laird [1965]; A. Laird [1964] for an introduction on the topic. More recently a similar problem has been considered for glioblastoma in Ma et al. [2020].

IV.4.1 Dataset construction and Segmentation

In this work, we consider clinical data for tumour growth relative to a cohort of patients referred to IRCCS Mondino, collected from 2011 to 2021. Among 263 subjects suffering from brain tumour, we select those affected by primary glioblastoma. In all these cases MRI (Magnetic Resonance Imaging) scans were available after each visit. Combining the neuro-radiological and the clinical information, we choose among the selected patients the ones who exhibit an initial tumour free-growth and that have at least two MRI scans at different times. In this way, we are capable to estimate the patient-based growth dynamics. Anyway, only very few observations can be obtained of these

characteristics since the great majority of patients are enrolled for follow-up at Mondino after initial treatments. For these reasons, we include subjects with treatments' interruption. At the end of this preliminary analysis, we considered the evolution of the tumours' size of 13 patients.

Among the patients' MRI sequences, typical of the MRI brain tumour acquisition protocol, we are interested in the T1 weighted 3D MRI scans with contrast agent to estimate the subjects' tumour volume x in mm^3 at a given time. The T1-weighted MRI images rely upon longitudinal relaxation of the tissue's magnetisation vector due to the protons spin-lattice interactions. Different tissue types are characterised by different T1 relaxation times, therefore it is possible to differentiate anatomical structures. An injection of a contrast agent, such as gadolinium, during the T1- weighted image acquisition, supplies information about current disease activity. In fact, passing through the blood brain barrier, the contrast agent reveals inflammation areas that appear brighter, helping in identifying the tumours' contours.

For each subject, the glioblastoma volume segmentation is performed using the software 3D slicer (Fedorov et al. [2012](#)). We combine a data clustering algorithm and manual segmentation corrections. In particular, we apply the region growing algorithm based on the examination of neighbouring pixels of the initial seeds, a set of selected points in the region of interest, determining whether a neighbour pixel should be added to that region or not. After that, a manual correction of contours is performed. The procedure is iterated in the axial, coronal and sagittal image projection in order to obtain more precise results. To determine the tumours' volume, the number of voxels contained in the segmentation and the MRI metadata information have been considered.

IV.4.2 Growth curves and growth model parameters' distributions

To determine the empirical distribution of the parameters characterising the tumours' dynamics we adopted a two-level approach. In particular, in the phase

preceding therapies, we estimated the parameters characterising the growth for each patient. This estimation will be then kept to evaluate the observable effects of the treatment. In more details, for a cohort of N patients we define $\{\hat{x}_i(t^n)\}_{i=1}^N$ the observed volume size at time t^n .

Assuming Gompertz-type growths we need to estimate a 2D vector for each patient, *i.e.* the tumour growth rate $\alpha > 0$ and the carrying capacity $x_L > 0$. We indicate with $\Theta = (\alpha, x_L)$ the 2D vectors of parameters. Hence, in the time interval $[0, T]$ we solve a least square problem based on the minimisation of a suitable norm of theoretical and empirical tumour's sizes measured at the available times $t^0, \dots, t^n \leq T$. More precisely, we considered a minimisation problem based on the following norm

$$\min_{\Theta} \left[\sum_{h \in H_i} |x(t^h) - \hat{x}(t^h)| + \beta \|\Theta\|_{L^1} \right], \quad (\text{IV.27})$$

where H_i collects all the observations of the tumour's volume of the i th subject. Furthermore, we introduced the regularisation parameter $\beta > 0$. In the case $\delta \rightarrow 0^+$ we considered the theoretical evolution for x given by [\(IV.4\)](#).

For von Bertalanffy-type dynamics we have to estimate a 3D vector for each patient $\Theta = (a, p, q)$, with $a = \delta + 1$, as observed in Section [IV.2.1](#). Furthermore, information on the carrying capacity x_L has been considered compatible with the Gompertz case. In the time interval $[0, T]$ we solved a least square problem [\(IV.27\)](#) where the theoretical evolutions of the tumours' volumes are given by [\(IV.5\)](#).

Since the first MRI time point t_0 and tumour size x_0 are different for each subject, we need to find a common point with the aim of comparing the patient specific growth curves for both models. As initial volume, we take the tumour size 1mm^3 as the mentioned point. This choice is justified by the fact that the smallest appreciable MRI voxel dimension is 1mm^3 . Hence, we solve through standard numerical methods [IV.3](#) to obtain, for each subject, the specific time corresponding to 1mm^3 . Subsequently, we translate for each subject the initial time of the estimated time. The obtained growth curves and empirical volume

size data are shown for each subject and for Gompertz and von Bertalanffy models in Figure [IV.1](#).¹

To understand the trends of the aforementioned model parameters, incorporated in the random variable \mathbf{z} , we construct the associated histograms and we determine the theoretical distributions that better reproduce each of them in the associated range of variability. The results are shown in the Fig. [IV.2](#). We obtained a poor fit of the parameter α characterising Gompertz-type growths and we decided to consider an uninformative uniform distribution over the observed interval of variability [0.001, 0.03]. Anyway, we observe that the range of α is consistent with values reported in Ma et al. [2020](#) and obtained from a global fit on a larger subjects data cohort.

The parameters of the theoretical distributions are obtained by maximising the proper likelihood function. To verify the goodness of the theoretical representations, we quantify the distance between each distribution function of the empirical sample and the cumulative distribution function of the selected theoretical one by performing the Kolmogorov-Smirnov test. The results are summarised in Table [IV.1](#).

All other parameters, as can be seen from Table [IV.1](#), are instead well described by a Beta distribution defined by

$$f(x, c_1, c_2) = \frac{\Gamma(c_1 + c_2)x^{c_1-1}(1-x)^{c_2-1}}{\Gamma(c_1)\Gamma(c_2)}$$

with c_1 and c_2 the shape parameters that have been reported in the third column of Table [IV.1](#).

¹From Figure [IV.1](#) it seems that different clusters of fast-growing tumors, less-fast-growing tumors and more- slowly-growing ones can be found. However, the available clinical data about glioblastoma and patient characteristics (age, survival outcome, therapeutic protocol, received Dose (Gy), chemotherapy drugs or type of alkylating agent used) do not allow a precise identification of patterns or significant features to distinguish those clusters. According to Han et al. [2020](#) the analysis of genetic mutations, in particular IDH mutant neomorphic activity “*establishes distinctive patterns in cancer metabolism, epigenetic shift and therapy resistance.*” The available clinical data report the IDH mutation (wild type) information for 3 of 13 patients. As a future perspective we aim to collect a statistically significant group of glioblastoma data coupled with genetic analysis of biopsies in order to apply the developed model and to investigate if we find effectively the clusters that seem to emerge in Figure [IV.1](#) and if they can be distinguished according to genetic mutations or clinical characteristics.

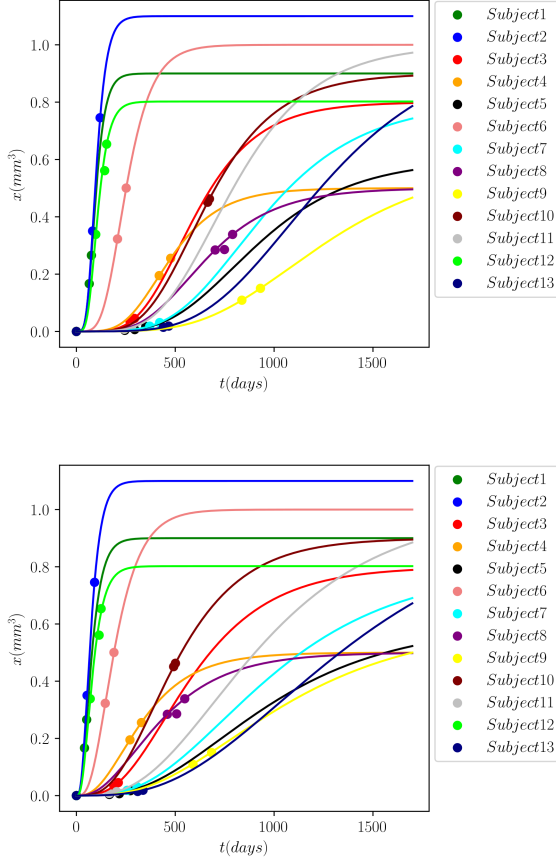


Figure IV.1: Growth curves and empirical data relative to untreated glioblastoma. The trajectory of each curve (solid line) and the empirical volume size (circle marker) data are shown for each patient and for different growth laws: Gompertz case (left plot), von Bertalanffy case (right plot). Values reported on y-axes are scaled by a quantity of 10^5 .

Parameter	Range	Distribution	Constants (c_1, c_2)	KS-pvalue
x_L	[0.4, 1.1]	Beta	(0.705, 0.574)	0.823
a	[0.69, 0.8]	Beta	(0.656, 0.193)	0.902
q	[0.007, 0.12]	Beta	(0.112, 0.238)	0.314

Table IV.1: We report for each parameter the best fitted Beta distribution characterised by the constants (c_1, c_2) in the third column and the range of definition in the second column (the x_L range is scaled by a quantity of 10^5). The quantification of the goodness of the theoretical representations is given by KS-pvalue in the last column.

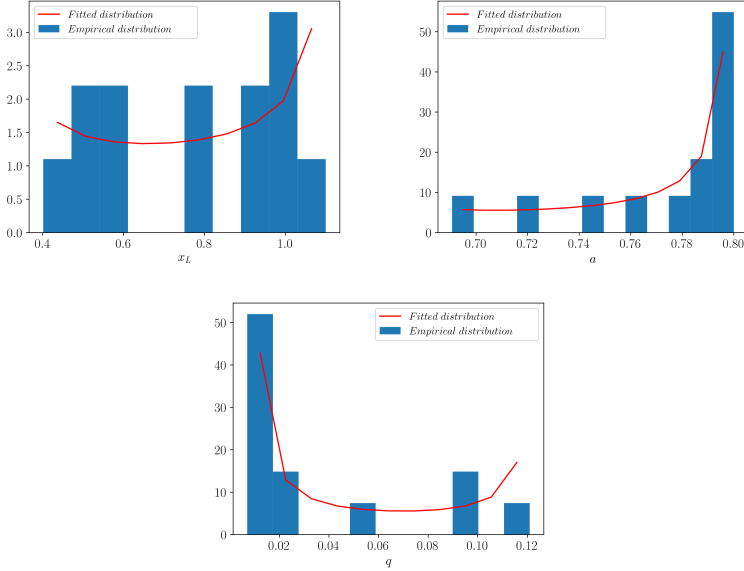


Figure IV.2: Empirical distributions of the obtained parameters and fitted Beta distributions with parameters given in Table [IV.1](#)

IV.5 Numerical tests

In this section we introduce accurate numerical strategies for kinetic equations based on a stochastic Galerkin formulation of the derived equations, see Carrillo and Zanella [2019](#); G. Dimarco, L. Pareschi, and Zanella [2017](#); L. Pareschi [2021](#); Zhu and Jin [2017](#) and the references therein. In particular, we present several numerical tests highlighting the obtained theoretical results focusing first on the untreated tumour growth case providing results on spectral convergence of the adopted methods. Furthermore, we compare the evolution of the QoI with the experimental data. Next, we investigate the case including therapies through the considered control protocols testing its effectiveness in damping the introduced uncertainties at the level of observable quantities. In the following, we will consider all the tumours' volumes scaled by a factor of 10^5 .

IV.5.1 Stochastic Galerkin methods

The stochastic Galerkin (sG) method is based on the construction of a set of hierarchical orthogonal polynomials $\{\Psi_k(\mathbf{z})\}_{k=0}^M$ of degree less or equal to $M \in \mathbb{N}$, orthonormal with respect to the PDF of the random parameters $\rho(\mathbf{z})$, that is

$$\mathbb{E}_{\mathbf{z}}[\Psi_k(\mathbf{z})\Psi_h(\mathbf{z})] = \int_{\mathbb{R}^d} \Psi_k(\mathbf{z})\Psi_h(\mathbf{z})\rho(\mathbf{z})d\mathbf{z} = \delta_{kh}, \quad k, h = 0, \dots, M,$$

where δ_{kh} is the Kronecker delta. The choice for the orthogonal polynomials obviously depends on the PDF of the parameters $\rho(\mathbf{z})$ and follows the so-called Wiener-Askey scheme (see Xiu [2010](#); Xiu and Karniadakis [2002](#)).

Let $f = f(\mathbf{z}, x, t)$ be the solution of a Fokker-Planck equation at time $t \geq 0$, provided that it is sufficiently regular, it can be approximated by f^M that is defined as follows

$$f(\mathbf{z}, x, t) \approx f^M(\mathbf{z}, x, t) = \sum_{k=0}^M \hat{f}_k(x, t)\Psi_k(\mathbf{z}), \quad (\text{IV.28})$$

where $\hat{f}_k(x, t)$ is the projection of the solution over the space generated by the polynomial of degree $k = 0, \dots, M$

$$\hat{f}_k(x, t) := \mathbb{E}_{\mathbf{z}}[f(\mathbf{z}, x, t)\Psi_k(\mathbf{z})] = \int_{\mathbb{R}^d} f(\mathbf{z}, x, t)\Psi_k(\mathbf{z})\rho(\mathbf{z})d\mathbf{z}.$$

Hence, if we substitute the approximation [\(IV.28\)](#) of the PDF into the Fokker-Planck equation [\(IV.11\)](#), exploiting the orthonormality of the polynomials, we find a system of $M+1$ equations for the time evolution of the projections $\hat{f}_k(x, t)$, that reads

$$\partial_t \hat{f}_k(x, t) = \partial_x \left[\sum_{h=0}^M \mathcal{A}_{kh}(x) \hat{f}_h(x, t) + \frac{\sigma^2}{2} \partial_x (x^2 \hat{f}_k(x, t)) \right], \quad (\text{IV.29})$$

where the matrix $\mathcal{A}_{kh}(x)$ is defined as

$$\mathcal{A}_{kh}(x) = - \int_{\mathbb{R}^d} x \Phi_\delta(x/x_L, \mathbf{z}) \Psi_k(\mathbf{z}) \Psi_h(\mathbf{z}) \rho(\mathbf{z}) d\mathbf{z}.$$

We stress the fact that the system of equations [\(IV.29\)](#) is deterministic since it does not depend on the random parameters \mathbf{z} . The main advantage of the

stochastic Galerkin approach relies on the fact that, if the solution of the PDE of interest is sufficiently regular, the approximated solution spectrally converges to the correct solution of the problem. This translates into the fact that it is sufficient to consider M relatively small.

Analogous computations can be performed in the model that includes the introduced control (IV.26) with the only difference that the drift coefficient results modified by an additional term. In particular, in the controlled case the matrix $\mathcal{A}_{kh}(x)$ reads

$$\mathcal{A}_{kh}(x) = - \int_{\mathbb{R}^d} \left(x\Phi(x/x_L, \mathbf{z}) - \frac{S^2(x)(x - x_d)}{\kappa} \right) \Psi_k(\mathbf{z})\Psi_h(\mathbf{z})\rho(\mathbf{z})d\mathbf{z}.$$

In order to prove the stability result for the sG scheme, we may reformulate the Fokker-Planck equation (IV.29) in a more compact form. If we define the $M + 1$ vector $\hat{\mathbf{f}}(x, t) = (\hat{f}_0(x, t), \dots, \hat{f}_M(x, t))$, the $(M + 1) \times (M + 1)$ matrix $\mathbf{A}(x) = \{\mathcal{A}_{kh}(x) + \sigma^2 x \mathbb{I}\}_{k,h=0}^M$, being \mathbb{I} a unitary matrix, and the diffusion coefficient $D(x) = x^2 \sigma^2 / 2$, we have

$$\partial_t \hat{\mathbf{f}}(x, t) = \partial_x \left[\mathbf{A}(x) \hat{\mathbf{f}}(x, t) + D(x) \partial_x \hat{\mathbf{f}}(x, t) \right]. \quad (\text{IV.30})$$

We denote with $\|\hat{\mathbf{f}}\|_{L^2}$ the standard L^2 norm of the vector $\hat{\mathbf{f}}(x, t)$

$$\|\hat{\mathbf{f}}\|_{L^2} := \left[\int_{\mathbb{R}_+} \left(\sum_{k=0}^M \hat{f}_k^2(x, t) \right) dx \right]^{1/2},$$

and we observe that, thanks to the orthonormality of the polynomials $\{\Psi_k\}_{k=0}^M$ in $L^2(\Omega)$, we have

$$\|f^M\|_{L^2(\Omega)} = \|\hat{\mathbf{f}}\|_{L^2}.$$

Now, we can show the stability result.

Theorem IV.5.1. *Assume that there exists two constants $C_A > 0$ such that $\|\partial_x \mathcal{A}_{kh}\|_{L^\infty} \leq C_A$ for every $k, h = 0, \dots, M$ and $D(x) > 0$ for every $x \in \mathbb{R}_+$, then*

$$\|\hat{\mathbf{f}}\|_{L^2}^2 \leq e^{C_A t} \|\hat{\mathbf{f}}(0)\|_{L^2}^2.$$

Proof. We multiply every component of (IV.30) by \hat{f}_k and we integrate over \mathbb{R}_+ to get

$$\int_{\mathbb{R}_+} \frac{1}{2} \partial_t (\hat{f}_k^2) dx = \int_{\mathbb{R}_+} \hat{f}_k \partial_x \left[\sum_{h=0}^M \mathcal{A}_{kh} \hat{f}_h + D(x) \partial_x \hat{f}_k \right] dx.$$

We integrate by parts the transport term on the right-hand side of the equation to obtain

$$\begin{aligned} \sum_{h=0}^M \int_{\mathbb{R}_+} \hat{f}_k \partial_x (\mathcal{A}_{kh} \hat{f}_h) dx &= \sum_{h=0}^M \int_{\mathbb{R}_+} (\hat{f}_k \hat{f}_h \partial_x \mathcal{A}_{kh} + \hat{f}_k \mathcal{A}_{kh} \partial_x \hat{f}_h) dx \\ &= - \sum_{h=0}^M \int_{\mathbb{R}_+} \mathcal{A}_{kh} \partial_x (\hat{f}_k \hat{f}_h) dx - \sum_{h=0}^M \int_{\mathbb{R}_+} \hat{f}_h \partial_x (\mathcal{A}_{kh} \hat{f}_k) dx. \end{aligned}$$

We sum over $k = 0, \dots, M$ and we exploit the symmetry of \mathbf{A} to have

$$\begin{aligned} 2 \sum_{k,h=0}^M \int_{\mathbb{R}_+} \hat{f}_k \partial_x (\mathcal{A}_{kh} \hat{f}_h) dx &= - \sum_{k,h=0}^M \int_{\mathbb{R}_+} \mathcal{A}_{kh} \partial_x (\hat{f}_k \hat{f}_h) dx \\ &= \sum_{k,h=0}^M \int_{\mathbb{R}_+} \hat{f}_k \hat{f}_h \partial_x \mathcal{A}_{kh} dx. \end{aligned}$$

Since $\|\partial_x \mathcal{A}_{kh}\|_{L^\infty} \leq C_A$ and from Cauchy-Schwartz inequality, we have

$$\sum_{k,h=0}^M \int_{\mathbb{R}_+} \hat{f}_k \partial_x (\mathcal{A}_{kh} \hat{f}_h) dx \leq \frac{C_A}{2} \|\hat{\mathbf{f}}\|_{L^2}^2.$$

As for the diffusion term, we have

$$\sum_{k=0}^M \int_{\mathbb{R}_+} \hat{f}_k \partial_x (D(x) \partial_x \hat{f}_k) dx = - \sum_{k=0}^M \int_{\mathbb{R}_+} D(x) (\partial_x \hat{f}_k)^2 dx \leq 0,$$

since $D(x) \geq 0$ by assumption. If we sum over k , the left-hand side is nothing but the derivative in time of the L^2 norm of $\hat{\mathbf{f}}$

$$\sum_{k=0}^M \int_{\mathbb{R}_+} \frac{1}{2} \partial_t (\hat{f}_k^2) dx = \frac{1}{2} \partial_t \|\hat{\mathbf{f}}\|_{L^2}^2.$$

Finally, we have

$$\frac{1}{2} \partial_t \|\hat{\mathbf{f}}\|_{L^2}^2 \leq \frac{C_A}{2} \|\hat{\mathbf{f}}\|_{L^2}^2,$$

and thanks to Gronwall's Lemma we conclude. ■

We concentrate on the case where the evolution of the Fokker-Planck equations [\(IV.13\)](#) and [\(IV.26\)](#) is affected by an uncorrelated 2D random term in the Gompertz case, *i.e.* $\mathbf{z} = (z_1, z_2)$ and $\mathbf{z} \sim \rho(z_1, z_2) = \rho_1(z_1)\rho_2(z_2)$, or by an uncorrelated 3D random term in the von Bertalanffy case, *i.e.* $\mathbf{z} = (z_1, z_2, z_3)$ and $\mathbf{z} \sim \rho(z_1, z_2, z_3) = \rho_1(z_1)\rho_2(z_2)\rho_3(z_3)$. The distribution of the components of the random vectors are determined by the analysis presented in [Section IV.4](#)

In the limit $\delta \rightarrow 0^+$, corresponding to a kinetic Gompertz model, the approximated solution is therefore given by

$$f(\mathbf{z}, x, t) = f^M(\mathbf{z}, x, t) \approx \sum_{h,k=0}^M \hat{f}_{hk}(x, t) \Psi_h^1(z_1) \Psi_k^2(z_2)$$

being $\{\Psi_h^1\}_{h=0}^M$ and $\{\Psi_k^2(z_2)\}_{k=0}^M$ the set of polynomials orthonormal with respect to $\rho_1(z_1)$ and $\rho_2(z_2)$ respectively. Under the introduced assumptions we obtain the following set of equations

$$\partial_t \hat{f}_{hk} = \partial_x \left[\sum_{\ell,r=0}^M \mathcal{A}_{hk\ell r} \hat{f}_{\ell r}(x, t) + \frac{\sigma^2}{2} \partial_x (x^2 \hat{f}_{hk}(x, t)) \right], \quad (\text{IV.31})$$

with

$$\mathcal{A}_{hk\ell r}(x) = - \int_{\mathbb{R}^2} x \Phi_\delta(x/x_L, \mathbf{z}) \Psi_h^1(z_1) \Psi_k^2(z_2) \Psi_\ell^1(z_1) \Psi_r^2(z_2) \rho_1(z_1) \rho_2(z_2) dz_1 dz_2.$$

Similarly, we can consider the approximated solution of the obtained von Bertalanffy kinetic model

$$f(\mathbf{z}, x, t) = f^M(\mathbf{z}, x, t) \approx \sum_{h,k,\ell=0}^M \hat{f}_{hk\ell}(x, t) \Psi_h^1(z_1) \Psi_k^2(z_2) \Psi_\ell^3(z_3)$$

that is determined by the following set of equations

$$\partial_t \hat{f}_{hk\ell} = \partial_x \left[\sum_{p,r,s=0}^M \mathcal{A}_{hk\ell p r s} \hat{f}_{p r s}(x, t) + \frac{\sigma^2}{2} \partial_x (x^2 \hat{f}_{hk\ell}(x, t)) \right], \quad (\text{IV.32})$$

and

$$\mathcal{A}_{hk\ell p r s}(x) = - \int_{\mathbb{R}^3} x \Phi_\delta(x/x_L, \mathbf{z}) \Psi_h^1(z_1) \Psi_k^2(z_2) \Psi_\ell^3(z_3) \Psi_p^1(z_1) \Psi_r^2(z_2) \Psi_s^3(z_3) \rho_1(z_1) \rho_2(z_2) \rho_3(z_3) dz_1 dz_2 dz_3.$$

IV.5.2 Free growth case: convergence and agreement with available data

In the following, we show the convergence of the sG scheme for the Fokker-Planck equation (IV.11). We consider deterministic initial conditions coherent with growth curves of Figure IV.1 after 100 days from the tumour onset. These observations are distributed as a Gamma density

$$f_0(x) = \frac{p_1^{p_2} x^{p_1-1} e^{-p_2 x}}{\Gamma(p_1)},$$

with $(p_1, p_2) = (0.3, 2.8)$ for the Gompertz case and with $(p_1, p_2) = (0.37, 2.2)$ for the von Bertalanffy case.

We introduce then a uniform discretisation of the domain $[0, 2] \subset \mathbb{R}_+$ obtained with $N = 201$ gridpoints, $\Delta x = 10^{-2}$ and a time discretisation of the interval $[0, T]$ obtained with $\Delta t = \Delta x/C$ with $C = 10^2$ and $T = 10$. A central difference scheme is then considered for the numerical solution of the systems of equations (IV.31)-(IV.32).

As for the uncertain parameters, we refer to Subsection IV.4.2 and in particular to Table IV.1 for the choice of the distributions and, consequently, of the polynomial basis. Let us recall that the Uniform distribution and the Beta distribution corresponds to a Legendre polynomial chaos expansion and a Jacobi polynomial chaos expansion, respectively.

In the following, we numerically check the convergence of the scheme in the space of random parameters in terms of the evolution of mean volumes. Hence, we consider a reference approximation of the first momentum

$$m^{\bar{M}}(\mathbf{z}, t) = \int_{\mathbb{R}_+} x f^{\bar{M}}(\mathbf{z}, x, t) dx$$

obtained with $\bar{M} = 50$ at fixed time $T = 10$. Then, we compute the L^2 error at time $t > 0$ defined as

$$\|m^{\bar{M}}(\mathbf{z}, t) - m^M(\mathbf{z}, t)\|_{L^2(\Omega)}$$

where $m^M(\mathbf{z}, T)$ is the first momentum obtained with a sG expansion up to order $M < \bar{M}$, with $M = 0, \dots, 30$. In Fig. IV.3 we may observe the rapid

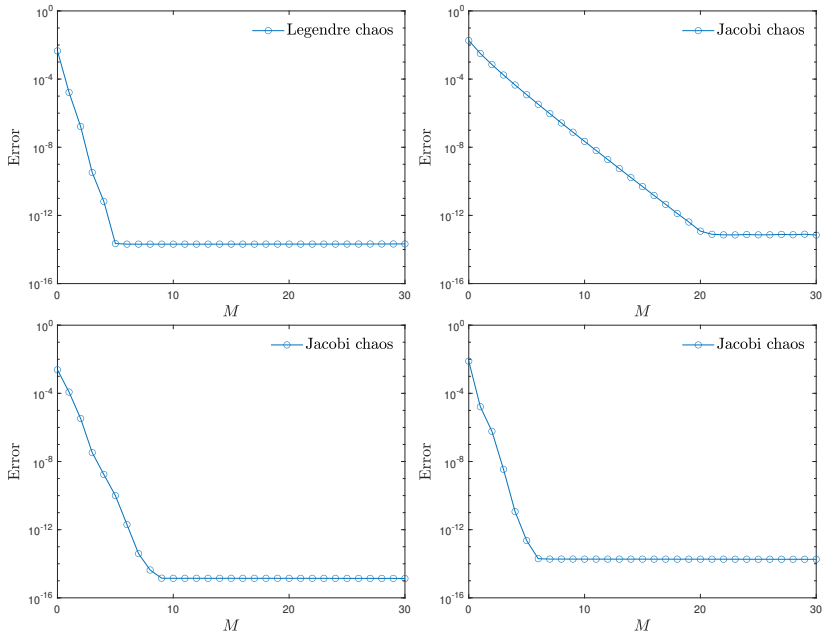


Figure IV.3: Convergence of the L^2 error with respect to a reference solutions obtained with $\bar{M} = 50$, at fixed time $T = 10$. The top row corresponds to the Gompertz case whereas the bottom row to the von Bertalanffy case. Top-Left: $z_1 = \alpha \sim \mathcal{U}([10^{-3}, 3 \cdot 10^{-2}])$ and fixed $z_2 = x_L \equiv 0.5$. Top-Right: $z_2 = x_L \sim \mathcal{B}(c_1, c_2)$ and fixed $z_1 = \alpha \equiv 0.01$. Bottom-Left: $z_1 = a \sim \mathcal{B}(c_1, c_2)$ and fixed $z_2 = q \equiv 0.01$, $z_3 = x_L \equiv 0.5$. Bottom-Right: $z_2 = q \sim \mathcal{B}(c_1, c_2)$ and fixed $z_1 = a \equiv 0.8$, $z_3 = x_L \equiv 0.5$. The values (c_1, c_2) are reported in Table [IV.1](#).

decay of the numerical error in the random space in both models that we have considered. We observe that we reach essentially the machine precision with a relatively small number of projections.

Once we have checked for the spectral convergence of the method, we can investigate the behaviour of our models with respect to the experimental data. In particular, we will look at the QoI introduced in Section [IV.4](#). To this aim, we use the introduced numerical setting with $M = 3$ in all the subsequent numerical tests. In the top row of Fig. [IV.4](#) we show the emerging equilibrium distribution from [\(IV.31\)](#) with the discussed 2D uncertainty and in the right plot the evolution of the mean volume of the tumours. In the bottom row of Figure [IV.4](#) we concentrate on the model [\(IV.32\)](#) with 3D uncertainty and again the

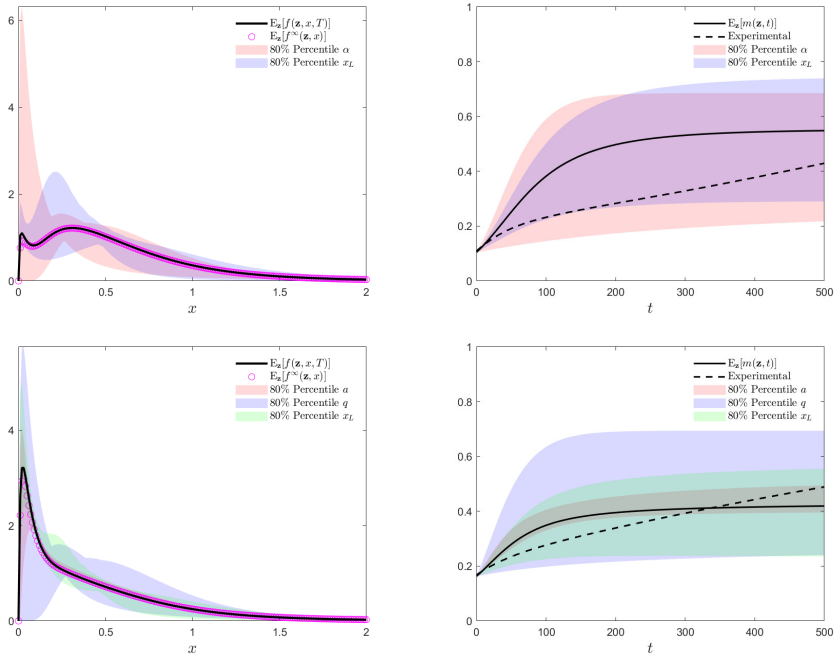
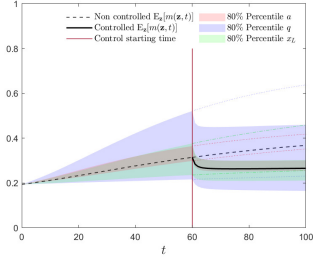


Figure IV.4: Top: large time distribution (left) and evolution of the mean volume (right) for the Gompertz kinetic model with 2D uncertainties. The solid line is the numerical solution of (IV.11) at the final time $T = 500$, the markers refers to the expectation of the analytic solution (IV.13). Bottom: large time distribution (left) and evolution of the mean volume (right) for the von Bertalanffy kinetic model with 3D uncertainties. In all the cases, we choose $\Delta x = 10^{-2}$, $\Delta t = \Delta x/C$ with $C = 10^2$ and $M = 3$. (For interpretation of the references to colour in this figure legend, the reader is referred to the web version of this article).

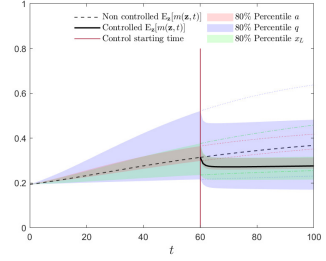
evolution of the mean volume of tumours in the right plot. The shaded colour bands are relative to the variability computed with percentiles with respect to the introduced uncertain quantities.

IV.5.3 Effects of the control and damping of uncertainties

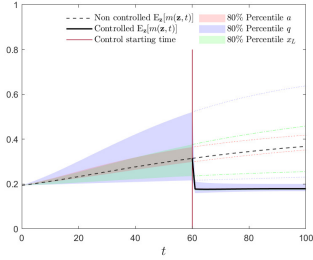
We consider now the kinetic models (IV.26) in presence of control strategies to test the effectiveness of the introduced control in reducing the tails of the distributions and damping the uncertainties of the system. For this reason, we consider here only the von Bertalanffy case that induces a power-law-type



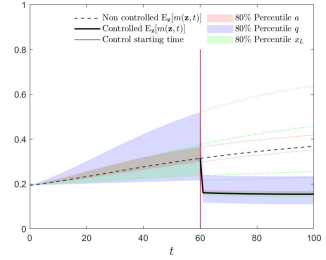
(a) $p = 1, \kappa = 1, S(x) = 1$



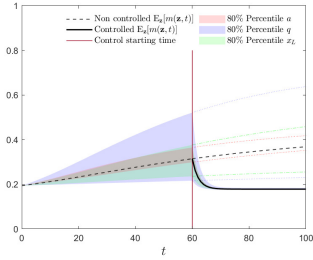
(b) $p = 1, \kappa = 1, S(x) = \sqrt{x}$



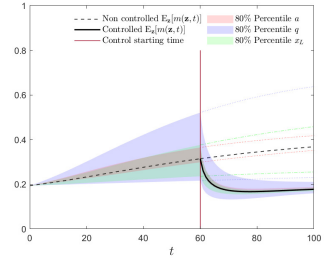
(c) $p = 1, \kappa = 0.1, S(x) = 1$



(d) $p = 1, \kappa = 0.1, S(x) = \sqrt{x}$



(e) $p = 2, \kappa = 1, S(x) = 1$



(f) $p = 2, \kappa = 1, S(x) = \sqrt{x}$

Figure IV.5: Evolution of $m(\mathbf{z}, t)$ in the uncontrolled scenario for $t \leq 60$ and in a controlled scenario for $t > 60$, with $p = 1, 2$, $S(x) = 1, \sqrt{x}$ and $\kappa = 0.1, 1$. The dashed lines represent the trend of the tumour if the control is not in action. In the case $p = 2$, we adopted a sG scheme with $\Delta x = 10^{-2}$, $\Delta t = \Delta x/C$ with $C = 10^2$, $M = 3$ for the numerical solution of (IV.32) with the introduced clinical uncertainties. In the case $p = 1$, we adopted a stochastic collocation DSMC with $N = 10^5$, $\Delta t = 0.05$, $\epsilon = 2\Delta t$ and $M = 3$. We considered the experimental target volume size $x_d = 0.18 \times 10^5 \text{mm}^3$. and the results are scaled by a factor 10^5 .

equilibrium distribution as discussed in Section [IV.2.2](#). From experimental measurements we observed an average value of the target volume $x_d = 0.18 \times 10^5 \text{mm}^3$ after the implemented therapeutic protocols, for this reason we have fixed this value in each experiment of this section. The obtained value of the target volume will be scaled by a factor 10^5 through the section. The activate the control we compute the mean tumours' size from experimental data. Hence, u starts acting when $\mathbb{E}_{\mathbf{z}}[m(\mathbf{z}, t)]$ exceeds this threshold.

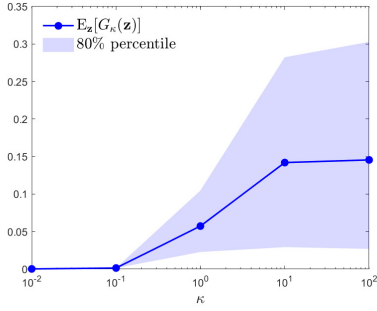
In Fig. [IV.5](#) we present the evolution of the expected values of the first order momentum $m(\mathbf{z}, t)$ in a constrained setting obtained from [\(IV.26\)](#). In particular, we plot the uncontrolled evolutions up to the time $t = 60$ and then we activate the control. As in the uncontrolled scenario, we consider a uniform discretisation of $[0, 2]$ obtained with $N = 201$ gridpoints and a time step $\Delta t = \Delta x/C$, with $C = 10^2$, for the time interval $[0, T]$, with $T = 100$ final time. We notice that the control succeeds in reducing both the expected values of the first momentum and the uncertainty, with smaller values of κ .

To quantify the effectiveness of the adopted control strategy, we define an index that quantifies the variability around the target x_d computed at a given time $T > 0$ and defined as follows

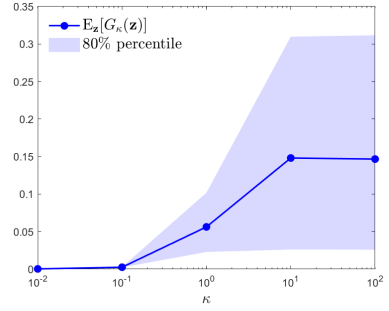
$$G_{\kappa}(\mathbf{z}) = \int_{\mathbb{R}_+} (x - x_d)^2 f(\mathbf{z}, x, T) dx, \quad (\text{IV.33})$$

where $f(\mathbf{z}, x, T)$ is the kinetic distribution of the controlled model with embedding the penalisation coefficient $\kappa > 0$. In Fig. [IV.6](#) we show the behaviour of $\mathbb{E}_{\mathbf{z}}[G_{\kappa}(\mathbf{z})]$ together with confidence bands and computed for several penalisation coefficients. We considered both the cases $p = 1, 2$ and selective functions $S(x) = 1, \sqrt{x}$.

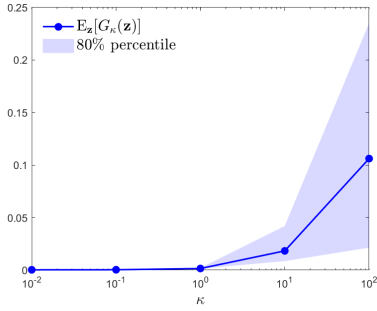
For the case $p = 1$ we adopt a stochastic collocation approach for the kinetic model [\(IV.17\)](#) that is solved through a DSMC scheme (Tosin and Zanella [2018](#)). We choose $N = 10^5$, $M = 3$ and $\Delta t = 0.05$ and $\epsilon = 2\Delta t$. We notice that, in all the considered cases, $\mathbb{E}_{\mathbf{z}}[G_{\kappa}(\mathbf{z})]$ decreases with smaller values of κ and the uncertainty is dampen.



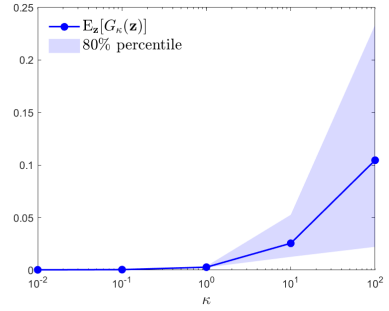
(a) $p = 1, S(x) = 1$



(b) $p = 1, S(x) = \sqrt{x}$



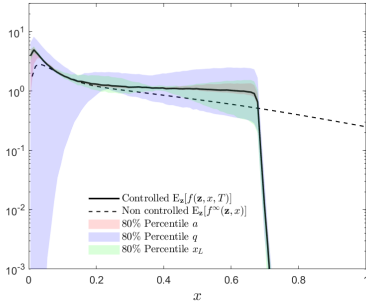
(c) $p = 2, S(x) = 1$



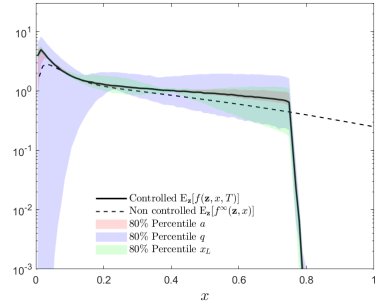
(d) $p = 2, S(x) = \sqrt{x}$

Figure IV.6: Expectation of the quantity $G_\kappa(\mathbf{z})$ defined in (IV.33) and computed with $x_d = 0.18$ versus the penalisation κ , for $p = 1, 2$ and $S(x) = 1, \sqrt{x}$, considering the von Bertalanffy model with uniform-distributed coefficients. The plots are in semi-logarithmic scale to highlight the uncertainty damping for small values of κ . In all the cases, a collocation DSMC scheme is adopted, with the choices $N = 10^5$, $M = 3$, $\Delta t = 0.05$ and $\epsilon = 2\Delta t$.

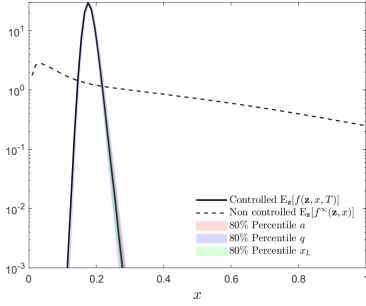
Now we look directly to the effectiveness of the control strategies in reducing both the tails and the uncertainty of the distributions. In Fig. IV.7 we show the expected distributions in the controlled case for large times, obtained with the introduced sG scheme for the kinetic von Bertalanffy model. We may observe how the introduction of selectivity is capable to change the behaviour of the tail of the distribution as discussed in Section IV.3.1.2



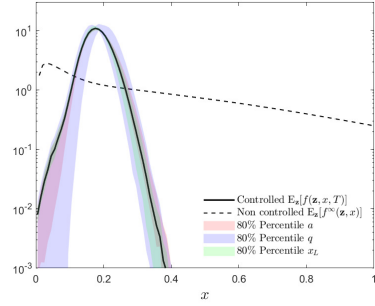
(a) $p = 1, \kappa = 1, S(x) = 1$



(b) $p = 1, \kappa = 1, S(x) = \sqrt{x}$



(c) $p = 2, \kappa = 1, S(x) = 1$



(d) $p = 2, \kappa = 1, S(x) = \sqrt{x}$

Figure IV.7: Details of the expected value of the controlled and uncontrolled distributions in the von Bertalanffy growth scenario, for fixed penalisation $\kappa = 1$, $p = 1, 2$ and $S(x) = 1, \sqrt{x}$. The solid line is the numerical controlled solution at the final time $T = 100$, the dashed line is the uncontrolled analytic solution at the equilibrium. The plots are in semi-logarithmic scale to highlight the suppression of the fat tails. We considered the experimental target volume size $x_d = 0.18 \times 10^5 \text{mm}^3$ and results are scaled by a factor 10^5 .

Conclusions

In the present paper, we concentrated on the influence of uncertain quantities on kinetic models for tumour growths. Under suitable assumptions, we derived surrogate Fokker-Planck models from which we obtain analytical insight on the large time behaviour of the system. Hence, we proposed suitable selective control strategies mimicking the effects of therapies in steering the volume of tumours towards a target value x_d . Through explicit computations, we showed that the

solution of the controlled model is close to the target volume and the distance of the first order momentum from x_d depends on the penalisation of the control. These control protocols are capable to dampen the variability of the tumours' dynamics due to the presence of uncertainties. Since from the pathological point of view fat-tailed distributions are related to a higher probability of finding large tumours with respect to thin-tailed distributions we observed that by implementing suitable selective strategies we can also change the nature of the emerging distribution of tumours' sizes. Thanks to real observations on a cohort of subjects we observed great variability in the choice of parameters of the models that has been considered in the numerical section. Numerical schemes for the uncertainty quantification of kinetic equations are then considered to observe the effects of the control on the solution of the models.

References

- Agosti, A. et al. (2018). “A personalized mathematical tool for neuro-oncology: A clinical case study”. In: *Int. J. Non Linear Mech.* vol. 107, pp. 170–181.
- Albano, G. and Giorno, V. (2006). “A stochastic model in tumour growth”. In: *J. Theor. Biol.* vol. 242, pp. 329–336.
- Albi, G., Fornasier, M., and Kalise., D. (2016). “A Boltzmann approach to mean-field sparse feedback control”. In: *IFAC PapersOnLine* vol. 50(1), pp. 2898–2903.
- Albi, G., Herty, M., and Pareschi, L. (2015). “Kinetic description of optimal control problems and applications to opinion consensus”. In: *Commun. Math. Sci.* vol. 13(6), pp. 4–21.
- Albi, G. and Pareschi, L. (2018). “Selective model-predictive control for flocking systems”. In: *Commun. Appl. Ind. Math.* vol. 9(2), pp. 4–21.
- Albi, G., Pareschi, L., and Zanella, M. (2014). “Boltzmann-type control of opinion consensus through leaders”. In: *Phil. Trans. R. Soc. A* vol. 372, p. 20140138.

- Bailo, R. et al. (2018). “Optimal consensus control of the Cucker-Smale model”. In: *IFAC PapersOnLine* vol. 51(13), pp. 1–6.
- Bensoussan, A., Frehse, J., and Yam, P. (2013). “Mean Field Games and Mean Field Type Control Theory”. In: *SpringerBriefs in Mathematics*.
- Benzekry, S. et al. (2014). “Classical mathematical models for description and prediction of experimental tumour growth”. In: *PLoS Comput. Biol.* vol. 10(8).
- Carrillo, J. A., Pareschi, L., and Zanella, M. (2019). “Particle based gPC methods for mean-field models of swarming with uncertainty”. In: *Commun. Comput. Phys.* vol. 25(2), pp. 508-531–954.
- Carrillo, J. A. and Zanella, M. (2019). “Monte Carlo gPC methods for diffusive kinetic flocking models with uncertainties.” In: *Viet. J. Math.* vol. 47(4), pp. 931–954.
- Cercignani, C. (1988). “The Boltzmann Equation and its Applications”. In: *Springer Series in Applied Mathematical Sciences* vol. 67.
- Conte, Martina and Surulescu, Christina (2021). “Mathematical modeling of glioma invasion: acid-and vasculature mediated go-or-grow dichotomy and the influence of tissue anisotropy”. In: *Applied Mathematics and Computation* vol. 407, p. 126305.
- Degond, P., Herty, M., and Liu, J.-G. (2017). “Meanfield games and model predictive control”. In: *Commun. Math. Sci.* vol. 15(5), pp. 1403–1422.
- Dimarco, G., Pareschi, L., and Zanella, M. (2017). “Uncertainty quantification for kinetic models in socio-economic and life sciences”. In: *Uncertainty Quantification for Hyperbolic and Kinetic Equations* vol. 14, pp. 151–191.
- Dimarco, Giacomo and Toscani, Giuseppe (2020). “Social climbing and Amoroso distribution”. In: *Mathematical Models and Methods in Applied Sciences* vol. 30, no. 11, pp. 2229–2262.
- During, B., Pareschi, L., and Toscani, G. (2018). “Kinetic models for optimal control of wealth inequalities.” In: *Europ. Phys. J. B* vol. 91, p. 265.

- Engwer, Christian et al. (2015). “Glioma follow white matter tracts: a multiscale DTI-based model”. In: *Journal of mathematical biology* vol. 71, no. 3, pp. 551–582.
- Fedorov, A. et al. (2012). “3D Slicer as an Image Computing Platform for the Quantitative Imaging Network.” In: *Magn Reson Imaging* vol. 30(9), pp. 1323–41.
- Fornasier, M., Piccoli, B., and Rossi, F. (2014). “Mean-field sparse optimal control.” In: *Phil. Trans. R. Soc. A* vol. 372.
- Frank, S. A. (2007). “Dynamics of Cancer: Incidence, Inheritance, and Evolution”. In: *Princeton Series in Evolutionary Biology*.
- Gerlee, P. (2013). “The model muddle: In search of tumour growth laws”. In: *Cancer Res.* vol. 73, pp. 2407–4211.
- Giverso, C. and Preziosi, L. (2019). “Influence of the mechanical properties of the necrotic core on the growth and remodelling of tumour spheroids”. In: *Int. J. Non Linear Mech.* vol. 108, pp. 20–32.
- Grizzi, F. and Chiriva-Internati, M. (2006). “Cancer: looking for simplicity and finding complexity”. In: *Cancer Cell Int.* vol. 6, :4.
- Han, Sue et al. (2020). “IDH mutation in glioma: molecular mechanisms and potential therapeutic targets”. In: *British journal of cancer* vol. 122, no. 11, pp. 1580–1589.
- Henscheid, N. et al. (2018). “Physiological random processes in precision cancer therapies”. In: *PLoS One* vol. 13(6).
- Herty, M., Steffensen, S., and Pareschi, L. (2015). “Mean-field control and Riccati equations”. In: *Netw. Heter. Media* vol. 10, pp. 699–715.
- Kashdan, Eugene and Pareschi, Lorenzo (2012). “Mean field mutation dynamics and the continuous Luria–Delbrück distribution”. In: *Mathematical biosciences* vol. 240, no. 2, pp. 223–230.
- Laird, A. K. (1965). “Dynamics of tumour growth: comparison of growth rates and extrapolation of growth curve to one cell”. In: *British Journal of Cancer* vol. 19(2), : 278.

- (1964). “ Dynamics of tumour growth”. In: *British Journal of Cancer* vol. 18(3), : 490.
- Langer, R. et al. (1980). “Control of tumour growth in animals dy infusion of an angiogenesis inhibitor”. In: *Proc. Natl. Acad. Sci. USA* vol. 77, pp. 4331–4335.
- Leory-Lerêtre, M. et al. (2017). “ Are tumour cell lineages solely shaped by mechanics forces?” In: *Bull. Math. Biol.* vol. 79(10), pp. 2356–2393.
- Loy, N. and Preziosi, L. (2020). “ Kinetic models with non-local sensing determining cell polarization and speed according to independent cue ”. In: *J. Math. Biol.* vol. 80, pp. 373–421.
- Ma, Z. et al. (2020). “ Stochastic growth pattern of untreated human glioblastomas predicts the survival time for patients ”. In: *Sci. Rep.* vol. 10 (1), pp. 1–13.
- Marušić, M., Vuk-Pavlovic, S., and Frejer, J. P. (1994). “ tumour growth in vivo and as multicellulas spheroids compared by mathematical models ”. In: *Bull. Math. Biol.* vol. 56 (4), pp. 617–631.
- Nobile, A. G. and Ricciardi, L. M. (1980). “Growth and extinction in random environment ”. In: *Appl. Inform. Control Syst.*, pp. 455–465.
- Norton, L. (1988). “A Gompertzian model on human breast cancer growth ”. In: *Cancer Res.* vol. 48, pp. 7067–7071.
- Painter, KJ and Hillen, Thomas (2013). “Mathematical modelling of glioma growth: the use of diffusion tensor imaging (DTI) data to predict the anisotropic pathways of cancer invasion”. In: *Journal of theoretical biology* vol. 323, pp. 25–39.
- Pareschi, L. (2021). “An introduction to uncertainty quantification for kinetic equations and related problems ”. In: *Trails in Kinetic Theory: Foundational Aspects and Numerical Methods* vol. 25, pp. 141–181.
- Pareschi, L. and Toscani, G. (2013). *Interacting Multiagent Systems: Kinetic Equations and Monte Carlo Methods*. Oxford University Press.

- Pareschi, L. and Zanella, M. (2020). “Monte Carlo stochastic Galerkin methods for the Boltzmann equation with uncertainties: space-homogeneous case ”. In: *J. Comput. Phys.* vol. 423.
- Preziosi, L., Toscani, G., and Zanella, M. (2021). “Control of tumour growth distributions through kinetic methods. ” In: *J. Theor. Biol.*
- Risken, H. (1996). *The Fokker-Planck Equation: Methods of Solution and Applications.*
- Rodriguez-Brenes, I. A., Komarova, N. J., and Wodarz, D. (2013). “tumour growth dynamics: insights into evolutionary processes ”. In: *Trends Ecol. Evol.* vol. 28, pp. 597–604.
- Roose, T., J. Chapman, S., and Maini, P. K. (2007). “Mathematical models of avascular tumour growth ”. In: *SIAM Rev.* vol. 49 (2), pp. 179–208.
- Toscani, G. (2006). “ Kinetic models of opinion formation”. In: *Commun. Math. Sci.* vol. 4 (3), pp. 481–496.
- Toscani, Giuseppe (2013). “A kinetic description of mutation processes in bacteria”. In: *Kinetic & Related Models* vol. 6, no. 4, p. 1043.
- Tosin, A. and Zanella, M. (2018). “ Boltzmann-type models with uncertain binary interactions”. In: *Commun. Math. Sci.* vol. 16 (4), pp. 962–984.
- (2021). “ Uncertainty damping in kinetic traffic models by driver-assist controls”. In: *Math. Contr. Relat Fields* vol. 11 (3), pp. 681–713.
- West, G. B., Brown, J. H., and Enquist, B. J. (2001). “ A general model for ontogenetic growth”. In: *Nature* vol. 413, pp. 628–631.
- West, J. and Newton, P.K. (2019). “ Cellular interactions constrain tumour”. In: *PNAS* vol. 116 (6), pp. 1918–1923.
- Wheldon., T. E. (1988). *Mathematical Models in Cancer Research.* Taylor & Francis.
- Wodarz, D. and Komarova, N. (2014). *Dynamics of Cancer: Mathematical Foundations of Oncology.* World Scientific.
- Xiu, D. (2010). *Numerical Methods for Stochastic Computations.* Princeton University Press.

- Xiu, D. and Karniadakis, G. E. (2002). “The Wiener-Askey polynomial chaos for stochastic differential equations”. In: *SIAM J. Sci. Comput.* vol. 42 (2), pp. 614–644.
- Zhu, Y. and Jin, S. (2017). “The Vlasov-Poisson-Fokker-Planck system with uncertainty and a one-dimensional asymptotic preserving method”. In: *Multiscale Model. Simul.* vol. 15 (4), pp. 1502–1529.

Part 3

A first attempt to combine
quantum field theory, neural
network and brain description

Introduction

The brain is an organ capable of extreme complex activities that elaborates and integrates internal and external stimuli. Its behavior spans nine orders of magnitude-scale in spatial structures tiers in ways that have yet to be fully understood (Swan, Santos, and Witte [2022](#)). Modeling the brain means to introduce a mathematical framework to reproduce the non-linear dynamics of a physical system exhibiting a highly stochastic activity (Rolls and Deco [2010](#)). Brain models also link hidden neuronal processes to observed neural data obtained from Elettroencephalography (EEG) (Binnie and Prior [1994](#)), Magnetoencephalography (MEG) (Proudfoot et al. [2014](#)) and functional MRI (fMRI) (Matthews and Jezzard [2004](#)).

There are two main classes of brain models (Toronov et al. [2013](#)) one based on single neurons organized into functional units (Markram [2006](#)), and another based on the average behavior of neuronal populations (Friston, Harrison, and Penny [2003](#); Haken [2007](#); Valdes-Sosa et al. [2009](#)). Early neurodynamic models, such as Wilson-Cowan model (Wilson and Cowan [1972](#)), are based on the description of interactions between populations of excitatory and inhibitory neurons. However, to deal with large cerebral neural networks and to compare model predictions with spatially averaged neuronal signals directly measured with non-invasive tools (such as EEG and fMRI), it is introduced the mean field approximations of subpopulations of excitatory and inhibitory neurons. A mean field brain model is based on stochastic differential equations that include random fluctuations and it expresses the distribution of the neuronal activity states in terms of probability density. In particular, in Jirsa and Haken works (Jirsa and Haken [1996](#); Jirsa and Haken [1997](#)) a semi-quantitative non-linear model based on quasi-microscopic properties of neural populations and realistic

anatomical connectivity is developed, with a temporal evolution in agreement, in some extent, with the signals of magnetoencephalography measured by Kelso et al. [1992]. In addition, it is also introduced in Haken [2007] the idea of synchronization as the element underlying information processing mechanism of combining signals from various regions of the brain.

Another model that summarizes the activity of the neuronal population with a single state, *i.e.*, by mean activity, is the neural mass model (David and Friston [2003]; Moran et al. [2007]). The central idea is to approximate a group of neurons by its average properties by treating the current state “*as a point ‘mass’, i.e a delta function, approximation to the underlying density on the population’s states*”(Marreiros, Kiebel, and Friston [2010]). Conversely to mean field models, neural mass models describe neuronal states evolution through ordinary differential equations.

Brain space-state models are known in literature as Dynamic causal models (DCM) (Friston, Harrison, and Penny [2003]) in which the brain is treated as a deterministic non-linear dynamic system influenced by inputs and producing outputs. The distinguishing trait of this approach is framing the problem of the parameterized connectivity estimation by perturbing the system and measuring its response.

All these models are based on the classical treatment of the underlying neuronal physical processes and they all rely on the assumption that neurons are modeled as binary units, whose output can be represented by a step-function. These models also consider the activity or inactivity states of the neurons, the values of neurons’ thresholds and the strangeness of their coupling coefficients as the most important parameters of the brain. In this way, the instantaneous net behavior can be obtained as the solution of a N nonlinear equations which can be solved once the specification of the neurons’ couplings and thresholds are defined (Globus, Pribram, and Vitiello [2004]). Models of this type encourage a computer-like machine vision performing classical stimulus-response computations. In this regard, a very powerful tool for simulating the brain is The Virtual Brain (TVB) that reduces the complexity on the micro level

to attain the macro organization and it also merges the individual patient's anatomy from brain imaging data with state-of-art mathematical modeling (Sanz Leon et al. [2013], <https://www.thevirtualbrain.org/tvb/zwei>).

New studies, however, demonstrate that biological systems exhibit non-trivial quantum effects as a result of their interaction with the noisy environment (Rolls and Deco [2010]). Therefore, quantum events may have an impact on brain activity (Jedlicka [2017], see also Koch and Hepp [2006]), since nonlinear chaotic dynamics can amplify, instead of self-averaging, the lowest-level quantum fluctuations that can affect large-scale mesoscopic and macroscopic neuronal activity. The first approach to describe fundamental brain information processing with physical quantum theory principle is related to the theory proposed by Umezawa and Ricciardi (Ricciardi and Umezawa [1967]) that describes the physical aspect of living matter in terms of collective mode. In Fröhlich [1968] it is pointed out the existence of coherent dipolar wave propagation in the cytoskeletal structure of biological cells and its interaction with external magnetic fields. After the Umezawa model, several physicists began to investigate the quantum nature and dynamics of the brain (QBD). Among them, there are the works of Penrose and Nanopoulos (Pothos and Busemeyer [2009], Yukalov and Sornette [2011]) according to which quantum phenomena are essential for consciousness and they occur in cytoskeletal microtubules within brain neurons. In fact, microtubules' periodic paracrystalline structure makes microtubules able to support superposition of coherent quantum states. Although this idea was initially approached with skepticism and dismissed by some scientists, recent researches on EEG rhythms and on anesthesia seem to support it (<https://www.elsevier.com/>).

Guided by all these evidences supporting a quantum treatment of the brain, we try to introduce a quantum field theory and a deep learning framework for the description and the simulation of a brain portion. This is a still ongoing project and the obtained results are presented in the draft below.

References

- Binnie, CD and Prior, PF (1994). “Electroencephalography.” In: *Journal of Neurology, Neurosurgery & Psychiatry* vol. 57, no. 11, pp. 1308–1319.
- David, Olivier and Friston, Karl J (2003). “A neural mass model for MEG/EEG:: coupling and neuronal dynamics”. In: *NeuroImage* vol. 20, no. 3, pp. 1743–1755.
- Friston, Karl J, Harrison, Lee, and Penny, Will (2003). “Dynamic causal modelling”. In: *Neuroimage* vol. 19, no. 4, pp. 1273–1302.
- Fröhlich, Herbert (1968). “Long-range coherence and energy storage in biological systems”. In: *International Journal of Quantum Chemistry* vol. 2, no. 5, pp. 641–649.
- Globus, Gordon G, Pribram, Karl H, and Vitiello, Giuseppe (2004). *Brain and being: at the boundary between science, philosophy, language and arts*. Vol. 58. John Benjamins Publishing.
- Haken, Hermann (2007). *Brain dynamics: an introduction to models and simulations*. Springer Science & Business Media.
- Jedlicka, P. (2017). “Revisiting the quantum brain hypothesis: toward quantum (neuro) biology?” In: *Frontiers in molecular neuroscience* vol. 10, p. 366.
- Jirsa, Viktor K and Haken, Hermann (1996). “Field theory of electromagnetic brain activity”. In: *Physical review letters* vol. 77, no. 5, p. 960.
- (1997). “A derivation of a macroscopic field theory of the brain from the quasi-microscopic neural dynamics”. In: *Physica D: Nonlinear Phenomena* vol. 99, no. 4, pp. 503–526.
- Kelso, JAS et al. (1992). “A phase transition in human brain and behavior”. In: *Physics Letters A* vol. 169, no. 3, pp. 134–144.
- Koch, C. and Hepp, K. (2006). “Quantum mechanics in the brain”. In: *Nature* vol. 440, no. 7084, pp. 611–611.
- Markram, Henry (2006). “The blue brain project”. In: *Nature Reviews Neuroscience* vol. 7, no. 2, pp. 153–160.

- Marreiros, André C, Kiebel, Stefan J, and Friston, Karl J (2010). “A dynamic causal model study of neuronal population dynamics”. In: *Neuroimage* vol. 51, no. 1, pp. 91–101.
- Matthews, Paul M and Jezzard, Peter (2004). “Functional magnetic resonance imaging”. In: *Journal of Neurology, Neurosurgery & Psychiatry* vol. 75, no. 1, pp. 6–12.
- Moran, Rosalyn J et al. (2007). “A neural mass model of spectral responses in electrophysiology”. In: *NeuroImage* vol. 37, no. 3, pp. 706–720.
- Pothos, E. M. and Busemeyer, J. R. (2009). “A quantum probability explanation for violations of ‘rational’ decision theory”. In: *Proceedings of the Royal Society B: Biological Sciences* vol. 276, no. 1665, pp. 2171–2178.
- Proudfoot, Malcolm et al. (2014). “Magnetoencephalography”. In: *Practical neurology* vol. 14, no. 5, pp. 336–343.
- Ricciardi, Luigi Maria and Umezawa, Horoomi (1967). “Brain and physics of many-body problems”. In: *Kybernetik* vol. 4, no. 2, pp. 44–48.
- Rolls, E. T. and Deco, G. (2010). *The noisy brain: stochastic dynamics as a principle of brain function*. Vol. 34. Oxford university press Oxford.
- Sanz Leon, Paula et al. (2013). “The Virtual Brain: a simulator of primate brain network dynamics”. In: *Frontiers in neuroinformatics* vol. 7, p. 10.
- Swan, M., Santos, R. P. dos, and Witte, F. (2022). “Quantum Neurobiology”. In: *Quantum Reports* vol. 4, no. 1, pp. 107–126.
- Toronov, V et al. (2013). “Dynamics of the brain: Mathematical models and non-invasive experimental studies”. In: *The European Physical Journal Special Topics* vol. 222, no. 10, pp. 2607–2622.
- Valdes-Sosa, Pedro A et al. (2009). “Model driven EEG/fMRI fusion of brain oscillations”. In: *Human brain mapping* vol. 30, no. 9, pp. 2701–2721.
- Wilson, Hugh R and Cowan, Jack D (1972). “Excitatory and inhibitory interactions in localized populations of model neurons”. In: *Biophysical journal* vol. 12, no. 1, pp. 1–24.

Yukalov, V. I. and Sornette, D. (2011). “Decision theory with prospect interference and entanglement”. In: *Theory and Decision* vol. 70, no. 3, pp. 283–328.

Paper V

Quantum Field Theory and Neural Network for the description of a brain portion: a first attempt

Giulia Colelli^{1,2,3,*}, Francesco Giovanni Celiberto^{4,5,6}, Anna Pichiecchio^{7,2}, Silvia Figini^{8,9}, Alessandro Bacchetta^{10,3}

Manuscript in preparation

Abstract

We propose an exploratory study to combine quantum-field theory and neural-network approaches to describe a brain portion. By drawing a parallel with theoretical particle physics, we assume that a brain portion can be described by a scalar self-interacting bosonic theory in the stimulus-response space. We simulate a brain portion by considering the relationships between free fields, Gaussian processes and infinite neural networks, and the ones between interacting fields, Non-Gaussian processes

¹ Department of Mathematics, University of Pavia, Pavia, Italy

² Advanced imaging and radiomics center, Neuroradiology Department, IRCCS Mondino Foundation, Pavia, Italy

³ INFN - National Institute of Nuclear Physics, Pavia, Italy

⁴ European Centre for Theoretical Studies in Nuclear Physics and Related Areas (ECT*), I-38123 Villazzano, Trento, Italy

⁵ Fondazione Bruno Kessler (FBK), I-38123 Povo, Trento, Italy

⁶ INFN-TIFPA Trento Institute of Fundamental Physics and Applications, I-38123 Povo, Trento, Italy

⁷ Department of Brain and Behavioral Sciences, University of Pavia, Pavia, Italy

⁸ University of Pavia, Department of Social and Political Science, Pavia, Italy

⁹ BioData Center, IRCCS Mondino Foundation, Pavia, Italy

¹⁰ Department of Physics, University of Pavia, I-27100 Pavia, Pavia, Italy

and finite neural networks. We introduce an *ad-hoc* neural-network activation function inspired by the biological-neuron response function in the case where a brain neuron is modeled as a Resistance-Capacity circuit. We come out with the conclusion that, under the considered conditions, a brain portion can be modeled up to $O(6)$, *i.e.*, six fields interaction, as a Gaussian Process, or rather a quantum free field theory with an *ad-hoc* constructed propagator. Then, the Fourier-transform relation allows us to make quantitative statements in the physical space.

V.1 Introduction

The brain is a complex physical system in constant interaction with the external world. It elaborates and integrates information on the internal and external environment involving spatial structures spanning nine orders of magnitude-scale in ways that have yet to be fully elucidated (Swan, Santos, and Witte 2022).

From an anatomical point of view, the brain is subdivided into the cerebrum, the brainstem and the cerebellum. The cerebrum is in turn divided down the middle into left and right cerebral hemispheres. From a functional point of view, four main areas controlling senses, thoughts and movements, called lobes, can be identified: frontal, parietal, temporal and occipital lobes. The frontal lobe is responsible for the decision-making process, execution of voluntary actions, planning, reasoning, and it is also involved in personality traits. The parietal lobe is implicated in sensory perceptions, whereas the two temporal lobes play a crucial role in storing of memory and auditory processing, emotions and learning. The occipital lobe is responsible for processing visual stimuli. Below the cerebral hemispheres, there are thalamus and hypothalamus which regulate emotions, the behavior and many unconscious body functions. Other basic functions such as consciousness, sleep-awake cycle, respiratory and cardiovascular control are managed by the brainstem. The cerebellum, instead, controls balance, posture, stores learned movements and synchronizes muscle contractions. Both the cerebrum and cerebellum have comparatively thin outer surface layers of gray matter involved in various kinds of computational tasks and larger inner regions of white matter consisting of axons, *i.e.*, long nerve fibers, carrying signals from one part of the brain to another. From a neurophysiological point of view, three areas has been initially distinguished: the ancient brain, the intermediate brain and the recent brain. The ancient brain is connected to instinctive processes, the intermediate brain is involved in emotions whereas the recent brain is the most rational part of the brain responsible for highly information processing. Today the interconnection and interaction

among these areas are studied to determine the functioning of the decision-making process. A deep knowledge of the latter can lead to understanding the mechanisms characteristic of social neuroscience and of economic field, as suggested by neuroeconomics and neuroethics cognitive neuroscience subfields (Camerer, Loewenstein, and Prelec [2004](#)).

Neurons are elementary processing units in the central nervous system. They are connected to each other in an intricate pattern (Gerstner et al. [2014](#)). Functionally speaking, a neuron can be divided into soma, which contains the nucleus of the cell, the axon transmitting the neuron's output signal, and the dendrites, *i.e.*, tree-like structures that extroject from the soma and along which input data are carried into the soma. Signals pass from one neuron to another through the junctions, *i.e.*, synapses, where a synaptic knob (the end of axon's bifurcation) of one neuron is attached to another neuron's soma or dendrites. The axon terminal comes very close to the postsynaptic neuron, leaving only a small gap between pre- and postsynaptic cell membrane called synaptic cleft. Nerve fibers are cylindrical tubes containing a mixed ionic solution of NaCl and KCl. The same kind of ions, but in different concentrations, are present in the surrounding environment. In the resting state, a negative membrane potential of -65mV is established and a different concentration of Na⁺, K⁺, Cl⁻ and proteic anion is maintained inside and outside the nerve fiber.

A signal is actually a region of charge reversal traveling along the fiber: sodium-potassium pump, voltage-gated sodium channels, which are closed at the resting potential, open in response to an initial change in voltage causing the influx of Na⁺ and the depolarization of the cell. Once the depolarization is completed, it leaves the cell membrane potential at +40mV and the voltage-gated sodium ion channels close. The resulting increased positive charge within the cell causes the opening of potassium channels allowing a K⁺ flux outside the membrane, following the electrochemical gradient, with consequent restoring of resting potential.

When the depolarization reaches the synaptic knob, it triggers the emission of vesicles containing neurotransmitters. These chemical substances diffuse into

the synaptic cleft and interact with receptor proteins on receiving neurons causing the opening of ions gate. The ion influx changes the membrane potential at the postsynaptic site so that the chemical signal is translated into an electrical response. The voltage response of a postsynaptic neuron to a presynaptic action potential, or spike, is called postsynaptic potential. The spike on the postsynaptic neuron can reduce the negative polarization of the resting polarization value thus it is an excitatory synapse, whereas it is an inhibitory synapse if the spike increases the negative membrane polarization. The effect of the spike on the membrane can be recorded with an electrode that measures the potential difference between the interior of the cell and its surroundings.

Since networks of nerve cells linked by many mutual connections are capable of non-linear computation (London, Hausser, et al. [2005](#)), *i.e.*, nonlinear summation of information from multiple sources, the brain acts as a non-linear dynamical complex system exhibiting a highly stochastic activity (Rolls and Deco [2010](#)). A widespread idea in neuroscience is that the brain is a computer-like machine performing classical stimulus-response computations. However, recent research shows that non-trivial quantum effects are present in biological systems because of the amplification of the quantum fluctuations due to the interaction with the noisy environment (Jedlicka [2017](#)). The original idea of a deterministic, classic brain is supported by the fact that, as a macroscopic object, the brain presents self-averaging of quantum fluctuations, or rather a decoherence timescales much shorter than the relevant timescales for regular neuron firing and other excitations in microtubules (Tegmark [2000](#)). Therefore, phenomena such as quantum entanglement, superposition or tunneling cannot contribute to its rich and complex dynamics (Koch and Hepp [2006](#)). However, in a non-linear system with high sensitivity, such as the brain, microscopic quantum fluctuations may be amplified: quantum events may influence the activity of the brain (Barr [2001](#) see also Jedlicka [2005](#); Jedlicka [2009](#)) because non-linear chaotic dynamics can amplify lowest-level quantum fluctuations modulating even the large-scale mesoscopic and macroscopic neuronal activity. In addition, non-trivial quantum effects can

accelerate computational processes at the microscopic level in living organisms (Jedlicka [2017]). As reported in Al-Khalili and McFadden [2014], extracellular electrical fields, affected by ion-channel activity, influence the membrane potential of neurons and their spiking activity. These fields are also coupled to quantum coherent events in many neurons, potentially causing synchrony of neural firing. Furthermore, several studies have shown that certain aspects of the decision-making behavior are better described by a quantum-probability framework than a classical one (Mogiliansky, Zamir, and Zwirn [2009], Pothos and Busemeyer [2009], Wang et al. [2014], Yukalov and Sornette [2011]). A quantum treatment of the brain theory is also supported by Penrose's and Nanopoulos works (Hameroff and Penrose [1996] and Nanopoulos [1995]), according to which quantum phenomena are essential for consciousness and occur in cytoskeletal microtubules within brain neurons. Microtubule structure allows organizing cell functioning and processing information, whereas microtubule subunits are coupled to internal quantum events and cooperatively interact with other tubulins. The periodic paracrystalline structure of microtubules makes them able to support a superposition of coherent quantum states for sufficient time needed for efficient quantum computing.

After 20 years of skeptical criticism and many scientist dismissing the quantum idea, "*recent discovery of warm temperature quantum vibrations in microtubules inside brain neurons by the research group led by Anirban Bandyopadhyay suggests that EEG rhythms derive from deeper level microtubule vibrations. In addition, work from the laboratory of Roderick G. Eckenhoff suggests that anesthesia, which selectively erases consciousness while sparing non-conscious brain activities, acts via microtubules in brain neurons.*" (<https://www.elsevier.com/>).

Driven by all these evidences supporting a quantum treatment of the brain, we pursue the goal to introduce a quantum field-theory framework for the brain description in addition to a neural network framework for brain simulation. A very important and significant fact for the construction of our model is that each neuron receives some 10^4 synaptics inputs from the axons of other neurons and that each branching neuron axon forms about the same number of

synaptic contacts on postsynaptic neurons. A closer look at the brain cortex would expose a “*mosaic-type structure of assemblies of a few thousand densely connected neurons*” (Nanopoulos [1995]) considered as the fundamental cortical processing modules, *i.e.*, brain portions with a size of about 1 mm^2 . Moving to larger scale, parallel and integrative processing of local collective behavior are allowed by a neural connectivity that gets much sparser (Nanopoulos [1995]).

Our intent is to formulate a description of a brain portion and its activity with a quantum field theory and deep learning neural network approach. The brain portion can be identified with a cortical processing module, or with interconnected groups of neurons across different cortex layers, with each group sharing similar properties, since the framework that is about to be introduced is valid for different size of brain portion.

V.2 Theory

In order to describe a portion of the brain and its activity, we work in the input-output, or stimulus-response space that mathematically corresponds to a one-dimensional (1D) space. According to functional magnetic resonance imaging (fMRI), during a particular task (Esteban et al. [2020]) different regions of the brain are simultaneously activated. Therefore they share the same activation status. This suggests that we need a 1D bosonic field theory in analogy to nuclear physics in which bosonic particles (an irreducible representation of the Poincaré group (Di Giacomo [1992])) can occupy the same physical state. We assume zero vacuum expectation value. The bosonic field is defined as:

$$\phi(x) : \mathbb{R}^{d_{\text{in}}} \rightarrow \mathbb{R}^{d_{\text{out}}} \quad (\text{V.1})$$

where d_{in} and d_{out} are the dimensions of the input and output space, respectively, that turn out to be both the 1D \mathbb{R} space in our case, and an element x of the input-output space can be thought as a signal intensity, for example the voltage of the brain portion activity measured with Electroenceelography (EEG). We also consider a self-interacting bosonic theory to take into account

the physical and chemical interconnection of brain neurons and regions. A suitable action S for fields with these characteristics can be written as:

$$S[\phi] = S_1 + \int_{-\infty}^{\infty} d^{d_{\text{in}}}x \sum_k g_k O_k \quad (\text{V.2})$$

where $O_k := \phi(x)^k$ and with S_1 defined as:

$$S_1[\phi] = \int d^d\phi(x) (\square + m^2)\phi(x) \quad (\text{V.3})$$

in which $\square := \partial_\mu \partial^\mu = \frac{1}{c^2} \frac{\partial^2}{\partial t^2} - \nabla^2 = \frac{1}{c^2} \frac{\partial^2}{\partial t^2} - \frac{\partial^2}{\partial x^2}$ and m is the mass of the bosonic particle associated to ϕ . In this case m could be thought as the mass parameter of the considered brain portion. A non-equilibrium theory with the action of Eq. (V.2) up to four field interaction is proposed in Nishiyama and Tuszynski (2019) to describe memory formations with a quantum brain dynamics.

S_1 in Eq. (V.2) is the component that takes into account for a quantum free field $\phi(x)$ and essentially it can be considered as the log-likelihood S_{GP} of a Gaussian process (*i.e.* a Gaussian distribution on the function space):

$$S_{\text{GP}} = \frac{1}{2} \int d^{\text{in}}x d^{\text{in}}x' \phi(x) \Xi(x, x') \phi(x') \quad (\text{V.4})$$

with $\Xi(x, x') = K^{-1}(x, x')$ the kernel function, defined by:

$$\int d^{\text{in}}x' K(x, x') \Xi(x, x'') = \delta^{(d_{\text{in}})}(x - x'') \quad (\text{V.5})$$

and $\delta^{(d_{\text{in}})}(x - x'')$ the d_{in} -dimensional Dirac delta function. Eq. (V.2), therefore, describes a non-Gaussian process, with

$$\int d^{d_{\text{in}}}x \sum_k g_k O_k$$

being the terms that take into account the self-interaction, or rather the non-Gaussian corrections to the Gaussian process S_1 . The resulting non-Gaussian process (NGP) generate n -pt correlation functions:

$$G^{(n)}(x_1, \dots, x_n) = \frac{\int d\phi(x_1) \dots \phi(x_n) e^{-S}}{Z_0} \quad (\text{V.6})$$

with $Z_0 = \int d\phi e^{-S}$. The non-Gaussian component can lead to divergent integrals. A way to treat these divergences is to bound the integrals over input

space from below by $-\Lambda$ and above by Λ . Therefore, we can replace $S \rightarrow S_\Lambda$ and the resulting theory is valid in finite regimes, in analogy to scattering theory valid at some momentum scale that should not be valid up arbitrarily to all momenta. In the range of validity of the theory, the coefficient of operators in S must obey to Wilsonian renormalization-group equations (RGEs) obtained by imposing:

$$\frac{dG^{(n)}(x_1, \dots, x_n)}{d\Lambda} = 0. \quad (\text{V.7})$$

V.3 Correspondence between quantum-field theory and neural network

A first attempt to connect Feynman paths with neural networks is reported in Miranker [2006](#). Recent works (Dyer and GurAri [2019](#); J. Halverson, A. Maiti, and K. Stoner [2021](#) and Yaida [2020](#)) have developed a correspondence between neural networks and quantum-field theory. We took inspiration from the Wilsonian effective field theory (EFT) framework introduced in J. Halverson, A. Maiti, and K. Stoner [2021](#). We summarize in this section the main findings of J. Halverson, A. Maiti, and K. Stoner [2021](#). According to that work, it is possible to establish an analogy between a GP with mean $\mu = 0$ and a class of fully-connected randomly initialized neural networks in the infinite width limit ($N \rightarrow \infty$). This correspond to describing neural network outputs, evaluated on fixed inputs, by draws from a multivariate Gaussian distribution. In particular, consider a family of neural network architectures with discrete hyperparameter N and learnable parameters θ initialized as $\theta \approx P(\theta)$

$$f_{\theta, N} : \mathbb{R}^{d_{\text{in}}} \rightarrow \mathbb{R}^{d_{\text{out}}}. \quad (\text{V.8})$$

The parameter distribution and the network architecture together induce an implicit distribution $P(f)$ on the function space from which the neural network is drawn. In the limit $N \rightarrow \infty$, neural network outputs $\{f(x_1), \dots, f(x_k)\}$ evaluated on any fixed set of k inputs $\{x_1, \dots, x_k\}$ are drawn from a multivariate Gaussian distribution $N(\mu = 0, \Xi^{-1})$. Correlation functions between n outputs

are calculated as:

$$G^{(n)}(x_1, \dots, x_n) = \frac{\int df f(x_1) \dots f(x_n) e^{-\frac{1}{2} S_{\text{GP}}}}{Z_{\text{GP},0}} = \frac{\int df f(x_1) \dots f(x_n) e^{-\frac{1}{2} \int d^{d_{\text{in}}} x d^{d_{\text{out}}} y f(x) \Xi(x,y) f(y)}}{Z_{\text{GP},0}} \quad (\text{V.9})$$

with $Z_{\text{GP},0} := \int df e^{-S_{\text{GP}}}$.

Introducing a source term $J(x)$ the partition function of the Gaussian process Z_{GP} , is defined as:

$$Z_{\text{GP}}[J] = \exp\left(\frac{1}{2} \int d^{d_{\text{in}}} x d^{d_{\text{in}}} y J(x) K(x, y) J(y)\right)$$

and the correlation functions can be written as:

$$G_{\text{GP}}^{(n)}(x_1, \dots, x_n) = \left[\left(-\frac{\delta}{\delta J(x_1)} \right) \dots \left(-\frac{\delta}{\delta J(x_n)} \right) Z_{\text{GP}} \right]_{J=0}.$$

The latter can be calculated using Wick contractions and the expression of the kernel $K(x_1, x_2)$, which depends on the specific activation function $\Phi(x)$ of the neural network. The kernel is the analogous of the quantum-field theory Feynman propagator that represents the probability or amplitude of propagation of a particle from one point to another. From the basic properties of Gaussian integrals it follows the possibility to diagrammatically represent $G^{(n)}$ computation with the Feynman diagrams, and to introduce Feynman rules for a diagrammatic-to-analytic mapping (Feynman rules are reported in Appendix B). Due to the Gaussian nature of the Z_{GP} , all diagrams in the diagrammatic expressions for $G_{\text{GP}}^{(n)}(x_1, \dots, x_n)$ are simple connections of pairs of points in space. Therefore, for a free theory, *i.e.*, for the asymptotic limit of a neural network, we have:

$$\begin{aligned} x_1 \text{ --- } x_2 &= G^{(2)}(x_1, x_2) = K(x_1, x_2) \\ \begin{array}{c} x_1 \\ | \\ x_2 \end{array} & \begin{array}{c} x_3 \\ | \\ x_4 \end{array} + \begin{array}{c} x_1 \text{ --- } x_3 \\ \text{---} \\ x_2 \text{ --- } x_4 \end{array} + \begin{array}{c} x_1 \text{ --- } x_3 \\ \diagdown \quad \diagup \\ x_2 \quad x_4 \end{array} = G_{\text{GP}}^{(4)}(x_1, x_2, x_3, x_4) = \\ &= K(x_1, x_2)K(x_3, x_4) + K(x_1, x_3)K(x_2, x_4) + K(x_1, x_4)K(x_2, x_3) \end{aligned}$$

similarly we can calculate the $G_{GP}^{(6)}(x_1, x_2, x_3, x_4, x_5, x_6)$ as:

$$\begin{aligned}
G_{GP}^{(6)}(x_1, x_2, x_3, x_4, x_5, x_6) = & K(x_1, x_2)K(x_3, x_4)K(x_5, x_6) + K(x_1, x_2)K(x_3, x_5)K(x_4, x_6) \\
& + K(x_1, x_2)K(x_3, x_6)K(x_4, x_5) + K(x_1, x_3)K(x_2, x_4)K(x_5, x_6) \\
& + K(x_1, x_3)K(x_2, x_5)K(x_4, x_6) + K(x_1, x_3)K(x_2, x_6)K(x_4, x_5) \\
& + K(x_1, x_4)K(x_2, x_3)K(x_5, x_6) + K(x_1, x_4)K(x_2, x_5)K(x_3, x_6) \\
& + K(x_1, x_4)K(x_2, x_6)K(x_3, x_5) + K(x_1, x_5)K(x_2, x_3)K(x_4, x_6) \\
& + K(x_1, x_5)K(x_2, x_4)K(x_3, x_6) + K(x_1, x_5)K(x_2, x_6)K(x_3, x_4) \\
& + K(x_1, x_6)K(x_2, x_3)K(x_4, x_5) + K(x_1, x_6)K(x_2, x_4)K(x_3, x_5) \\
& + K(x_1, x_6)K(x_2, x_5)K(x_3, x_4)
\end{aligned}$$

For any odd n , $G_{GP}^{(n)}(x_1, \dots, x_n) = 0$ since in the analytic expression of $G_{GP}^{(n)}$ an odd n corresponds to a factor J in every term and after taking the functional J -derivatives, J is set to zero.

Moving to finite networks corresponds to moving from a Gaussian process (GP) to a Non-Gaussian Process (NGP), *i.e.*, to turning on interactions. To verify this through neural network simulation it is defined the quantity:

$$\Delta G^{(n)}(x_1, \dots, x_n) = G^{(n)}(x_1, \dots, x_n) - G_{GP}^{(n)}(x_1, \dots, x_n). \quad (\text{V.10})$$

with $G^{(n)}(x_1, \dots, x_n)$ the experimental evaluation, obtained through a feed-forward neural network and expressed as:

$$G^{(n)}(x_1, \dots, x_n) = \frac{1}{n_{\text{nets}}} \sum_{\alpha \in \text{nets}}^{n_{\text{nets}}} f_{\alpha}(x_1) \dots f_{\alpha}(x_n).$$

Comparing the theoretical computation with the experiments, $\Delta G^{(2)}(x_1, x_2) \rightarrow 0$, that means

$$G^{(2)}(x_1, x_2) = K(x_1, x_2),$$

i.e., the kernel, calculated for each activation function, is an exact measure of the 2-pt correlation function even away from the GP limit. For the 4-pt and 6-pt signals, GP prediction are still good for large network width but no longer

correctly predict the experimental n -pt function at small width. This suggests that finite neural networks can be obtained from an NGP. In the EFT framework the NGP action is

$$S = S_{\text{GP}} + \Delta S \quad (\text{V.11})$$

with $\Delta S = \int d^{d_{\text{in}}} \sum_k g_k O_k$ and O_k the k - fields interaction expressed as $O_k := f(x)^k$, with the field $f(x) : \mathbb{R}^{d_{\text{in}}} \rightarrow \mathbb{R}^{d_{\text{out}}}$ describing in this case a neural network. Since S must be invariant under the transformation $f \rightarrow -f$, because the randomly initialized neural nets f and $-f$ should be on equal footing, the $\Delta S = \int d^{d_{\text{in}}} [\lambda f(x)^4 + \kappa f(x)^6]$, with k considered negligible as demonstrated in Sec. 4 of J. Halverson, A. Maiti, and K. Stoner [\[2021\]](#)

Using this effective action for the NGP, one may compute correlation functions in perturbation theory. The diagrammatic representation of these correlation functions are the following Feynman diagrams at the first order in k and λ in perturbation theory:

$$x_1 \text{ --- } x_2 - \lambda \left[12 x_1 \text{ --- } \text{---} x_2 \right] - k \left[90 x_1 \text{ --- } \text{---} x_2 \right] = G^{(2)}(x_1, x_2)$$

$$3 \left[\begin{array}{c} x_1 \text{ --- } x_2 \\ \text{---} \\ x_3 \text{ --- } x_4 \end{array} \right] - \lambda \left[24 \begin{array}{c} x_1 \text{ --- } x_2 \\ \times \\ x_4 \text{ --- } x_3 \end{array} + 72 \begin{array}{c} x_1 \text{ --- } x_2 \\ \text{---} \\ x_3 \text{ --- } x_4 \end{array} \right] + \\ - k \left[360 \begin{array}{c} x_1 \text{ --- } x_2 \\ \times \\ x_4 \text{ --- } x_3 \end{array} + 540 \begin{array}{c} x_4 \text{ --- } x_2 \\ \text{---} \\ x_1 \text{ --- } x_3 \end{array} \right] = G^{(4)}(x_1, x_2, x_3, x_4)$$

$$15 \left[\begin{array}{c} x_5 \text{ --- } x_6 \\ \text{---} \\ x_3 \text{ --- } x_4 \end{array} \right] - \lambda \left[540 \begin{array}{c} x_5 \text{ --- } x_6 \\ \text{---} \\ x_4 \text{ --- } x_3 \end{array} + 360 \begin{array}{c} x_5 \text{ --- } x_6 \\ \times \\ x_3 \text{ --- } x_4 \end{array} \right] + \\ - k \left[720 \begin{array}{c} x_5 \text{ --- } x_6 \\ \times \\ x_4 \text{ --- } x_3 \end{array} + 4050 \begin{array}{c} x_5 \text{ --- } x_6 \\ \text{---} \\ x_1 \text{ --- } x_3 \end{array} + 5400 \begin{array}{c} x_5 \text{ --- } x_6 \\ \times \\ x_1 \text{ --- } x_3 \end{array} \right] = G^{(6)}(x_1, x_2, x_3, x_4, x_5, x_6)$$

for which it was demonstrated in J. Halverson, A. Maiti, and K. Stoner [2021](#) that $G_{\text{NGP}}^{(2)}(x_1, x_2) = K(x_1, x_2) = G_{\text{GP}}^{(2)}(x_1, x_2)$, which means that $K(x_1, x_2)$ already takes into account the λ - and k - corrections for the $G^{(2)}$ expression.

V.4 Reproducing the behavior of a brain portion using a neural network

Considering the similarity of the analytic expression of the action S associated to Eq. [\(V.11\)](#), referring to neural network, and to Eq. [\(V.2\)](#) referring to a brain portion field, we want to introduce a neural network that reproduce a brain portion.

A portion of a brain that we are trying to describe in a quantum-field theory framework can be thought of as a set of interconnected biological neurons. On the other hand, a neural network, which according to J. Halverson, A. Maiti, and K. Stoner [2021](#) can be described as a quantum field, is made by weighted and interconnected computational units, the neurons. Starting from this correspondence we want to investigate the possibility to construct a neural network that reproduces the behavior of a brain portion. In particular, we are not searching for a one-to-one correspondence between biological neurons present in the brain portion and neurons of the neural network. What we aim to find is a neural network, thought of as a function $f : \mathbb{R}^{d_{\text{in}}} \rightarrow \mathbb{R}^{d_{\text{out}}}$, that operates as a brain portion described by the field in the relation [\(V.1\)](#).

We consider a finite fully-connected feed-forward neural network with a single hidden layer. This architecture, as underlined in Sec. [V.3](#) is well described by a NGP of the same kind of Eq. [\(V.2\)](#) and its behavior in the asymptotic limit is a Gaussian process distribution on function space.

Crucial in the correspondence that we are trying to create is the choice of the activation function. In fact, the latter generates a specific kernel expression, or a Feynman propagator in a quantum field framework, and consequently correlation functions, or rather a specific quantum-field theory.

A generic neural network with activation function $\Phi(x)$ and one hidden layer

has the following output function (J. Halverson, A. Maiti, and K. Stoner [2021](#)):

$$f(x) = W_1 \Phi(W_0 x + b_0) + b_1$$

with W_0, W_1, b_0, b_1 i.i.d. and drawn from a Gaussian distribution with mean 0 and standard deviations $\sigma_{W_0}, \sigma_{W_1}, \sigma_{b_0}, \sigma_{b_1}$ respectively. The kernel or 2-pt function is calculated, according to Williams [1996](#) by

$$K(x, x') = \mathbb{E}[f(x), f(x')] = \sigma_{b_1}^2 + \sigma_{W_1}^2 V_{\Phi}' [\Phi(W_0 x + b_0), \Phi(W_0 x' + b_0)] \quad (\text{V.12})$$

with

$$V_{\Phi}'(x, x') = \frac{\int \Phi(W_0 x + b_0) \Phi(W_0 x' + b_0) e^{-\frac{1}{2} W_0^T \sigma_{W_0}^{-2} W_0 - \frac{1}{2} b_0^T \sigma_{b_0}^{-2} b_0} dW_0 db_0}{\int \exp\left(-\frac{1}{2} W_0^T \sigma_{W_0}^{-2} W_0 - \frac{1}{2} b_0^T \sigma_{b_0}^{-2} b_0\right) dW_0 db_0} \quad (\text{V.13})$$

To identify the activation function Φ we start modeling the membrane potential of integrate-and-fire neuron (*i.e.* a neuron model where action potentials are considered events completely characterized by an equation describing the evolution of membrane potential and a mechanism to generate spike (Gerstner et al. [2014](#))), and using a hardware circuit that consists of a resistance R and a capacitor C . Inspired by the calculation reported in Amemori and Ishii [2001](#) we define the activation function as:

$$\Phi(x) = \frac{q(e^{-\alpha x} - e^{-\beta x})}{\sqrt{K(x, x)}} \quad (\text{V.14})$$

with $\alpha = \frac{1}{\tau_m}$, that according to Amemori and Ishii [2001](#) is set to $0.1(\frac{1}{ms})$, $\beta = \frac{1}{\tau_s}$ with τ_s the synaptic time constant, $q = \frac{\beta}{(\beta - \alpha)}$ (we chose $\beta = [1.2 - 1.8]$ compatible with the range of values reported in Amemori and Ishii [2001](#)) and

$$K(x, x) = q^2 \left(e^{2\alpha^2(\sigma_{b_0}^2 + \sigma_{W_0}^2 x^2)} + e^{2\beta^2(\sigma_{b_0}^2 + \sigma_{W_0}^2 x^2)} - 2e^{\frac{1}{2}(\alpha + \beta)^2(\sigma_{b_0}^2 + \sigma_{W_0}^2 x^2)} \right).$$

The numerator of the activation function defined in Eq. [\(V.14\)](#) is the analogue in the 1D-space introduced in Sec. [V.2](#) of the "spike response function" defined in Amemori and Ishii [2001](#) that characterizes the biological neuron membrane response to a single input spike.

Substituting the activation function of Eq. [\(V.14\)](#) in the expression [\(V.13\)](#) we obtain

$$V'_{\Phi}(x, x') = \frac{e^{\frac{1}{2}\alpha^2(4\sigma_{b_0}^2 + (x+x')^2\sigma_{W_0}^2)} + e^{\frac{1}{2}\beta^2(4\sigma_{b_0}^2 + (x+x')^2\sigma_{W_0}^2)}}{AB} + \quad (\text{V.15})$$

$$+ \frac{-e^{\frac{1}{2}(\alpha+\beta)^2\sigma_{b_0}^2 + (x'\alpha+x\beta)^2\sigma_{W_0}^2} - e^{\frac{1}{2}(\alpha+\beta)^2\sigma_{b_0}^2 + (x\alpha+x'\beta)^2\sigma_{W_0}^2}}{AB}, \quad (\text{V.16})$$

with

$$A = \sqrt{e^{2\alpha^2(\sigma_{b_0}^2 + x^2\sigma_{W_0}^2)} + e^{2\beta^2\left(\sigma_{b_0}^2 + x^2\sigma_{W_0}^2 - 2e^{\frac{1}{2}(\alpha+\beta)(\sigma_{b_0}^2 + x\sigma_{W_0}^2)}\right)}} \quad (\text{V.17})$$

and

$$B = \sqrt{e^{2\alpha^2(\sigma_{b_0}^2 + x'^2\sigma_{W_0}^2)} + e^{2\beta^2\left(\sigma_{b_0}^2 + x'^2\sigma_{W_0}^2 - 2e^{\frac{1}{2}(\alpha+\beta)(\sigma_{b_0}^2 + x'\sigma_{W_0}^2)}\right)}}. \quad (\text{V.18})$$

The latter expression substituted in Eq. (V.12) gives the corresponding propagator.

In order to investigate the possibility of a translation invariant theory, we also studied the limit $\beta \rightarrow \infty$ for which the activation function is:

$$\Phi(x) = \frac{qe^{-\alpha x}}{\sqrt{K(x, x)}} \quad (\text{V.19})$$

with $q = 1$ as reported in Amemori and Ishii [2001] and $K(x, x) = q^2 e^{2\alpha^2\sigma_{W_0}^2 x^2 + 2\alpha^2\sigma_{b_0}^2}$. Substituting the activation function of Eq. (V.19) in (V.13) we have:

$$V'_{\Phi}(x, x') = e^{-\frac{1}{2}\alpha^2\sigma_{W_0}^2(x-x')^2} \quad (\text{V.20})$$

and then putting the latter expression in (V.12) we obtain the propagator:

$$K(x, x') = \sigma_{b_1}^2 + \sigma_{W_1}^2 e^{-\frac{1}{2}\alpha^2\sigma_{W_0}^2|x-x'|^2}.$$

This expression turns also to be invariant under the translation map $x \rightarrow x + c$, $x' \rightarrow x' + c$. Thus, the associated theory has also to show this symmetry.

The next step is to analyze the network behavior with the activation functions defined in Eq. (V.19) and in Eq. (V.14). To do this, we need to

find appropriate inputs for the network and to modify the open-source code at <https://github.com/keeganstoner/nn-qft> (James Halverson, Anindita Maiti, and Keegan Stoner [2021], James Halverson, Anindita Maiti, and Keegan Stoner [2020]) introducing the definition of the new activation functions and of the derived propagators.

V.4.1 Input creation

The idea underlying the creation of inputs is that we are not interested in reproducing spikes of individual neurons but in describing the response of interconnected neuronal populations as a whole and even distributed in different cortical layer, once the properties of each neurons' population and the network connectivity are known. A neuronal population has to be intended as an homogeneous group of neurons with similar intrinsic properties and similar receptive fields (Gerstner et al. [2014]). More generally, the mathematical notion of population does not necessarily imply a local group of neurons: a neuronal assembly (Hebb [1949]), in fact, is composed of a network of neurons involved in the same stimuli response and which can even be distributed in several brain areas. Neurons of a certain population can interact among themselves and with neurons of different populations and of different cortical layers, even of different brain areas.

To obtain the input, we refer to Bos, Diesmann, and Helias [2016] where a combination of mean-field (Amit, Brunel, et al. [1997]) and linear-response theory is used to predict the spectra generated in a layered microcircuit. The latter models a multi-layered spiking cortical network as composed of four layers of excitatory and four layers of inhibitory neurons' populations, according to the balanced random network model introduced in Amit, Brunel, et al. [1997] with a data-based cell-type specific connectivity as proposed by Potjans and Diesmann [2014]. For a graphical representation see Fig. [V.1]

We use the toolbox described in Layer et al. [2022] to obtain how the layered microcircuit power signal is distributed across its different frequency

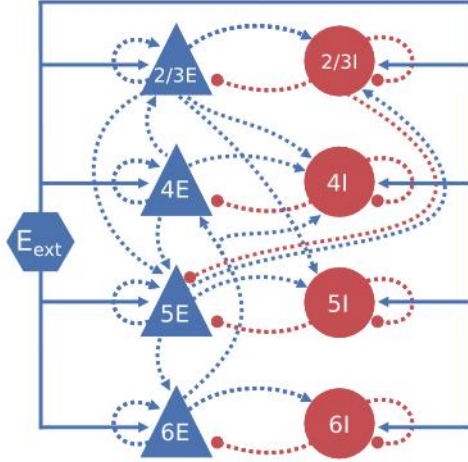


Figure V.1: Example of cortical layered microcircuit consisting of four layers of excitatory neurons' population (E) and four layers of inhibitory neurons' population (I). Image from Layer et al. [2022](#)

components. This toolbox implements mean-field approximation of neuronal activity and the power spectra are obtained by studying the linear response of the network activity to fluctuations caused by its spiking activity, as reported in Bos, Diesmann, and Helias [2016](#). The numerical predictions obtained with this toolbox reproduce the simulated data presented in Bos, Diesmann, and Helias [2016](#).

Once we obtain the power spectra of each population, we calculate the associated signal intensity using the Parseval relation, which allows the calculation of the norm of a Fourier series. Therefore the generated inputs, referring to the signal intensity of the four layers of excitatory neurons' population and of the four layers of inhibitory neurons' population, are:

$$\{0.0143, 0.0702, 0.2028, 0.3972, 0.6535, 1.0201, 0.0335, 0.9587\} \quad (\text{V.21})$$

V.4.2 Study of the network behavior

In this section we use the generated inputs to study the network behavior considering the two defined activation functions, the activation function 1

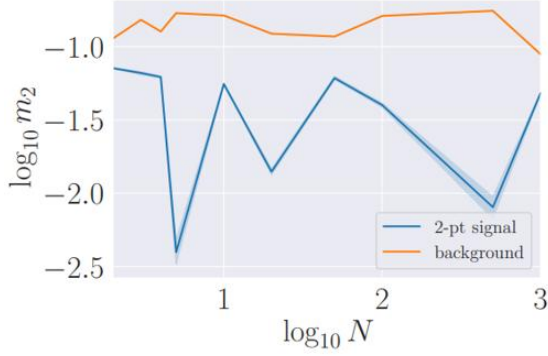
expressed by Eq. (V.19) and the activation function 2 by Eq. (V.14).

V.4.2.1 Study with activation function 1

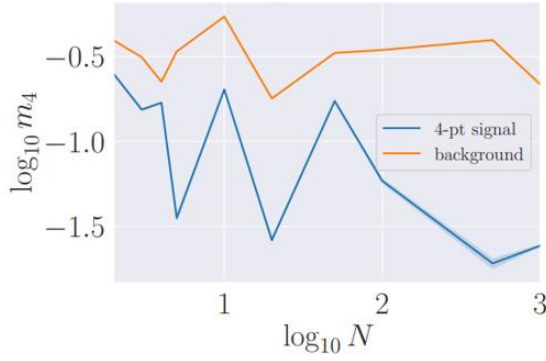
Fig V.2 shows the 2-pt, 4-pt and 6-pt deviation defined as $m_n = \frac{\Delta G^{(n)}}{G_{GP^{(n)}}}$ with respect to a background signal, the average element-wise standard deviation of the experimental m_n as reported in J. Halverson, A. Maiti, and K. Stoner [2021]. We can observe that the n-pt deviations are below the background level and therefore consistent with $\Delta G^{(n)} \rightarrow 0$ indicating that the kernel is an exact measure of the n-pt correlation function even away from the infinite neural network limit, or rather away from GP limit, as reported in J. Halverson, A. Maiti, and K. Stoner [2021]. This means that GP prediction still correctly reproduce the experimental n-pt functions; thus the neural networks can be considered as drawn from a GP or rather the neural network with the activation function 1, approximating the behavior of a brain portion, can be described as a Gaussian Process up to O(6). As a consequence, the network statistics constructed in this way is entirely determined by Wick contractions of the kernel $K(x, x')$ calculated in Sec. V.4

V.4.2.2 Study with activation function 2

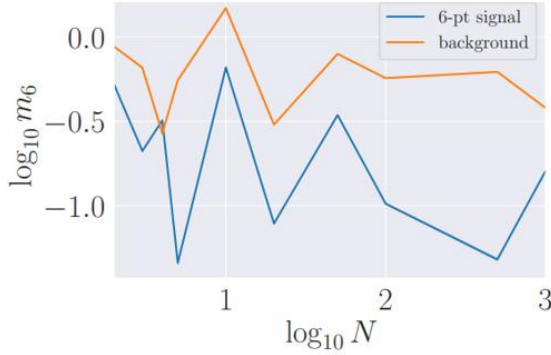
From Fig. V.3, related to inputs defined in (V.21), we can see that the correlation function $G^{(2)}$ has some small fluctuations upon the level of the background signal. However, considering correlation functions $G^{(4)}$ and $G^{(6)}$ we can see that the behavior of the network with activation function 2 is well approximated up to O(6) with a Gaussian process when $\beta = [1.2, 1.8]$ (a range compatible with values reported in Amemori and Ishii [2001]). For different β values (compatible with Amemori and Ishii [2001], *e.g.*, in the range [2., 3.]) we have the n-pt deviation signal above the background level. This means that GP prediction no longer correctly predicts the experimental n-pt function or rather the neural network is not drawn from a GP, but instead from an NGP.



(a) 2 - pt deviation



(b) 4 - pt deviation



(c) 6 - pt deviation

Figure V.2: n -pt deviation calculated as [\(V.10\)](#) normalized for $G_{GP}^{(n)}$ and generated by the activation function 1. Signal represents element of the tensor $m_n = \frac{\Delta G^n}{G_{GP}^n}$ and the background the average element-wise standard deviation. The experiment is done with 10^3 networks for a run and inputs defined in [\(V.21\)](#).

The theory framework is still valid also in this case, as reported in Appendix A, and it will be further investigated in future works.

V.4.3 Stability studies of the network behavior

To study the stability of the network behavior, we also consider the inputs related to the sub-circuit, or the so-called minimal circuit described in Bos, Diesmann, and Helias [2016]. The minimal circuit corresponds to the anatomical circuit underlying the generation of low (64 Hz)- and high- γ oscillations. These oscillations are present in neural population signals, like multi-unit recordings EEG/MEG.

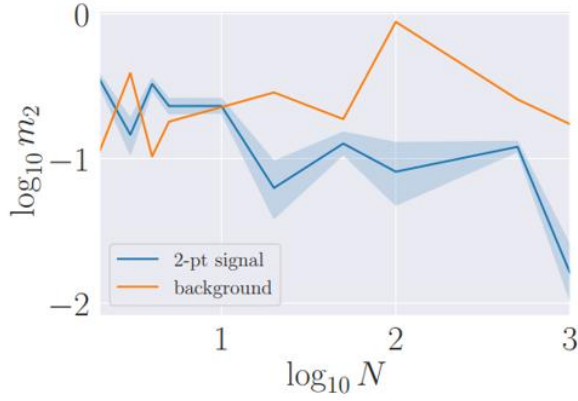
With reference to Fig. [V.1] and as reported in Bos, Diesmann, and Helias [2016], the low- and high- γ oscillation turns out to be generated in a sub-circuit located in layer 2/3E and 4E and 4I.

Power spectra associated to the tree populations in sub-circuit are derived with toolbox Layer et al. [2022] and, using again the Parseval identity, the associated signal intensity are obtained. Inputs generated in this way are:

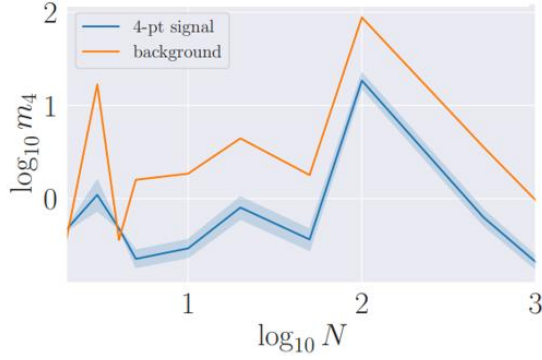
$$\{0.0143, 0.2028, 0.3972\}. \quad (\text{V.22})$$

The obtained results for the activation function 1 are reported in Fig. [V.4] whereas the results for the activation function 2 are shown Fig. [V.5]. They all confirm that the neural network with the activation functions 1 and 2, can be described as a Gaussian Process up to $O(6)$. Besides, the obtained behaviors are further supported by the results generated considering 10 runs for each of the 10^3 models (different network initialization) and inputs given by Eq. ([V.21]) and Eq. ([V.22]) for activation function 1 (Fig. [V.6] and Fig. [V.7]) and for activation function 2 (Fig. [V.8] and Fig. [V.9]).

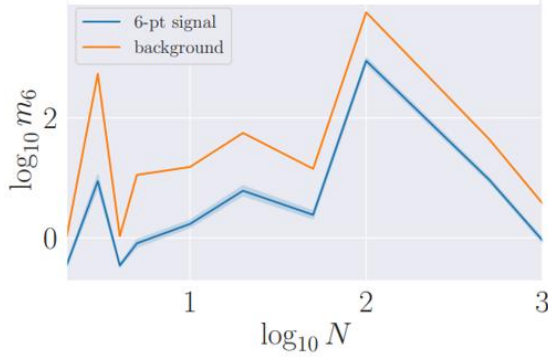
From the studies presented, we can conclude that, unlike the finite neural networks with different activation functions presented in J. Halverson, A. Maiti, and K. Stoner [2021], the neural network $f(x) : \mathbb{R}^{d_{\text{in}}} \rightarrow \mathbb{R}^{d_{\text{out}}}$ constructed to behave as a brain portion can be described up to the $O(6)$ as a Gaussian process. More in detail, we are referring to a neural network with one of the



(a) 2 – pt deviation

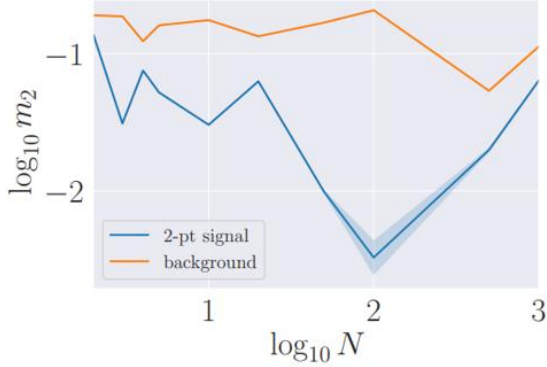


(b) 4 – pt deviation

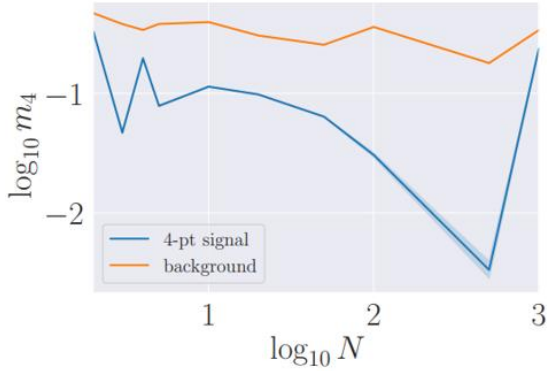


(c) 6 – pt deviation

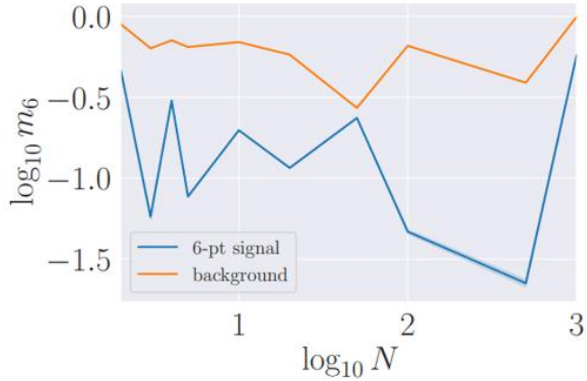
Figure V.3: n -pt deviation calculated as (V.10) normalized for $G_{GP}^{(n)}$ and generated by the activation function 2. Signal represents element of the tensor $m_n = \frac{\Delta G^n}{G_{GP}^n}$ and the background the average element-wise standard deviation. The experiment is done with 10^3 networks for a run and inputs defined in (V.21) and $\beta = 1.8$.



(a) 2-pt deviation

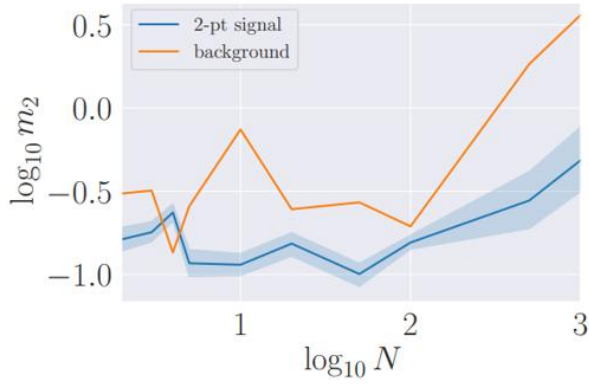


(b) 4-pt deviation

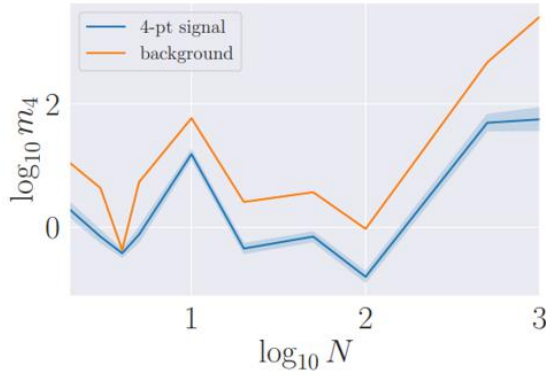


(c) 6-pt deviation

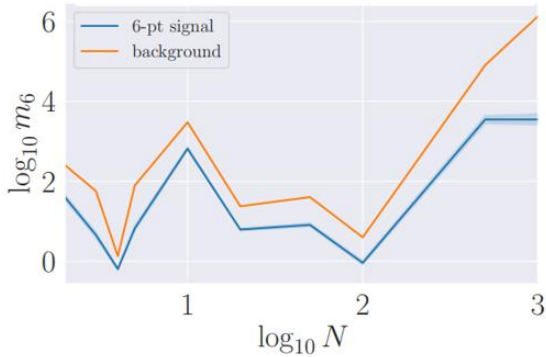
Figure V.4: n -pt deviation calculated as [\(V.10\)](#) normalized for $G_{GP}^{(n)}$ and generated by the activation function 1. Signal represents element of the tensor $m_n = \frac{\Delta G^n}{G_{GP}^n}$ and the background the average element-wise standard deviation. The experiment is done with 10^3 networks for a run and inputs defined in [\(V.22\)](#).



(a) 2 – pt deviation

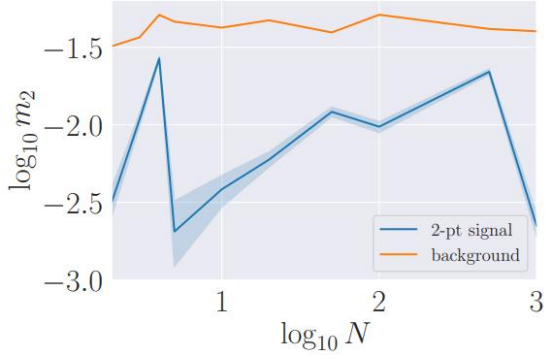


(b) 4 – pt deviation

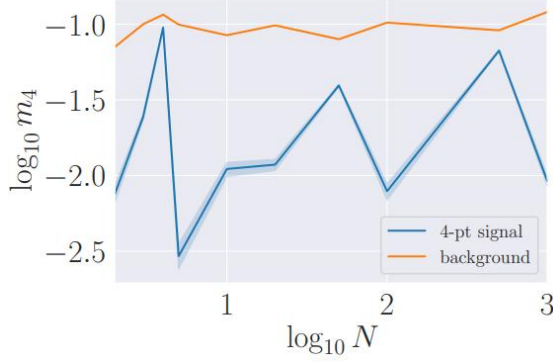


(c) 6 – pt deviation

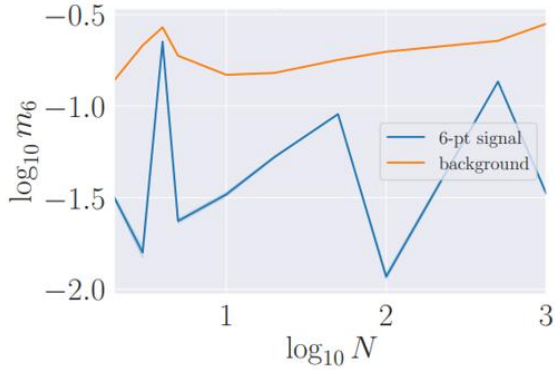
Figure V.5: n -pt deviation calculated as (V.10) normalized for $G_{GP}^{(n)}$ and generated by the activation function 2. Signal represents element of the tensor $m_n = \frac{\Delta G^n}{G_{GP}^n}$ and the background the average element-wise standard deviation. The experiment is done with 10^3 networks for a run and inputs defined in (V.22) and $\beta = 1.8$.



(a) 2-pt deviation

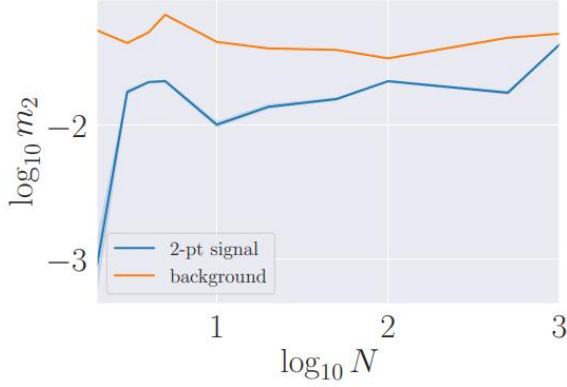


(b) 4-pt deviation

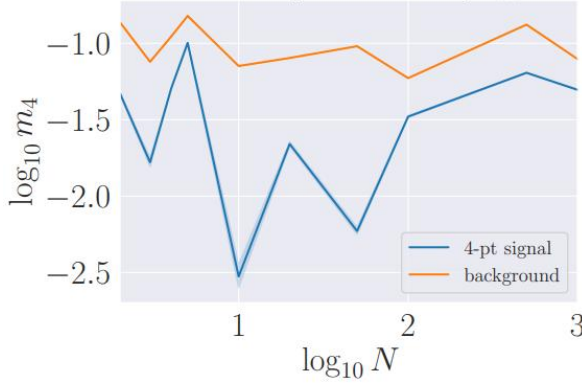


(c) 6-pt deviation

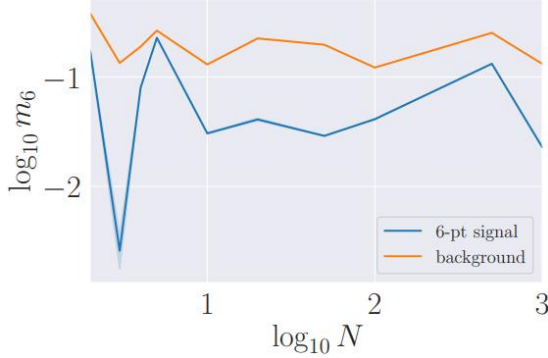
Figure V.6: n -pt deviation calculated as (V.10) normalized for $G_{GP}^{(n)}$ and generated by the activation function 1. Signal represents element of the tensor $m_n = \frac{\Delta G^n}{G_{GP}^n}$ and the background the average element-wise standard deviation. The experiment is done with 10^3 networks for 10 run and inputs defined in (V.21)



(a) 2 - pt deviation

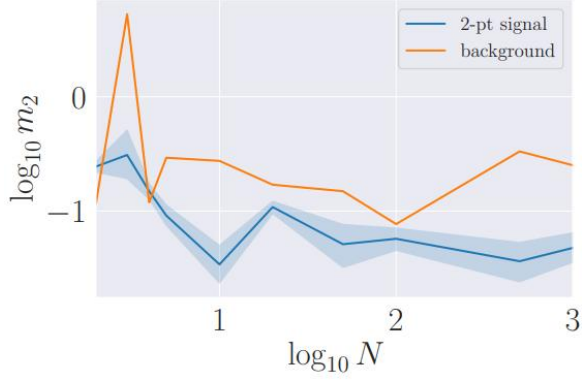


(b) 4 - pt deviation

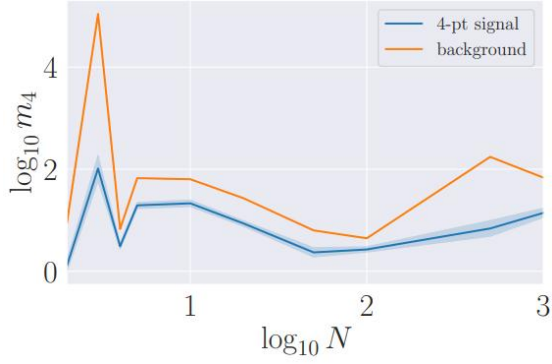


(c) 6 - pt deviation

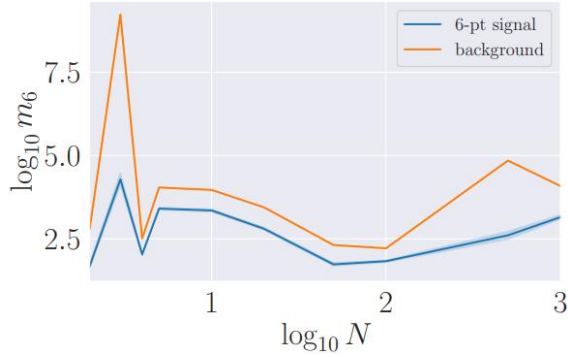
Figure V.7: n -pt deviation calculated as [\(V.10\)](#) normalized for $G_{GP}^{(n)}$ and generated by the activation function 1. Signal represents element of the tensor $m_n = \frac{\Delta G^n}{G_{GP}^n}$ and the background the average element-wise standard deviation. The experiment is done with 10^3 networks for 10 run and inputs defined in [\(V.22\)](#).



(a) 2-pt deviation

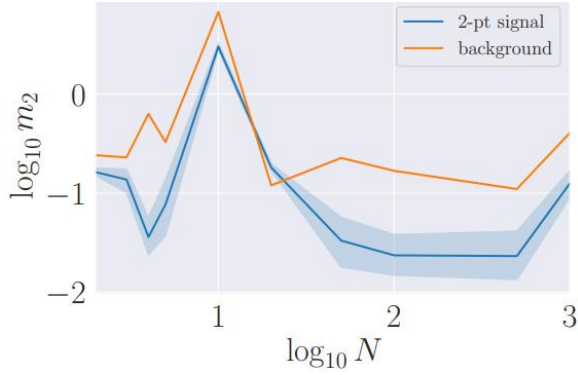


(b) 4-pt deviation

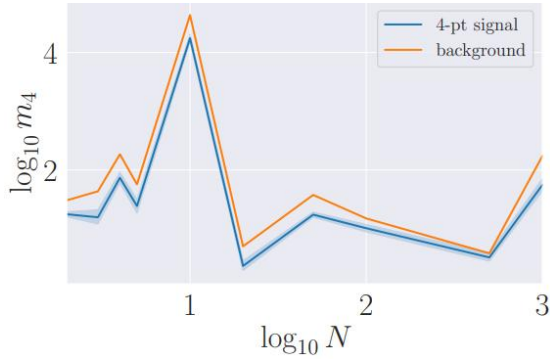


(c) 6-pt deviation

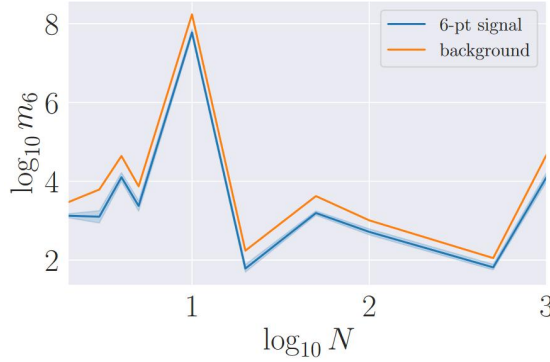
Figure V.8: n -pt deviation calculated as (V.10) normalized for $G_{GP}^{(n)}$ and generated by the activation function 2. Signal represents element of the tensor $m_n = \frac{\Delta G^n}{G_{GP}^n}$ and the background the average element-wise standard deviation. The experiment is done with 10^3 networks for 10 run and inputs defined in (V.21).



(a) 2 - pt deviation



(b) 4 - pt deviation



(c) 6 - pt deviation

Figure V.9: n -pt deviation calculated as (V.10) normalized for $G_{GP}^{(n)}$ and generated by the activation function 2. Signal represents element of the tensor $m_n = \frac{\Delta G^n}{G_{GP}^n}$ and the background the average element-wise standard deviation. The experiment is done with 10^3 networks for 10 run and inputs defined in (V.22).

defined activation functions of the type 1, 2 and receiving as inputs the vectors designed to reproduce the signal associated to the mean field power spectra approximation of the neural excitation and inhibition populations of the cortical layer. Therefore, a brain portion field expressed in (V.1) can be considered as a Gaussian Process on function space.

V.5 From the signal space to physical space

As shown in the previous section the behavior of a brain portion, represented through a finite neural network, can be modeled as a Gaussian process on function space $\phi : \mathbb{R} \rightarrow \mathbb{R}$. This means that the neural-signal intensity is drawn from a multivariate Gaussian distribution $\mathcal{N}(\mu, \Xi^{-1})$ (J. Halverson, A. Maiti, and K. Stoner 2021). For assumption in the model construction $\mu = 0$ whereas the covariance Ξ is the inverse of the Kernel function $K(x, x')$ which, in turn, incorporate the biological information of the neuronal model. Therefore, we have:

$$\phi(x) \sim e^{-\frac{1}{2}x\Xi^{-1}x} \quad (\text{V.23})$$

with $x \in \mathbb{R}$, the signal intensity space and Ξ^{-1} the propagator. To pass from the signal space to physical space $r \in \mathbb{R}$, we can take advantage of the Fourier transform. A Fourier transform of a Gaussian field is still a Gaussian field. Thus, in the physical space we have:

$$\phi(r) \sim e^{-\frac{r^2}{2\Xi^{-1}}} \int_{-\infty}^{+\infty} e^{-\frac{(\sqrt{\Xi^{-1}}x + \frac{ix}{\sqrt{\Xi^{-1}}})^2}{2}} dx = e^{-\frac{r^2}{2\Xi^{-1}}} C(\Xi^{-1}) \quad (\text{V.24})$$

with $C(\Xi^{-1}) = \sqrt{\frac{\pi}{2\Xi^{-1}}}$ a coefficient that depends on Ξ and so on the propagator. The derived distribution can be thought as the field describing the spatial influence of a brain portion centered in the position r .

An approach to experimentally obtain a high temporal-resolution signal of the neural activity in a certain region of the brain immediately surrounding the recording surface of an electrode, is the electroencephalography (EEG) technique. However, as reported in Owen et al. 2020, brain regions that are distant from the recording surface of the electrode also contribute to the recorded

signal, due to brain volume conduction but also to direct and indirect anatomical connections. In Owen et al. [2020] the behavior of how much a small volume of brain tissue at the location z contribute to the recording from an electrode at location η is approximated by a Gaussian radial-basis function (rbf):

$$rbf = e^{-\frac{\|x-\eta\|^2}{\lambda}} \quad (\text{V.25})$$

with λ a parameter that governs the level of spatial smoothing. The estimated values of the rbf at any brain location z can be used as a rough estimate of how much structures around z contribute to the recording from the location η . Thus, the rbf can take into account how informative the recordings at each electrode location is in reconstructing activity at each other brain position. In this way, as reported in Owen et al. [2020], one can construct a matrix to be used as a weight for the observed interelectrode correlation matrix of a certain patients and then to aggregate these estimates across all the available patient to obtain a single full-brain correlation matrix. By doing so, the authors of Owen et al. [2020] were able to estimate the voltage from different patients in different brain locations.

In this context, we can recognize that the rbf has the same role of the field distribution in (V.24), in which r is interpreted as the spatial distance $\|z - \eta\|$. We can take advantage of this connection to experimentally calibrate the constants value in the expression of the propagator K , which incorporate the model biological information. In particular, we can match

$$e^{-\frac{r^2}{2\Xi^{-1}}} \sqrt{\frac{\pi}{2\Xi}} = e^{-\frac{r^2}{\lambda}} \quad (\text{V.26})$$

with λ obtained from healthy control EEG data through an optimization problem on EEG similar to the one reported in Owen et al. [2020]. We can then solve for Ξ^{-1} that is:

$$K = \Xi^{-1} = -\frac{1}{W(-e^{-A})} \quad (\text{V.27})$$

with $A = -\frac{1}{\lambda} + \ln \frac{1}{\sqrt{\pi}}$ and W is the Lambert function (Mező and Keady [2016]). The biological implication of this result will be the object of future investigation.

V.6 Conclusion and future perspectives

We introduced an attempt to describe a brain portion through a quantum-field theory. Thanks to the connection between quantum-field theory and neural network pointed out in Halverson et. al. J. Halverson, A. Maiti, and K. Stoner [2021] we constructed a finite neural network characterized by an activation function inspired to a biological neuron model response function with the aim to simulate the brain portion. We studied the behavior of the defined neural network considering as input the mean field approximation of the power spectra associated to the multi-layered spiking cortical neurons' populations. We obtained that the brain portion activity can be approximated up to $O(6)$, *i.e.*, six fields interaction, as a Gaussian Process. A quantum-field theory description is also possible in the case in which the network behavior could result in a non-Gaussian Process as reported in the Appendix A. This quantum description of the brain can pave the way for a future study on quantum effects in the brain. It also gives the possibility to simulate the behavior of a brain portion incorporating the biological modeling of a neuron [1] and in addition, in theory, having available many fMRI data or EEG data, to train the network to reproduce neural data. In this context, we can also consider that different brain portions can be simulated separately and then connected, with a connectivity determined by correlation matrix as usual in connectomics (Behrens and Sporns [2012]), to reproduce the full-brain activity.

As a future application, we plan to extend this model in more dimensions, *e.g.*, a 3D space, by considering not just real scalar bosons but complex scalar bosons or even some analogue of the particles with spin.

¹A potential advantage of the proposed brain simulator based on QFT and NN respect to other brain simulators is that it is no longer necessary to distinguish between the top-down and bottom-up approach. In fact, the brain model based on QFT and NN directly incorporates the biological information at microscopic level in the chosen activation function. The QFT-NN model is also easily adaptable to different biological modeling of a single neuron, which is translatable into a change of activation function and of the corresponding Feynman propagator. Computationally speaking, the NN approach is also fast, once the models with a defined activation function and associated propagator are generated.

Appendix A

The developed theory is still valid in the case in which the constructed neural network with a particular activation function, modeling the response of the biological neuron, behaves as a non-Gaussian Process. In this case, we have an action S_{NGP} of the type reported in Eq. (V.2) and to calculate the n-pt correlation function we need to consider, as reported in J. Halverson, A. Maiti, and K. Stoner [2021](#), that:

$$G^{(2)}(x_1, x_2) \neq K(x_1, x_2) = G_{GP}^{(2)}(x_1, x_2) \quad (\text{V.28})$$

and so

$$G^{(2)}(x_1, x_2) = K(x_1, x_2) + \lambda\text{-, k-corrrections} \quad (\text{V.29})$$

and therefore:

$$\begin{aligned}
 & x_1 \text{ --- } x_2 - \lambda \left[12 \ x_1 \text{ --- } \overline{\text{O}} \ x_2 \right] - k \left[90 \ x_1 \text{ --- } \overline{\text{O}} \ x_2 \right] = G^{(2)}(x_1, x_2) \\
 \\
 & 3 \left[\begin{array}{c} x_1 \text{ --- } x_2 \\ \text{---} \\ x_3 \text{ --- } x_4 \end{array} \right] - \lambda \left[24 \begin{array}{c} x_1 \quad x_2 \\ \quad \times \\ x_4 \quad x_3 \end{array} + 72 \begin{array}{c} x_1 \quad x_2 \\ \quad \overline{\text{O}} \\ x_3 \quad x_4 \end{array} \right] + \\
 & \quad - k \left[360 \begin{array}{c} x_1 \quad x_2 \\ \quad \times \\ x_4 \quad x_3 \end{array} + 540 \begin{array}{c} x_4 \quad x_2 \\ \quad \overline{\text{O}} \\ x_1 \quad x_3 \end{array} \right] = G^{(4)}(x_1, x_2, x_3, x_4) \\
 \\
 & 15 \left[\begin{array}{c} x_5 \quad x_6 \\ \text{---} \\ x_1 \text{ ---} x_2 \\ \text{---} \\ x_3 \quad x_4 \end{array} \right] - \lambda \left[540 \begin{array}{c} x_5 \quad x_6 \\ \quad \overline{\text{O}} \\ x_4 \quad x_3 \end{array} + 360 \begin{array}{c} x_5 \quad x_6 \\ \quad \times \\ x_3 \quad x_4 \end{array} \right] + \\
 & \quad - k \left[720 \begin{array}{c} x_5 \quad x_6 \\ \quad \times \\ x_4 \quad x_3 \end{array} + 4050 \begin{array}{c} x_5 \quad x_6 \\ \quad \overline{\text{O}} \\ x_1 \quad x_3 \end{array} + 5400 \begin{array}{c} x_5 \quad x_6 \\ \quad \times \\ x_1 \quad x_3 \end{array} \right] = G^{(6)}(x_1, x_2, x_3, x_4, x_5, x_6)
 \end{aligned}$$

Proceeding as in J. Halverson, A. Maiti, and K. Stoner [2021] we consider that the kernels associated to a class of neural network architectures can be expressed in terms of a model independent (within the architecture class) term α and a model dependent term ξ :

$$K(x, x') = \alpha + \xi(x, x') \quad (\text{V.30})$$

where it is assumed that the first and the second terms are input independent and dependent, respectively in deep fully-connected networks (J. Halverson, A. Maiti, and K. Stoner [2021]). Substituting the kernel expressed by the Eq. (V.30) in the mathematical transcription of the Feynman graph for $G^{(4)}$ and $G^{(6)}$ we obtain

$$G^{(4)}(x_1, x_2, x_3, x_4) = \gamma_{4,0} + \rho_{4,0} - \lambda \int_{-\Lambda}^{\Lambda} d^{d_{in}} x (\gamma_{4,\lambda} + \rho_{4,\lambda}) - k \int_{-\Lambda}^{\Lambda} d^{d_{in}} x (\lambda_{4,k} + \rho_{4,k}) \quad (\text{V.31})$$

and similarly for $G^{(6)}$:

$$G^{(6)}(x_1, x_2, x_3, x_4, x_5, x_6) = \gamma_{6,0} + \rho_{6,0} - \lambda \int_{-\Lambda}^{\Lambda} d^{d_{in}} x (\gamma_{6,\lambda} + \rho_{6,\lambda}) - k \int_{-\Lambda}^{\Lambda} d^{d_{in}} x (\lambda_{6,k} + \rho_{6,k}) \quad (\text{V.32})$$

with the subscripts 4 and 6 representing the order of the corresponding correlation function. Terms $\lambda_{6,0}$ and $\rho_{6,0}$ are independent of the integration variable x and of any interaction vertices. The renormalization group equations (RGs) are :

$$\frac{\partial G^{(4)}(x_1, x_2, x_3, x_4)}{\partial \log \Lambda} = 0$$

and

$$\frac{\partial G^{(6)}(x_1, x_2, x_3, x_4, x_5, x_6)}{\partial \log \Lambda} = 0$$

and in the limit of large Λ , k term is negligible.

In this case we can estimate the parameter λ as:

$$\lambda = \frac{N}{D} \quad (\text{V.33})$$

where N is defined as:

$$x_1 \text{ --- } x_2 \quad - \quad G^{(2)}(x_1, x_2) = K(x_1, x_2)$$

with $G^{(2)}(x_1, x_2)$ the experimental evaluation of the 2-pt function according to the relation in Eq. (V.3), whereas D is:

$$\left[12 \ x_1 \ \underline{0} \ x_2 \right].$$

We can use then the derived λ to make prediction in $G^{(4)}$ and $G^{(6)}$.

Appendix B

We report, according to J. Halverson, A. Maiti, and K. Stoner [2021] the more general Feynman rules, whose particular expression depend on the action S :

- 1) For each of the n external points x_i , draw:

$$x_1 \text{ ---}$$

- 2) for each interaction vertices y_j and z_m , draw respectively:



and



- 3) Determine all ways to pair up the loose ends associated to x'_i s, y'_j s and z'_k s. This will yield some number of topologically distant diagrams.

- 4) Write a sum over the diagrams with an appropriate combinatorial factor out front, which is the number of ways to form that diagram. Each diagram corresponds to an analytic term in the sum.

5) For each diagram, write $-\int d^{d_{in}} y_j \lambda$ for each



, and $-\int d^{d_{in}} z_k k$ for each



6) Write $K(u, v)$ for each



7) Throw away any terms containing vacuum bubbles (or rather a diagram that is not connected to any external points.)

References

- Amemori, K. and Ishii, S. (2001). “Gaussian process approach to spiking neurons for inhomogeneous Poisson inputs”. In: *Neural computation* vol. 13, no. 12, pp. 2763–2797.
- Amit, D. J., Brunel, N., et al. (1997). “Global spontaneous activity and local structured (learned) delay period activity in cortex”. In: *Cerebral Cortex* vol. 7, pp. 237–252.
- Barr, S. M. (2001). “The Quantum Brain: The Search for Freedom and the Next Generation of Man.(Books in review: matter, life, and soul)”. In: *First Things: A Monthly Journal of Religion and Public Life*, pp. 43–47.
- Behrens, T. E.J. and Sporns, O. (2012). “Human connectomics”. In: *Current opinion in neurobiology* vol. 22, no. 1, pp. 144–153.
- Bos, H., Diesmann, M., and Helias, M. (2016). “Identifying anatomical origins of coexisting oscillations in the cortical microcircuit”. In: *PLoS computational biology* vol. 12, no. 10, e1005132.

- Camerer, Colin, Loewenstein, George, and Prelec, Drazen (2004). “Neuroeconomics, ovvero come le neuroscienze possono dare nuova forma all’economia”. In: *Sistemi intelligenti* vol. 16, no. 3, pp. 337–418.
- Di Giacomo, A. (1992). *Lezioni di Fisica Teorica*. ETS.
- Dyer, E. and GurAri, G. (2019). “Asymptotics of wide networks from feynman diagrams”. In: *arXiv preprint arXiv:1909.11304*.
- Esteban, O. et al. (2020). “Analysis of task-based functional MRI data preprocessed with fMRIPrep”. In: *Nature protocols* vol. 15, no. 7, pp. 2186–2202.
- Gerstner, W. et al. (2014). *Neuronal Dynamics: From Single Neurons to Networks and Models of Cognition*. Cambridge University Press.
- Halverson, J., Maiti, A., and Stoner, K. (2021). “Neural networks and quantum field theory”. In: *Machine Learning: Science and Technology* vol. 2, no. 3, p. 035002.
- Halverson, James, Maiti, Anindita, and Stoner, Keegan (2020). *Neural Networks and Quantum Field Theory*. arXiv: [2008.08601 \[cs.LG\]](https://arxiv.org/abs/2008.08601).
- (Mar. 2021). “Neural Networks and Quantum Field Theory”. In: *Machine Learning: Science and Technology*.
- Hameroff, S. and Penrose, R. (1996). “Orchestrated reduction of quantum coherence in brain microtubules: A model for consciousness”. In: *Mathematics and computers in simulation* vol. 40, no. 3-4, pp. 453–480.
- Hebb, Donald O (1949). “The first stage of perception: growth of the assembly”. In: *The Organization of Behavior* vol. 4, pp. 60–78.
- Jedlicka, P. (2005). “Neuroethics, reductionism and dualism”. In: *Trends in Cognitive Sciences* vol. 9, no. 4, p. 172.
- (2009). “Quantum stochasticity and neuronal computations”. In: *Nature Precedings*, pp. 1–1.
- (2017). “Revisiting the quantum brain hypothesis: toward quantum (neuro) biology?” In: *Frontiers in molecular neuroscience* vol. 10, p. 366.
- Al-Khalili, J. and McFadden, J. (2014). “Life on the Edge: The Coming of Age of Quantum Biology”. In.

- Koch, C. and Hepp, K. (2006). “Quantum mechanics in the brain”. In: *Nature* vol. 440, no. 7084, pp. 611–611.
- Layer, M. et al. (2022). “NNMT: Mean-Field Based Analysis Tools for Neuronal Network Models”. In: *Frontiers in neuroinformatics* vol. 16.
- London, M., Hausser, M., et al. (2005). “Dendritic computation”. In: *Annual review of neuroscience* vol. 28, no. 1, pp. 503–532.
- Mező, István and Keady, Grant (2016). “Some physical applications of generalized Lambert functions”. In: *European Journal of Physics* vol. 37, no. 6, p. 065802.
- Miranker, W. L. (2006). “A neural network wave formalism”. In: *Advances in Applied Mathematics* vol. 37, no. 1, pp. 19–30.
- Mogiliansky, A. L., Zamir, S., and Zwirn, H. (2009). “Type indeterminacy: A model of the KT (Kahneman–Tversky)-man”. In: *Journal of Mathematical Psychology* vol. 53, no. 5, pp. 349–361.
- Nanopoulos, D. (1995). “Theory of brain function, quantum mechanics and superstrings”. In: *arXiv preprint hep-ph/9505374*.
- Nishiyama, A. and Tuszynski, J. A. (2019). “Non-Equilibrium ϕ^4 theory for networks: towards memory formations with quantum brain dynamics”. In: *Journal of Physics Communications* vol. 3, no. 5, p. 055020.
- Owen, L. L.W. et al. (2020). “A Gaussian process model of human electrocorticographic data”. In: *Cerebral Cortex* vol. 30, no. 10, pp. 5333–5345.
- Pothos, E. M. and Busemeyer, J. R. (2009). “A quantum probability explanation for violations of ‘rational’ decision theory”. In: *Proceedings of the Royal Society B: Biological Sciences* vol. 276, no. 1665, pp. 2171–2178.
- Potjans, T. C. and Diesmann, M. (2014). “The cell-type specific cortical microcircuit: relating structure and activity in a full-scale spiking network model”. In: *Cerebral cortex* vol. 24, no. 3, pp. 785–806.
- Rolls, E. T. and Deco, G. (2010). *The noisy brain: stochastic dynamics as a principle of brain function*. Vol. 34. Oxford university press Oxford.
- Swan, M., Santos, R. P. dos, and Witte, F. (2022). “Quantum Neurobiology”. In: *Quantum Reports* vol. 4, no. 1, pp. 107–126.

- Tegmark, M. (2000). “Importance of quantum decoherence in brain processes”.
In: *Physical review E* vol. 61, no. 4, p. 4194.
- Wang, Z. et al. (2014). “Context effects produced by question orders reveal quantum nature of human judgments”. In: *Proceedings of the National Academy of Sciences* vol. 111, no. 26, pp. 9431–9436.
- Williams, C. (1996). “Computing with infinite networks”. In: *Advances in neural information processing systems* vol. 9.
- Yaida, S. (2020). “Non-Gaussian processes and neural networks at finite widths”.
In: *Mathematical and Scientific Machine Learning*. PMLR, pp. 165–192.
- Yukalov, V. I. and Sornette, D. (2011). “Decision theory with prospect interference and entanglement”. In: *Theory and Decision* vol. 70, no. 3, pp. 283–328.

Conclusion

This thesis deals with the necessity to support the clinical decision making process providing mathematical, statistical and computational tools to describe, understand and predict disease patterns and its time evolution, with special focus on neurology and neuroradiology fields. The thesis is divided into three parts.

Part1 is related to the development of a Radiomic workflow combined with ML algorithms that allows the prediction of neuromuscular biomarkers, Fat Fraction and water T2, from MRI images in order to quantify muscle fat replacement and muscle inflammation, respectively. These parameters are able to foster the quantitative detection of anatomical changes of muscles that characterize neuromuscular diseases, with special focus on FSHD. The main contribution of these studies is that the developed workflow relies on conventional MRI sequences, such as gradient-echo, spin-echo and STIR imaging, most likely available in the greatest part of neuromuscular centers, thus it constitutes a non-invasive tool to monitor even the fine change in neuromuscular disorders and to evaluate longitudinal progression over time. Besides, in dealing with the time-consuming segmentation problem, we provided an automated tool based on convolutional neural networks that classifies the MRI images in input as thigh or calf and then it also returns the associated muscle-wise segmentation maps as output.

Part 2 is about the description of a kinetic model for tumor growth by means of classical tools of statistical mechanics for many-agent systems also taking into account the effects of clinical uncertainties related to patient variability in

tumor progression.

From a theoretical point of view the main contribution of this work is the introduction of a statistical approach based on kinetic theory to describe the growth of tumor cells in terms of the evolution of distribution function whose temporal variation is related to elementary transitions occurring at the cellular level and incorporating environmental cues and random fluctuations. The large time behavior of the system is obtained as a solution of the associated Fokker-Planck equation and it depends on the nature of microscopic transitions. The action of therapeutic protocols is modeled as feedback control at the microscopic level with the aim to steer the volume of the tumors toward a smaller target volume. The implementation of suitable control selective strategies results in modifying the nature of the emerging distribution of tumor sizes. From a computational point of view, the main contribution is the introduction of suitable numerical methods, based on stochastic Galerkin formulation of the derived kinetic equations, to deal with uncertainties. We also showed how the control protocols are capable of dampening the variability of the tumor dynamics due to the presence of uncertainties.

Part 3 refers to a still-on going project that attempts to describe a brain portion through a quantum field theory and, due to the connection between quantum field theory and neural network highlighted in Halverson, Maiti, and Stoner [2021](#), to simulate its behavior through the implementation of a neural network. To this end, we construct a suitable activation function mimicking the biological neuron model response function. From a theoretical point of view, the main contribution is the creation of a quantum field theory framework for a brain portion description that may eventually pave the way for future study on quantum effects in the brain. From a computational point of view, the main contribution is the identification of a fully-connected neural network with an *ad-hoc* defined activation function and inputs to simulate a brain portion. We come out with the conclusion that, under the considered conditions, the brain portion activity can be expressed up to $O(6)$, *i.e.*, up to six fields interaction, as

a Gaussian Process. The defined framework is still valid in the case of a resulting Non-Gaussian Process but further studies are necessary. An additional planned work is the extension of this model in more dimensions, *e.g.*, a 3D space, by considering not just real scalar bosons but complex scalar bosons or even some analogue of the particles with spin. Besides, provided the data availability such as EEG or fMRI data, another future work is to train the introduced network to reproduce neural data of a certain brain portion. A further future perspective is to simulate different brain portions and to connect them with a connectivity map determined by correlation matrix, as usual in connectomics, in order to reproduce the full-brain activity.